Topographic couplings and waves in planetary cores

Rémy Monville

▶ **To cite this version:**

Rémy Monville. Topographic couplings and waves in planetary cores. Sciences of the Universe [physics]. Université Grenoble Alpes [2020-..], 2024. English. NNT : 2024GRALU017 . tel-04661653

HAL Id: tel-04661653

https://theses.hal.science/tel-04661653v1

Submitted on 25 Jul 2024

HAL is a multi-disciplinary open access archive for the deposit and dissemination of scientific research documents, whether they are published or not. The documents may come from teaching and research institutions in France or abroad, or from public or private research centers.

L'archive ouverte pluridisciplinaire **HAL**, est destinée au dépôt et à la diffusion de documents scientifiques de niveau recherche, publiés ou non, émanant des établissements d'enseignement et de recherche français ou étrangers, des laboratoires publics ou privés.

THÈSE

Pour obtenir le grade de

DOCTEUR DE L'UNIVERSITÉ GRENOBLE ALPES

École doctorale : STEP - Sciences de la Terre de l'Environnement et des Planètes
Spécialité : Sciences de la Terre et de l'Environnement
Unité de recherche : Institut des Sciences de la Terre

Couplages et ondes topographiques dans les noyaux planétaires

Topographic couplings and waves in planetary cores

Présentée par :

Rémy MONVILLE

Direction de thèse :

David CEBRON CHARGE DE RECHERCHE, Université Grenoble Alpes	Directeur de thèse
Dominique JAULT DIRECTEUR DE RECHERCHE, Université Grenoble Alpes	Co-directeur de thèse

Rapporteurs :

Véronique DEHANT
FULL PROFESSOR, Observatoire Royal de Belgique
Gael CHOBLET
DIRECTEUR DE RECHERCHE, CNRS délégation Bretagne et Pays de la Loire

Thèse soutenue publiquement le **22 avril 2024**, devant le jury composé de :

Julien AUBERT, DIRECTEUR DE RECHERCHE, CNRS délégation Paris Centre	Président
David CEBRON, CHARGE DE RECHERCHE HDR, CNRS délégation Alpes	Directeur de thèse
Dominique JAULT, DIRECTEUR DE RECHERCHE, CNRS délégation Alpes	Co-directeur de thèse
Véronique DEHANT, FULL PROFESSOR, Observatoire Royal de Belgique	Rapporteure
Gael CHOBLET, DIRECTEUR DE RECHERCHE, CNRS délégation Bretagne et Pays de la Loire	Rapporteur
Christophe BRUN, MAITRE DE CONFERENCES HDR, Université Grenoble Alpes	Examinateur
Daphné LEMASQUERIER, ASSISTANT PROFESSOR, University of St Andrews	Examinatrice

Résumé

En complément des observations magnétiques, la dynamique des noyaux liquides des planètes peut être explorée en mesurant leur rotation. Par exemple, à certaines échelles de temps, le couplage entre le noyau liquide et le manteau terrestre peut être estimé par ces mesures. La dissipation d'énergie associée aux nutations est contrainte par les mesures de rotation de la Terre, tandis que le couple sur l'axe de rotation est fourni par la mesure de la durée du jour. Dans les deux cas, les données ne concordent pas bien avec nos modèles actuels de couplages noyau-manteau. Pour interpréter ces observations, ce travail vise à développer un nouveau modèle de couplage fluide-solide.

Bien que les couplages mécaniques entre les domaines fluides et solides aient été largement étudiés, leurs estimations restent difficiles pour les couches fluides planétaires de grande épaisseur en présence d'effets topographiques, magnétiques, de rotation, et de stratification en densité. Les résultats des études sur l'atmosphère et l'océan ne sont en effet pas directement transposables aux couches épaisses telles que les océans de subsurface des lunes glacées ou les noyaux liquides des planètes. En considérant une couche fluide en rotation et stratifiée, nous avons développé un modèle local semi-analytique pour étudier le couplage en pression provenant de la topographie de petite échelle et le couplage électromagnétique.

Notre approche permet de lever plusieurs limites des modèles précédents de couplage. Elle permet d'obtenir les différentes contraintes exercées par le fluide sur une paroi en trois dimensions et conductrice (par exemple, le manteau inférieur). Ce modèle permet d'explorer une large gamme de paramètres et de conditions aux limites pour des topographies arbitraires. Nous prenons également en compte les effets de courbure planétaire en considérant une approximation de "plan-β" non traditionnelle adaptée aux couches fluides de grande épaisseur. En menant une étude détaillée du mécanisme de traînée d'onde, nous montrons que les ondes de Rossby, absentes des modèles asymptotiques récents, peuvent modifier significativement la contrainte sur le solide. Un tel effet n'existe d'ailleurs que pour des topographies moins spécifiques qu'étudiées auparavant.

Notre méthode prend en compte la variation spatiale de l'inclinaison et de la norme du champ magnétique et du vecteur rotation. Après intégration sur l'interface noyau-manteau, cela permet d'estimer plus précisément le couple topographique. Par conséquent, nous délimitons mieux l'espace de paramètres (hauteur de la topographie, intensité du champ magnétique, stratification) permettant de rendre compte des observations. Notre méthode fournit un cadre unique pour étudier à la fois les problèmes de la dissipation de la nutation annuelle ainsi que pour la variation de longueur du jour.

Abstract

One way to probe the dynamics of planetary liquid cores is by measuring planetary rotation. For instance, the coupling between the liquid core and the Earth's mantle is constrained by measurements of the Earth's rotation. Energy dissipation related to nutations is constrained by measurements of the tilting of Earth's rotation axis, whereas time series of the axial torque can be derived from length of day observations. In both cases, the data do not agree well with our current models of core-mantle boundary couplings. To better interpret these observations, this work aims to develop a new coupling model.

While mechanical couplings between fluid and solid domains have been widely studied, their estimation remains challenging for deep planetary fluid layers in the presence of topography, rotation, magnetic field, and density stratification. Results from atmospheric or oceanic sciences are unsuitable for thick layers, such as subsurface oceans of icy moons or liquid cores of planets. We consider a rotating and stratified fluid layer. We have developed a semi-analytical local box model to investigate small-scale topographic fluid-solid coupling due to pressure or magnetic stresses.

Our code unlocks several limitations of previous planetary coupling studies. By considering three-dimensional bumps, it provides the various fluid stresses on an electrically conducting solid (such as the Earth's mantle lowermost layer). We explore a wide range of parameters and boundary conditions for arbitrary topography shapes and account for planetary curvature effects by considering a "non-traditional β-plane" approximation suited for deep fluid layers. Carrying out a detailed study of the wave drag mechanism, we show that the Rossby waves, which are absent from recent asymptotic models, can significantly modify the boundary stress. We also show that the results are different if we consider three-dimensional topographies instead of ridges.

More precise geophysical applications are also provided by taking into account spatial variations of the magnetic field and rotation vector in both directions and magnitude. This provides the global torque after integration on the core-mantle interface. Therefore, we better circumscribe the parameter space (topography height, magnetic field intensity, stratification) that enables reproducing the observations. Our method provides a unique framework to investigate the dissipation of the Earth's nutations and the variations of the length of the day.

Remerciement

Arrivant à l'aboutissement de ma thèse, j'aimerais remercier toutes les personnes qui ont été présentes pendant ces trois années et qui ont permis que celle-ci se déroule dans les meilleures conditions.

Je voudrais tout d'abord remercier mes directeurs, David et Dominique, pour m'avoir encadré pendant ce travail. Je vous remercie pour votre grande implication, pour toutes les connaissances que vous m'avez apportées, mais aussi pour votre confiance qui m'a permis de mener à bien cette thèse. Je garderai un très bon souvenir de ces années à travailler avec vous.

Je remercie chaleureusement les membres de mon jury : Julien Aubert, Christophe Brun, Gaël Choblet, Véronique Dehant et Daphné Lemasquerier. Merci d'avoir accepté ce rôle et pour vos retours précieux. Je voudrais également exprimer ma gratitude à Bruno Voisin et Séverine Rosat, qui ont accepté de faire partie de mon comité de thèse et de m'avoir suivi tout au long de ce travail.

Je remercie aussi Jérôme Noir pour nos passionnantes discussions sur la topographie, qui ont éveillé mon intérêt pour les expériences de laboratoire. Merci également à Thomas Frasson pour avoir pris le temps de réanalyser ses simulations et nous fournir un modèle de topographie.

Un grand merci ensuite à toute l'équipe Geodynamo, une équipe extrêmement soudée que je côtoie périodiquement depuis presque six ans et avec laquelle je garderai un lien particulier.

Merci beaucoup à tous les amis du laboratoire que j'ai côtoyés pendant ces trois ans : Quentin, Lisa, Laura, Nico, Hannah, Pauline, Val, Jérémie, Max... Pour les nombreuses pauses café, les sorties d'escalade, les conférences... Je n'aurais pourtant jamais cru écouter autant de sismologie !

Merci à ma famille pour leur soutien sans faille. Merci infiniment à tous mes colocataires : Lisa, Paul, Sarah, Amélie, Diego, Nico, Dodo, Erwan et Agathe, pour avoir partagé cette période à mes côtés.

Enfin, une pensée pour tout.e.s les ami.e.s, collègues, camarades, qui m'ont accompagné pendant cette thèse, mais aussi pendant cette quasi-décennie passée à Grenoble.

Contents

List of Figures and Tables

1 Introduction

Contents

1.1 Observational constraints on the core-mantle coupling

Why are we studying the Earth's core when it is out of reach, approximately 3000 km below our feet? The core is not as unrelated to us as you might think. The core is a 2200 km deep ocean of liquid iron, with a water-like kinematic viscosity, that has an influence at the surface of the Earth. The most measurable effect of the core is the large-scale magnetic field of the Earth, generated by turbulent motions within the conductive liquid core. This is the mechanism of the"geodynamo". The standard scenario is that the flow in the core is powered by thermo-solutal convection as a result of the cooling of the Earth and the crystallisation of the inner core (Roberts & King, 2013). This sustained magnetic field could have been crucial to the development of life on our planet by protecting the atmosphere from erosion (Lundin *et al.*, 2007; Gunell *et al.*, 2018). Throughout history, the magnetic field has been used for navigation, by humans (from the compass to modern GPS systems), but also by other forms of life such as birds, lobsters (Wiltschko & Wiltschko, 2005) or even bacteria (Rismani Yazdi *et al.*, 2018). Beyond the magnetic field, core dynamics also affect the rotation of the Earth. The Earth is subjected to many external gravitational forces, mainly from the luni-solar system, resulting in intricate motions. While celestial mechanics relates these forcings to the motion of a rigid body (of the same mass and inertia tensor as the Earth), calculating the response to these forcings for elastic and partially fluid bodies becomes challenging. Combining accurate measurements of Earth's rotation and dedicated models allows one to obtain precious information on the core-mantle coupling.

1.1.1 Probing the Earth's core dynamics from the surface

The Earth spins around an axis, orientated by its rotation vector $\mathbf{\Omega}_0$, completing its revolution in approximately 23h56, which is the sidereal period. This axis is tilted with respect to the ecliptic plane[1] at an angle of about 23°26', creating seasonal variations. The core-mantle boundary is not completely spherical, but rather a spheroid with a flattening of approximately 1/374 (Koot *et al.*, 2010). Due to this equatorial bulge and the tilt of the rotation axis, the Sun and Moon generate a torque on Earth. The angle relative to the ecliptic remains constant on average over time, but the axis of rotation describes a regular cone over a period of 26000 years. This phenomenon is called axial precession (blue in figure 1.1a). Small oscillations that deviate from this reference cone are called nutations (red in figure 1.1a). Nutations correspond by convention to motions with a period larger than 2 days. They can be divided between longitude nutations and obliquity nutations. The nutation with the largest amplitude is Bradley's nutation and has a period of 18.6 years[2]. Finally, the rotation rate of the Earth varies around its main axis (*i.e.* in magnitude), with variations of the order of milliseconds. This is called variation in the length of the day (LOD). All these motions can be measured with great precision using the very long baseline interferometry (VLBI) method (Thompson *et al.*, 2017). This consists of observation of very distant celestial bodies, such as quasars, with a network of telescopes. This allows one to reconstruct a very precise positioning of the Earth. The precision of the measurement of VLBI is on the order of tens of μas (that is, approximately 1 mm at the Earth's surface) and approximately 10 μs (Bizouard *et al.*, 2019; Liu *et al.*, 2020). As said before, the nutation and precession motions are mainly driven by external forcings. We can calculate the forces applied on Earth since we know the position of the celestial bodies (ephemerides). Theoretical response series can be calculated for a rigid Earth (Bretagnon *et al.*, 1997). However, the elasticity and existence of fluid layers significantly change the response of the Earth to external forcings. It is thought that LOD variations are primarily due to the motion of fluid layers (which can be tidally driven), which accelerate or decelerate the solid Earth, conserving angular momentum.

In addition to the well-known free normal (seismic) modes, the Earth also has free rotational modes. One of these modes is the Chandler wobble[3] with a period of $\approx$ 432 days in the terrestrial frame (An & Ding, 2022). The fluid outer core has a mode, called "free core nutation" (FCN), which is quasi-diurnal (with a frequency of 1.00232 cycles per day) in the terrestrial frame (Dehant & Mathews, 2015). The term "nutation" describes oscillations of the Earth's axis of rotation relative to an inertial frame. The FCN is associated with a diurnal wobble in the terrestrial frame. This mode is particularly of interest because it is excited by all quasi-diurnal forcings. In particular, it is close to the solar tide frequency of 1.00273 cycle per sidereal day (Buffett, 2010), generating a large amplitude motion in the core (see figure 1.2). There is also the inner core rotational free mode (FICN) and its associated wobble. However, even if this wobble is present in the nutation models,

[1] The plane containing the trajectory of the earth in orbit around the sun.

[2] As datasets do not last long enough, most studies have been carried out on annual (in celestial frame) nutation.

[3] The term wobble describes "any periodic or quasiperiodic motion of the Earth instantaneous rotation axis with respect to the figure of the Earth" (Dehant & Mathews, 2015).

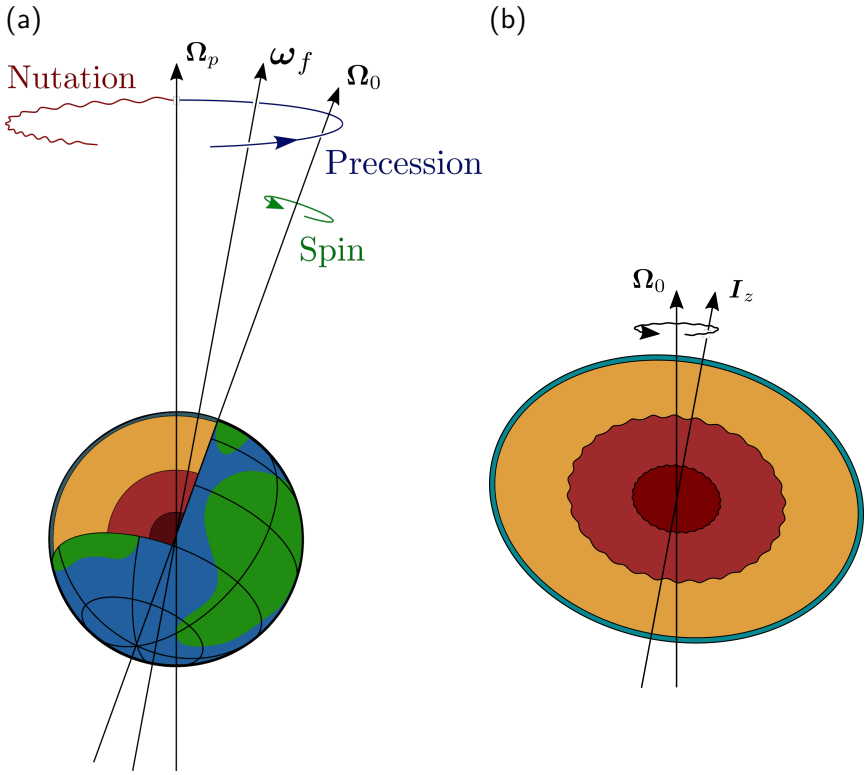

Figure 1.1: Sketch of Earth rotation mechanisms. **(a)** Sketch of the main motions of Earth. $\boldsymbol{\Omega}_p$ is the precession axis vector, $\boldsymbol{\Omega}_0$ is the mantle rotation vector that defines the geographical position of the north and south poles. $\boldsymbol{\omega}_f$ is the rotation axis of the fluid. **(b)** Sketch of the (exaggerated) interior geometry of the Earth. $\boldsymbol{I}_z$ is the main inertia axis (not necessarily aligned with $\boldsymbol{\Omega}_0$).

it has not yet been observed in the rotation measurements (Rosat *et al.*, 2017). In this work, we will perform our calculations in the reference frame rotating at $\boldsymbol{\Omega}_0$, which is not aligned with the main inertial axis $\boldsymbol{I}_z$ (see figure 1.1b).

$\boldsymbol{\omega}$ is an arbitrary fluid vector $\boldsymbol{\Omega}$ when seen in a frame rotating at $\boldsymbol{\Omega}_0$ and is related to $\boldsymbol{\Omega}$ by (Noir & Cébron, 2013)

$$\omega_x = \Omega_x \cos(\Omega_0 t) + \Omega_y \sin(\Omega_0 t), \tag{1.1a}$$

$$\omega_y = -\Omega_x \sin(\Omega_0 t) + \Omega_y \cos(\Omega_0 t), \tag{1.1b}$$

$$\omega_z = \Omega_z - \Omega_0, \tag{1.1c}$$

When the fluid rotation vector $\boldsymbol{\Omega}$ is steady in the frame of precession rotating at $\boldsymbol{\Omega}_p$ (such as when only precession forcing is present). Then, all coefficients $\Omega_{x,y,z}$ are constant, and the motion is then diurnal in the mantle frame. For nutation motions, the coefficients $\Omega_{x,y,z}$ are time-dependent. However, for periods in the inertial frame much longer than the day, these coefficients can be approximated as constant (in the mantle frame). This is referred to as quasi-diurnal forcing, as opposed to precession, which is exactly diurnal. The time variations of Ω_z correspond to the variation of the LOD.

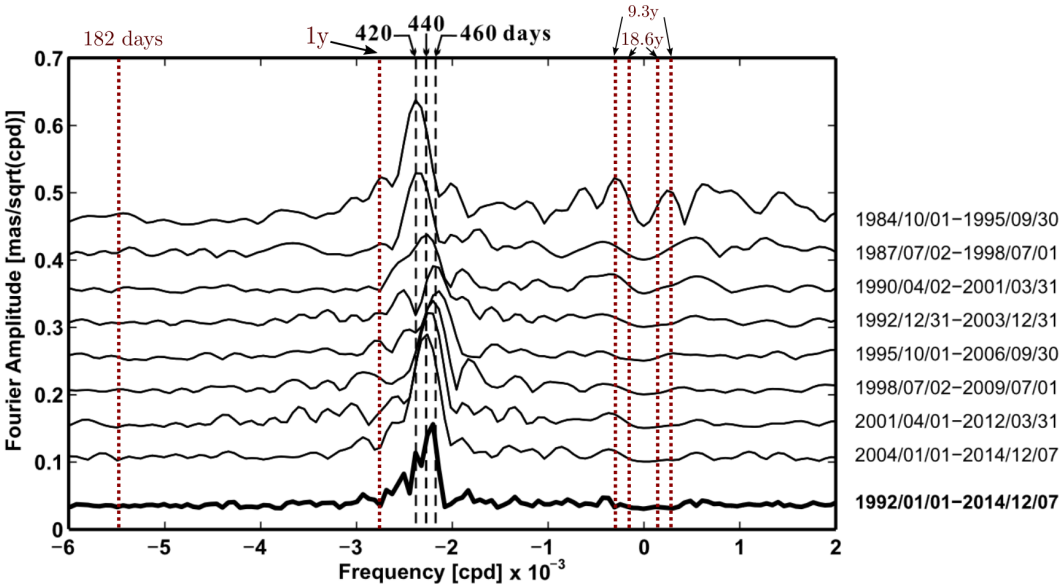

Figure 1.2: Fourier amplitude spectrum of the VLBI FCN complex series for 11-year segment datasets each advanced by 2.8 yr with 75% overlap consecutively (the respective timespan given on the right). The bottom thick curve is that for the 23-year full dataset. The periods are indicated on the top axis. The dotted red lines are the periods of the main external nutations forcings (Mathews *et al.*, 2002). Figure (without red lines) from Chao & Hsieh (2015).

In addition to rotation, the magnetic field measured at the surface of the Earth provides information on the core dynamics. Early measurements were made mainly using ground stations scattered around the globe. Recent advances in satellite measurement (*e.g.* the Swarm mission of the European Space Agency Friis-Christensen *et al.*, 2008) have led to considerable improvements in the temporal and spatial resolution of field measurements. One can reconstruct the magnetic field from the surface to the CMB by making assumptions about the mantle conductivity. This problem was first addressed with an insulating mantle using potential field theory (*e.g.* Whaler & Gubbins, 1981). However, the mantle is expected to not be fully insulating and acts then as a filter for the most rapid variations of the magnetic field in the core (Jault, 2015). Once we have a magnetic field model at the CMB, we can use inverse models to propose admissible core flows (Gillet *et al.*, 2015).

These velocity models at the surface of the core can be used to estimate the exchange of angular momentum between the core and the mantle using different methods. Knowing the angular momentum variation of each layer and assuming that the Earth is a closed system that conserves its angular momentum, allows us to reconstruct the motion of the mantle. In particular, knowing the velocity variation of the fluid at each point allows one to calculate its angular momentum variation. To use this method for the outer core, it is necessary to use models that reconstruct the flow in the interior. This method has been used for LOD calculations by Pais & Jault (2008) or Gillet *et al.* (2022) from the inversion of core flows at the CMB using magnetic field measurements. The angular momentum is then calculated by extending the surface flows with invariance along the rotation axis. This angular momentum L is written (assuming uniform density) as a function of only two

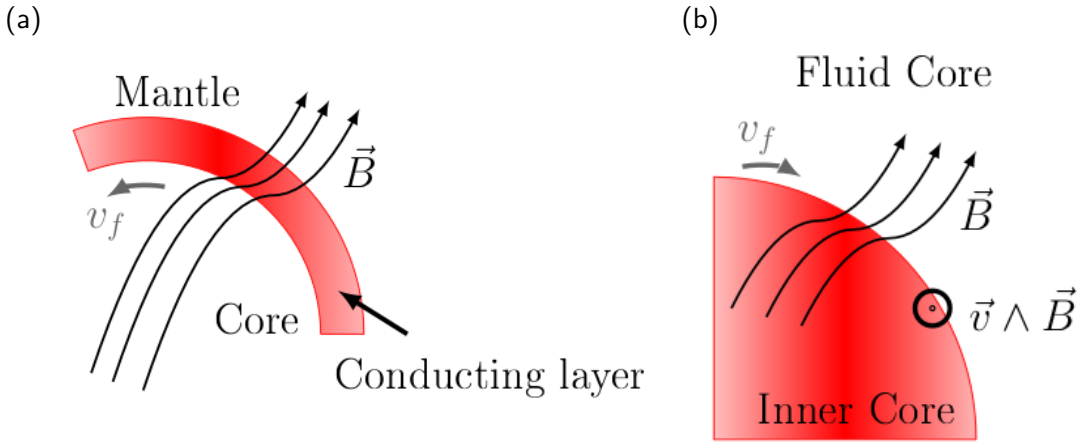

Figure 1.3: Schematic of electromagnetic coupling in the core. **(a)** Between the outer core and the mantle. **(b)** Between the inner core and the outer core. The differential rotation of the two layers bends the magnetic field lines and generates a force. Figure from Rosat (2016).

toroidal components of the surface flow as

$$L = \beta_l (t_1^0 + 12/7 t_3^0), \tag{1.2}$$

with t_n^0 the zonal toroidal component of the flow of spherical harmonic degree n, β_l is a constant (Jault *et al.*, 1988). The expression of the core angular momentum considering an adiabatic profile of density (Jault & Finlay, 2015) shows an infinite number of terms but stays dominated by the components of equation 1.2. Finally, Schwaiger *et al.* (2024) shows that the time-dependent part of 1.2 accounts very well for the core angular momentum changes in dynamo simulations.

1.1.2 Coupling mechanisms between planetary layers

The transfer of angular momentum between the different layers of the Earth involves coupling mechanisms. One can distinguish 4 types of coupling mechanisms (Roberts & Aurnou, 2012).

- **Gravitational**: These effects consist of a non-local force between anomalies of mass in the inner core and the mantle. It has been proposed to explain the variations in the length of day (Buffett, 1996; Davies *et al.*, 2014). This theory is supported by the seismological inference of large-scale deep regions at the bottom of the mantle. Tidal tomography indicates that these regions are dense (Lau *et al.*, 2017).

- **Viscous**: This is the force generated by a viscous flow on a solid as a result of shear in the boundary layer. The outer core kinematic viscosity is estimated to be in the range of $3 \times 10^{-7} - 5 \times 10^{-6}$ m s^{-2} (Mineev & Funtikov, 2004). The laminar viscous torque does not therefore seem to be able to explain the variations observed in Earth's rotation. This coupling can become non-negligible in the case of a turbulent flow permeated by a magnetic field, but

remain lower than the required torque (Deleplace & Cardin, 2006; Buffett & Christensen, 2007).

- **Electromagnetic**: This coupling appears if the solid (inner core or mantle) is electrically conducting. The flow inside the outer core bends the magnetic field lines that cross the boundary, generating a restoring force (see figure 1.3). This force is often considered to explain some of the variations in LOD (Holme, 1998). Although the torque amplitudes may be of the right order of magnitude, problems arise when looking at the time series of the LOD. Electromagnetic coupling has also been proposed to play a role in the dissipative part of annual nutation (Buffett, 1992; Deleplace & Cardin, 2006; Buffett, 2010).

- **Pressure**: This coupling is caused by a flow that encounters a surface that deflects it (ocean floor, mountains, etc.). In the core, it appears because of the deviations of the CMB from the sphericity. This concerns not only the ellipsoidal shape of the CMB but also medium- and short-wavelength bumps. This has been proposed as a mechanism by numerous studies (*e.g.* Hide, 1969; Moffatt, 1977; Braginsky, 1998; Acheson, 1975; Jault & Mouël, 1989; Kuang & Chao, 2001; Buffett, 2010; Glane & Buffett, 2018; Jault, 2020). The strength of this coupling is strongly related to the stratification, the intensity of the magnetic field, and its orientation.

All these couplings are based on more or less uncertain parameters. We provide a brief review of parameters that will be of interest in this work.

It has long been proposed that the upper part of the core has a stratified layer, but its thickness and the strength of this stratification are debated. The most common explanation is the accumulation of light elements at the CMB. Alternatively, Landeau *et al.* (2016) found that a thick stratified layer at the top of the core may result from merging between the proto-Earth and projectile cores following a giant impact, such as the moon forming event. Bouffard *et al.* (2020) concluded that such a primordial layer would survive convective erosion. The thickness of this layer is estimated to be 10 to 400 km. Insights on this subject are coming for seismic data (Helffrich & Kaneshima, 2010; Irving *et al.*, 2018; Kaneshima, 2018), mineral physics, thermal evolution model, but also magnetic field observations and dynamo simulations (Gastine *et al.*, 2020). Buffett (2014) and Buffett *et al.* (2016) predict a layer of 140 km thick with a buoyancy frequency close to the rotation frequency from the fluctuation of the dipolar part of the magnetic field. Olson *et al.* (2018) predict a thicker 400 km layer by comparing dynamo simulations and observed magnetic field structures. For a review that covers these different aspects, see Hirose *et al.* (2013); Hardy & Wong (2019).

The magnetic field at the CMB can be obtained by extrapolating the magnetic field measured at the surface and making assumptions about the mantle conductivity. The field measured as the surface is more dipolar than the one at the CMB since the small scales decay geometrically far from the sources, faster than the large scales (Lowes, 1974). The conductivity of the lower mantle is estimated mostly from indirect sources. Some estimates are obtained by calculating the torque necessary to explain the length of the day (Holme, 1998) or the nutation measurements (Buffett, 1992, 2010). The mantle is also not completely insulating and acts as a filter for short periods and long spatial wavelengths (Mandea *et al.*, 1999; Jault, 2015). This makes it difficult to reconstruct

the magnetic field at the CMB. The conductivity of the lower mantle is estimated mostly from indirect sources. Some estimates are obtained by calculating the torque necessary to explain the length of the day (Holme, 1998) or the nutation measurements (Buffett, 1992, 2010). As the conducting mantle acts as a low-pass filter for the magnetic field, Jault (2015) studies the filtering of the different magnetic field frequencies to give an estimate of the conductance. Schaeffer & Jault (2016) also proposed that the observed absorption of torsional waves at the equator by a conducting lowermost mantle yields an estimate of the conductance next to the equator of the core. Conductivity values are also obtained from mineralogy studies (*e.g.* Yoshino, 2010). Combining all of these results yields a very wide range of possible conductivity ($2 - 10^4$ S m^{-1}).

This research work focuses primarily on topographic coupling, raising an important initial question: does the CMB display irregularities? The conclusions drawn by the seismologists indicate that this is indeed very likely. Even if it remains largely unknown, the CMB topography is expected to have an amplitude quite similar to that of the Earth's surface, with a broad wavelength spectrum. Therefore, we can expect significant effects from this. Figure 1.4 presents a review of the expected typical topography. It includes a seismological calculation (for a detailed review on this topic see Koelemeijer, 2021). Some insights are also provided by numerical simulation of mantle convection (Coltice *et al.*, 2019) or by crystallisation / dissolution models (Narteau *et al.*, 2001), which give some insight into the small wavelength (< 100 km) undetectable by seismology.

1.1.3 Models of the Earth's rotational response

The Earth can be seen as a (nearly) spherical spinning top[4] subject to external forces with several layers that exchange moments by different coupling mechanisms. These complex mechanics can be modelled using various methods to reproduce the behaviour of the Earth. Models of Earth's rotation often exploit the Earth's axisymmetry (for the mass distribution) to separate the effects of angular velocity variations on the axis of rotation (LOD) from the one on the equatorial axes (precession, nutations). In fact, the fluid response of the core to these forcings is different for each case. For nutation and precession forcings, the main response is a uniform vorticity flow, which is close to a solid body rotation around an equatorial axis. For variation on the rotation axis, motions on a period longer than one day[5] are mainly constrained by the Taylor-Proudman theorem and take the form of geostrophic columns.

[4]With fluid layers and deformable solid layers.

[5]For rapid motions on a time scale much shorter than one rotation period, rotation effects become weak.

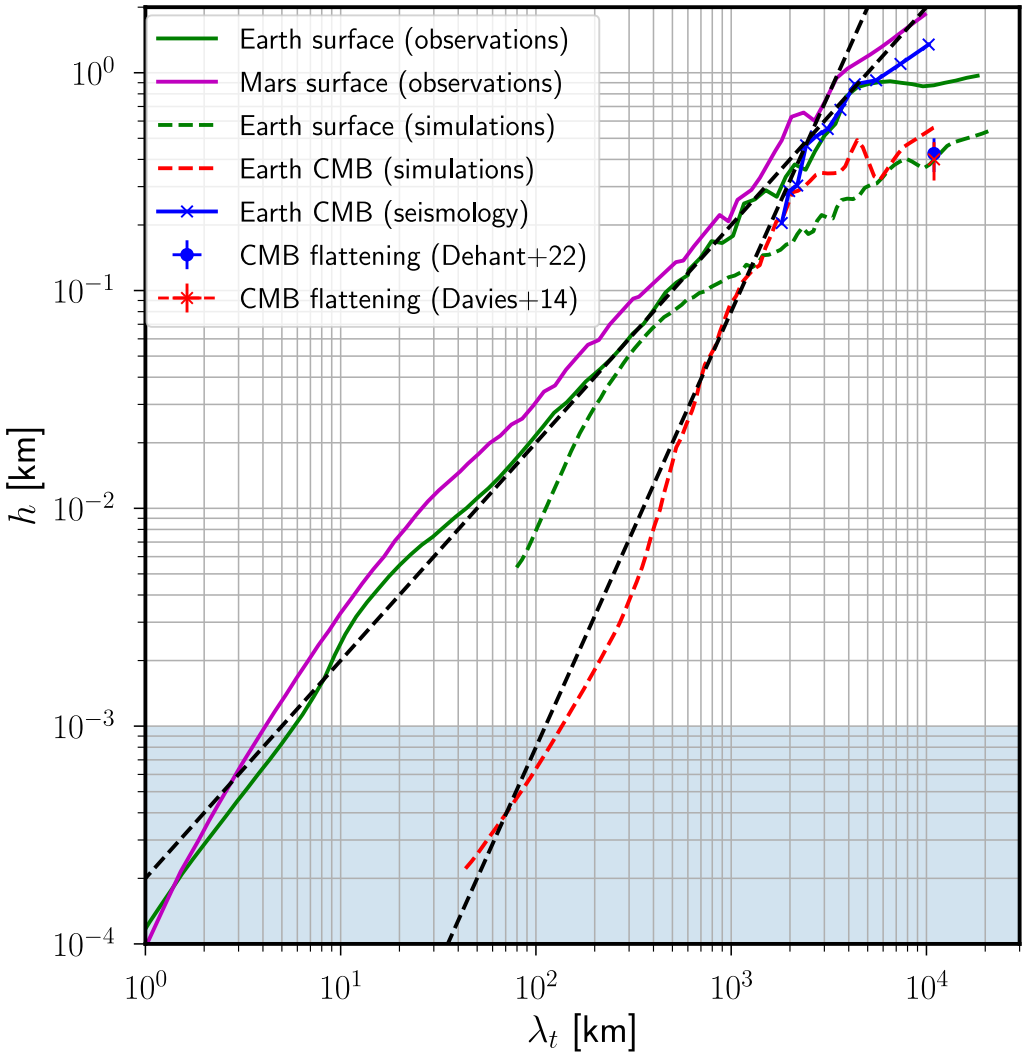

Figure 1.4: Typical topography height h vs. wavelength λ_t, from the RMS of the observed power spectrum at the Earth and Mars' surface (solid green and purple, Rexer & Hirt, 2015), or from a simulation (dashed green and red Coltice *et al.*, 2019) of the Earth's mantle convection with plate tectonics (model 5 in Arnould *et al.*, 2020, averaged on 300 – 450 Myr, courtesy of T. Frasson & N. Coltice), where the vertical stress provides h (equilibrium with gravity). The SBF2012-T model for Earth's CMB (Koelemeijer, 2021), based on seismic body waves, is shown, as well as the CMB flattening departure (from the hydrostatic value) given by studies of Earth's nutations (Dehant *et al.*, 2022) or length of day (Davies *et al.*, 2014, based on the core-mantle gravitational coupling). For comparison, the viscous Ekman layer thickness is 10^{-4} – 10^{-3} km at the CMB and ICB (light blue zone). Black dashed lines: empirical laws $h \propto \lambda_t$ at the surface (Vening Meinesz rule for the RMS height, Ermakov *et al.*, 2018), and $h \propto \lambda_t^2$ proposed for the CMB (from the Kaula rule for gravity RMS spectrum, Puica *et al.*, 2023). This figure is consistent with figure 7 of Garcia & Souriau (2000), dividing their values by 5 (ratio between their figures 6a & 6b). From D. Cébron's HDR manuscript (submit.).

Core flow response to precession and nutations forcings

In a frame rotating at a time-dependent rotation vector, the fluid experiences a volume force, which is the Poincaré force $(\mathrm{d}_t \boldsymbol{\Omega}) \times \boldsymbol{r}$, with $\boldsymbol{r}$ the position. This forcing has the same spatial dependence as the free spin-over mode, which will resonate in the presence of this excitation. This mode is a solution of the inertial modes equation and takes the form

$$\boldsymbol{u} = \boldsymbol{\Omega} \times \boldsymbol{r} + \nabla \psi \tag{1.3}$$

with ψ a potential ensuring the non-penetration condition at the boundary (associated with a flow linear in Cartesian coordinates). In our case, where the CMB is close to a sphere, $\nabla\psi$ is small. Nutation forcing forces the equatorial component of this uniform vorticity flow.

The earliest models of nutation use Euler's equation on a rigid Earth to provide the response to external forcings (Woolard, 1953). These models are then followed by the introduction of the elasticity of the Earth, firstly with the models of Jeffreys & Vicente (1957) and Molodensky (1961). These models split the equations between a static rheology equation and the well-known Liouville equations (Liouville, 1858), which is the conservation of the angular momentum (*i.e.* Euler's equation) for non-rigid bodies. These equations are given for each layer by

$$\mathrm{d}_t \boldsymbol{H} + \boldsymbol{\Omega} \times \boldsymbol{H} = \boldsymbol{\Gamma} \tag{1.4}$$

with $\boldsymbol{\Gamma}$ the torques applied to the body, where $\boldsymbol{H} = [\boldsymbol{C}] \cdot \boldsymbol{\Omega}$ is the angular momentum $[\boldsymbol{C}]$ is the (possibly time-dependent) inertia tensor which includes the effects of elasticity, and $\boldsymbol{\Omega}$ is the rotation vector of the frame in which we are standing. To model the Earth's response to nutation, two lines of research have been mainly followed.

First, an angular momentum description (AMD) can be used, integrating equation (1.4) for each layer of the Earth. It was pioneered by Molodensky (1961) and reformulated by Sasao *et al.* (1980), in the so-called SOS model. This approach allows semi-analytical expressions to be obtained with a few free parameters (ellipticity, compliances) constrained with data. The model was then improved, adding the dynamics of the inner core (Mathews *et al.*, 1991; Dehant *et al.*, 1993; Legros *et al.*, 1993). It was completed by the MHB2000 model (Mathews *et al.*, 2002; Buffett *et al.*, 2002), which has been the International Astronomical Union (IAU) reference model (Ferrándiz *et al.*, 2022) since 2000. The MHB model adds, in particular, the effect of the ocean, the atmosphere, and the electromagnetic coupling between the core and the mantle. Koot *et al.* (2008) later improves the inversion method of this model. More recent models also developed new features (not necessarily combined with the other effects included above), such as the elastic deformations associated with a tilted inner core (Dumberry, 2009), or the topographic coupling of a triaxial CMB (Guo & Shen, 2020). Despite all these improvements, the accuracy of the measurements motivates further discussions with the aim of improving the nutation models and defining a new reference model (Ferrándiz *et al.*, 2018, 2022).

The second approach is gravito-elastic models that rely on a linear momentum description (LMD), as reviewed in Rochester & Crossley (2009). By solving these equations numerically, we

can obtain displacements at any point on Earth. It is important to note that the AMD models can be considered as an integrated version, on each Earth's layer, of LMD the gravito-elastic ones. The LMD models are derived from the first studies of Smith (1977) and Wahr (1981). The model of Wahr (1981) was chosen in 1980 as the reference model of nutation (Seidelmann, 1982) by the IAU [6]. This model has been improved by adding mantle anelasticity (Dehant, 1987), atmosphere and ocean (Huang *et al.*, 2001), elastic deformation of the inner core (Rochester & Crossley, 2009) and magnetic field effects (Huang *et al.*, 2011).

These nutation models are important in the context of our study, since they provide estimates of the coupling at the CMB. The coupling between the layers is not explicitly modelled, but is introduced in a parameterised way. This parameterisation is introduced by a torque proportional to the differential rotation with a proportionality constant at the inner core boundary ($K_{\rm ICB}$) and the CMB ($K_{\rm CMB}$) written as (in the mantle frame)

$$\tilde{\Gamma}_{\rm ICB} = -\mathrm{i}\Omega_0^2 A_s K_{\rm ICB}(\tilde{m}_s - \tilde{m}_f). \tag{1.5a}$$

$$\tilde{\Gamma}_{\rm CMB} = -\mathrm{i}\Omega_0^2 A_f K_{\rm CMB}\tilde{m}_f. \tag{1.5b}$$

The notation $\tilde{}$ corresponds to a complex combination of the equatorial component of a vector (*e.g.* $\tilde{m} = m_1 + \mathrm{i}m_2$, Mathews *et al.*, 2002). The torque is noted $\tilde{\Gamma}$, A_f and A_s are the principal moments of inertia of the outer and inner core. $\tilde{m}_f$ is the differential rotation between the outer core and the mantle, where $(\tilde{m}_s - \tilde{m}_f)$ is the differential rotation between the inner and outer core. The $K_{\rm CMB}$ and $K_{\rm ICB}$ constants are complex, denoting an in-phase and out-of-phase response to external forcing. For the FCN, for instance, the ratio of the imaginary parts of $K_{\rm ICB}$ over $K_{\rm CMB}$ is typically found to be 60, which is of the order of $A_f/A_s \approx 155$, while $\tilde{m}_s - \tilde{m}_f \approx 0.4\tilde{m}_f$ (Koot, 2009), giving a ratio of 0.15 for the imaginary parts of $\tilde{\Gamma}_{\rm ICB}$ over $\tilde{\Gamma}_{\rm CMB}$, and thus a ratio of 0.06 between the associated dissipation. Therefore, the FCN damping is a priori dominated by the CMB coupling, but a large uncertainty remains on the value of $K_{\rm ICB}$. Note that this parameterisation of the coupling is modelled through a force on the boundary proportional to the velocity (equation 1.5). This is debatable since this scaling is known in fluid mechanics experiments to vary as a function of several parameters (*e.g.* the squared velocity for turbulent flows Shih *et al.*, 2023).

Some problems regarding the nutation seem to have been solved already. The in-phase (real part of the coupling constant) component of the annual nutation can be explained by an ellipticity higher by 5% (Gwinn *et al.*, 1986; Herring *et al.*, 1986), compared to the hydrostatic shape of the CMB. On the other hand, the dissipative part of the nutations remains difficult to explain. Precession coupling with the core, which is only briefly addressed in this manuscript, has been studied in the context of the Earth's secular spin evolution, showing an overall negligible influence (Correia, 2006). For a quantitative comparison, the Earth's precession drives a 2 mm/s flow at both its CMB and ICB[7] (Sikdar & Dumberry, 2023), while the (annual retrograde) nutation driven flows are roughly 20 times smaller at the CMB (Buffett, 2010), leading to a boundary layer Reynolds

[6] Upgrading the AMD model of Woolard (1953), IAU chose in 1979 the Molodensky (1961)'s AMD model as the reference, but, after an IUGG report, IAU finally retained in 1980 the Wahr (1981)'s LMD model (Seidelmann, 1982).

[7] leading to a boundary layer Reynolds number around 250 in both cases (Sikdar & Dumberry, 2023).

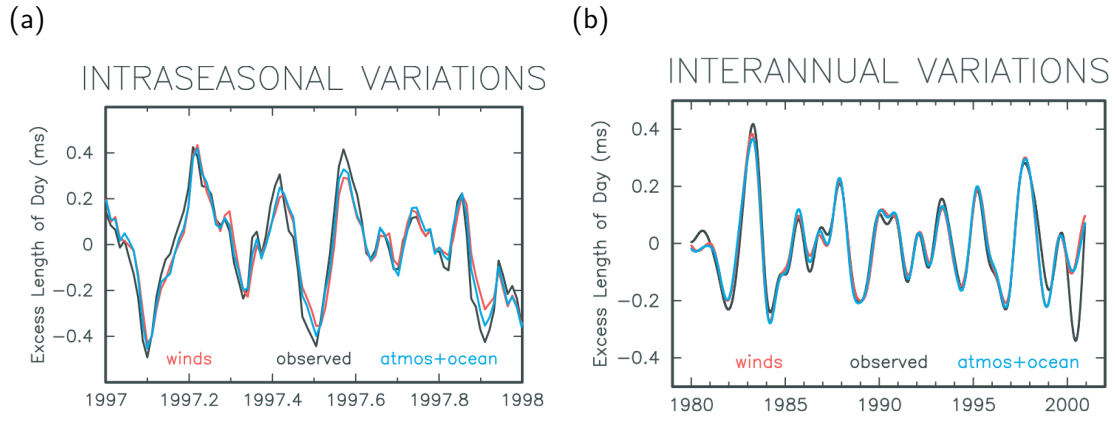

Figure 1.5: Observed length-of-day variations (black), variations caused by the modelled atmospheric winds (red) and variations caused by the sum of the modelled atmospheric winds, surface pressure, oceanic currents, and bottom pressure (blue). On seasonal **(a)** and **(b)** interannual timescale. On the seasonal time scale, the observed data are explained by the atmosphere and ocean at 92.2% in the period 1992 – 2000, and at 87.9% at the interannual time scale in the period 1980 – 2000 (Gross *et al.*, 2004). Figures from Gross *et al.* (2004).

number around 10. This corresponds to an associated nutation dissipation around 9 MW (Buffett, 2010), to be compared with the much larger precession-driven dissipation of 4.6 GW and 14.5 GW respectively expected at the CMB and ICB when considering the same coupling constants as for the annual retrograde nutation (Sikdar & Dumberry, 2023).

The variation in the length of the day is mainly due to the different exchanges of angular momentum between the solid Earth and the fluid layers. On short timescales (less than one year), variations of the LOD are mainly due to the coupling with the atmosphere (see figures 1.5 and 1.6a). The modelled contribution of the atmosphere separated the effects of the wind and pressure, with the addition of less significant ocean effects, providing a satisfactory explanation for the short periods. For longer periods, atmospheric or oceanic motions cannot fully explain the observations. Then a substantial part of the LOD variations is attributed to the core (Jault *et al.*, 1988; Holme & De Viron, 2013; Finlay *et al.*, 2023). To study the contribution of the core, the effects of the ocean and the atmosphere should be subtracted (Puica *et al.*, 2023; Rosat & Gillet, 2023). Figure 1.6, from Pfeffer *et al.* (2023) and Finlay *et al.* (2023), illustrates the core contribution to LOD data. Models of core-mantle coupling, which are required when modelling LOD variations, face three principal problems. First, when considering only one torque that acts to reduce the differential rotation between the core and the mantle (which is the case for the electromagnetic torque (Schwaiger *et al.*, 2024)), we expect that any initial differential rotation vanishes on a sufficiently long timescale. Therefore, a second torque is necessary to maintain a non-zero differential rotation (which allows LOD variations). A good candidate is a gravitational (coupling) torque between the mantle and the inner core Buffett (1996). The second problem is that the electromagnetic torque at the core-mantle boundary is expected to mainly arises from the axial rotation component of the

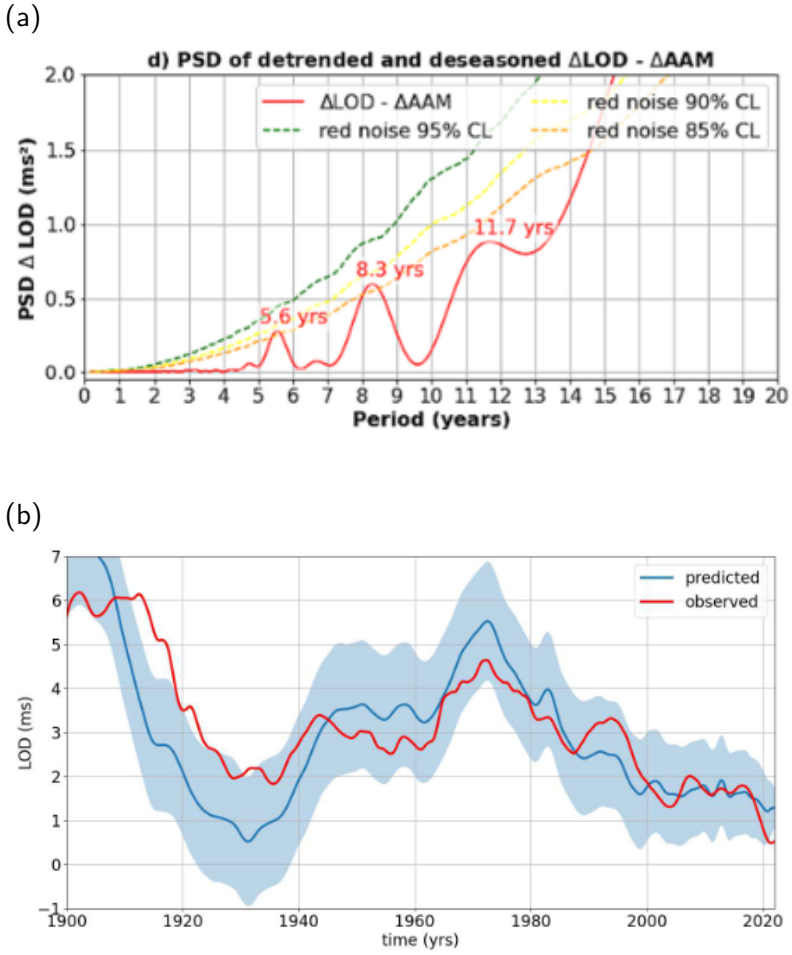

Figure 1.6: **(a)** Power spectrum density (PSD) of residual LOD variations corrected by the angular momentum of the atmosphere (AAM). Confidence levels at 85, 90 and 95% are shown as orange, yellow, and green hatched lines. The residual value is higher for long periods with peaks at 5.6, 8.3, and 11.7 years. From Pfeffer *et al.* (2023). **(b)** Observed changes in LOD (red curve) and predicted LOD change from a core flow model. Observed LOD data are derived from VLBI data, from the C04 series, with estimated contributions from solid tides and atmospheric angular momentum removed. The blue envelope shows the spread in an ensemble of flow predictions. From Finlay *et al.* (2023)

core surface flow, as $\Gamma_{EM} = -\alpha_l t_1^0$ (as shown by Schwaiger *et al.*, 2024, with dynamo simulations), with α_l a constant that depends only on the conductance of the mantle. We can then model LOD series from the core flow and this expression of the coupling. However, these obtained LOD series do not correspond to the LOD measurements. Finally, the torque is supposed to be proportional to the time derivative of the angular momentum, whose calculation is given in the core by the equation 1.2. This would conflict with the expression of the electromagnetic torque, which does not contain any component in t_3^0 (as opposed to equation 1.2). As we do not know the flow dependence of other kinds of torque, such as topographic coupling, we can hope that their expressions differ from the one of the electromagnetic torque (possibly bringing solutions to these issues).

1.2 Topographic effects in geophysical flows

1.2.1 Pressure coupling, insights from ocean and atmosphere studies

The flow over topography is a historical issue in the atmospheric and ocean sciences (Scorer, 1949). In particular, waves that propagate downstream of a mountain range or a sea ridge are the subject of extensive literature (*e.g.* Smith, 1979, 1989; Wurtele *et al.*, 1996; Legg, 2021). These waves are observable in the atmosphere since they are indicated by specific wave cloud formations (*e.g.* see figure 1.7b). This is a major topic for which every good textbook dealing with the dynamics of the atmosphere and ocean has a section dedicated to (Gill, 1982; Cushman-Roisin & Beckers, 2011; Vallis, 2017). Baines (2022) even published a book dedicated to this topic.

These waves, called "lee" or "orographic" waves, are inertial-gravity waves forced by the boundary shape. They are important because they carry the energy and momentum of the mean flow higher up into the atmosphere, where it is deposited as the waves break up. These waves also play a role in mixing the fluid layer Wurtele *et al.* (1996). Lee wave generation creates a pressure drag on the boundary that is responsible for the transfer of angular momentum between the fluid and the solid. Due to all these effects, lee waves are important but cannot be tracked by numerical meteorological models and need to be parameterised (Palmer *et al.*, 1986; Mayer & Fringer, 2020). There is much to learn from these works, which are more advanced than the equivalent for the Earth's core (disregarding magnetic and deep layer effects). Therefore, the method used in this work can easily be related to the pioneering work of Bell (1975), which developed an analytical solution for internal waves forced by a topography. Studies on the atmosphere have the advantage of being supported by many in situ measurements and experiments. Numerical models benefit from these observations (a numerical result of Nikurashin & Ferrari (2010*b*) is given as an example in figure 1.7). This has allowed them to acquire a lot of knowledge about turbulent and supercritical flow regimes.

Topographic coupling is also of interest to the planetology community. Several moons of Saturn and Jupiter have oceans of liquid water under an ice shell (for review see Nimmo & Pappalardo, 2016). In these satellites, the lower boundary of the ice is a phase-change interface. The coupling of the icy shell with the underground water through spatial variation of the heat flux, phase change, or elasticity of the ice shell can generate a topography that will affect the dynamics of the fluid below (*e.g.* see Kihoulou *et al.*, 2023; Kvorka & Čadek, 2024, and references therein). Radar measurements (Zebker *et al.*, 2009) coupled with gravimetric data (Iess *et al.*, 2010) have revealed this type of ice-ocean interface topography (*e.g.* Nimmo & Bills, 2010, on Titan). We expect that the aspherical boundary of these oceans has an impact on the rotation of these satellites. For instance, topographic pressure coupling has been proposed to explain the variation of Titan LOD (Van Hoolst *et al.*, 2009).

The question of turbulence will not be addressed in this work but may be relevant to geophysical fluids. Among turbulent flows over topography, two limit cases are usually distinguished: the topography height is lower than the boundary layer, which is often called roughness, which has, for instance, been studied theoretically Gérard-Varet (2003*a*); Gérard-Varet (2003*b*); Gérard-Varet

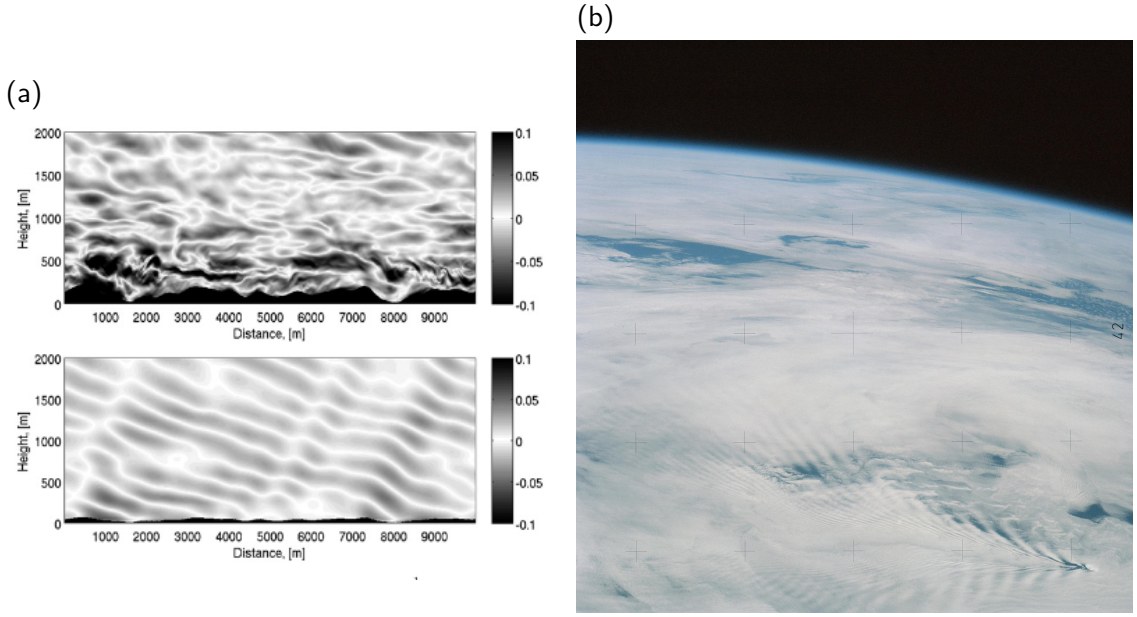

Figure 1.7: **(a)** Snapshot of the zonal velocity of a flow over topography in a numerical simulation of (top) Drake Passage and (bottom) the southeast Pacific. From Nikurashin & Ferrari (2010*a*). **b** Photographs taken from the Skylab space station illustrate an atmospheric internal lee wave pattern downstream of Bouvet Island. Credit: NASA (February 1974).

& Dormy (2006); Radko (2023*a*); Radko (2023*b*) or with numerical studies Chan & Chin (2023). In the opposite case, the topography directly interacts with the bulk of the fluid, preventing, for instance, any boundary layer parameterisation (e.g. through a logarithmic law of the wall). Numerical studies at large Reynolds numbers can then be quite challenging , and laboratory experiments are then particularly useful, notably to study non-linear and turbulent effects.

Gravity waves, internal gravity waves, and inertial gravity waves are crucial for geophysical fluids and have, therefore, motivated fluid experiments. Experimental observations of topographic inertial waves have been made for rapidly rotating fluids in a cylinder (Pedlosky & Greenspan, 1967; Pratte & Hart, 1991; Burmann & Noir, 2018) and a cylindrical annulus (Pfeffer *et al.*, 1993; Weeks *et al.*, 1997; Tian *et al.*, 2001), often with problems related to oceanic and atmospheric circulation (especially with links to circumpolar currents, see *e.g.* Maxworthy, 1977). Many studies aim to observe Rossby waves (Carnevale *et al.*, 1991; Pratte & Hart, 1991; Lemasquerier, 2021). Westerburg & Busse (2003) used an annulus with a top and bottom slope to reproduce planetary cores. On the other hand, many studies of internal waves have been based on experiments without rotation. These studies are often performed in canals (Long, 1955; Baines & Hoinka, 1985), or with topography on a conveyor belt (Aguilar & Sutherland, 2006; Aguilar *et al.*, 2006). For a complete review of stratified flows over topography, the reader is referred to Baines (2022). Rotating experiments with stratification and topography are less frequent. Some experiments have been performed with isolated topography (Boyer, 1987; Boyer & Zhang, 1989; Boyer & Davies, 2000) or a single ridge (Boyer & Biolley, 1986). The topography modelled by tilted slopes has

also been used in cylinders (Maxworthy & Browand, 1975; Baines *et al.*, 2005). For a review of experiments with topography, stratification, and rotation, see Boyer & Davies (2000). However, experiments that integrate rapid rotation and stratification are still needed to study the forcing of the drag of gravito-inertial lee waves on a (regular) topography (even more with parameters for which the results could be applied to the core).

1.2.2 Models of core-mantle coupling

Faced with the problems of LOD and nutations related to the core-mantle coupling, it has been necessary to develop dedicated models that incorporate the specific features of the core. The effect of the magnetic field is a key ingredient of the liquid-metal dynamics and can also be combined with topography, mantle conductivity, rotation, and stratification. The core is a thicker layer than the ocean and atmosphere, which does not allow the use of some of the approximations commonly used for surface fluids (*e.g.* shallow water). Although we know what value of the torque to expect, the origin of this torque is still debated (Roberts & Aurnou, 2012), and developing models that incorporate all of the above elements is not an easy task. Therefore, a large number of models have been developed to study all of these effects.

The first category of models uses global spherical geometry to calculate the torque. These models are used for gravity coupling since it is a non-local global force (Buffett, 1996). Global models are also particularly suitable for electromagnetic coupling models and have been used for the length of the day (Holme, 1998; Gillet *et al.*, 2015; Pichon *et al.*, 2016; Schwaiger *et al.*, 2024) and nutation applications (Buffett, 1992; Deleplace & Cardin, 2006). In any case, this coupling alone seemed insufficient on its own to explain the rotation data. Global models were also used for topographic coupling, recalculating the pressure field of the inverted core flow, and obtaining the torque from a topography model (Hide, 1989; Jault & Le Mouël, 1990; Kuang & Bloxham, 1993). The pressure field is calculated using the tangential geostrophy approximation, which is based on the fact that rotation is the dominant effect on the flow. This allows the pressure to be calculated using only the surface flow.

Another approach is to use local models. With this method, the flow (and the coupling) is calculated from the momentum equation in a Cartesian frame. This framework allows for a large set of mathematical methods, such as asymptotic methods, perturbation methods, or the use of plane waves. All of these techniques make it possible to add a host of features to the calculation. This has been widely used to estimate the topographic coupling at the CMB (Acheson, 1975; Moffatt, 1977; Hassan & Eltayeb, 1982; Braginsky, 1998) even in very recent papers (Glane & Buffett, 2018; Jault, 2020). Buffett (2010) also developed a model that mixes topographic and electromagnetic coupling to explain the out-of-phase component of the annual nutations. Recognising the limitations of the local model for long-wavelength topography, some studies have introduced global geometry effects, via β-plane effects (Braginsky, 1998; Jault, 2020), widely used for surface geophysical fluids. However, these local calculations have been performed under multiple (sometimes severe) assumptions, such as discarded induction and advection (Buffett, 2010), short topography wavelength (Glane & Buffett, 2018), or strong fluid stratification (Jault, 2020).

1.2.3 Aim and structure of the thesis

Building on recent works, our motivation aim here is to unlock previous limitations by developing an efficient local model of boundary coupling that can calculate the torque at values of the dimensionless numbers appropriate to the Earth's core. We also intend to take into account global geometry by β effects and variations with latitude. This model will also provide a better understanding of the physics of topographic and electromagnetic coupling by studying the physics of topographic waves, in particular. We also aim to bridge the gap between steady length of the day variation studies and nutation ones

The manuscript is structured as follows. In chapter 2, we first introduce the dynamical equations, the geometry, and the calculation method. We detail the specificity of our model. In chapter 3, we present our results for steady flows and geophysical applications for the variation of length of the day. We focus on the effects of global geometry through the β plane and Rossby waves, with also a study of the effect of magnetic field and dissipation on topographic coupling. We study the propagation of MAC steady waves forced by topography. Chapter 4 is dedicated to oscillating flows associated with nutation motion. The time periodicity will first allow us to compare our model with direct numerical simulations. We then investigate the effects of the base-flow oscillation frequency and introduce the effects of a conducting solid, to finish with geophysical applications. In the concluding chapter 5, we first show some ongoing work and short-term perspectives. In particular we use our method, which allows us to integrate over the surface of the CMB taking into account the spatial variation of the rotation and the magnetic field, to obtain more accurate values of the coupling. We then discuss the limitations of local periodic models. We conclude this study with a final remark and long-term perspectives as new implementations in the code or the links with laboratory experiments.

Summary of the chapter

- Using models, LOD and nutation measurements allow one to obtain accurate values of the fluid-solid (coupling) torque at the CMB thanks to rotation measurements.
- Dissipative coupling of nutations and length of day variations are difficult to explain with only an electromagnetic coupling.
- We aim at investigating the stress generated by a flow on a periodic topography.
- We will use our new model to study the propagation of topographic waves in a rotating, stratified, and electrically conducting fluid.
- This model will allow us to study both nutation motions and length of the day variations within the same framework.

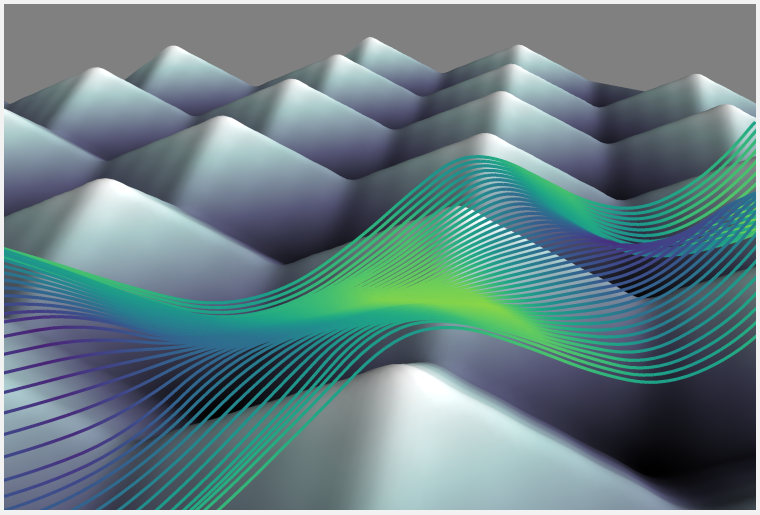

Figure 1.8: Three dimensional representation of velocity streamlines calculated with our code. The pyramidal topography is constructed from a polychromatic series of sinusoids.

2 Method

Contents

In this chapter, we describe the method used to obtain magneto-hydrodynamic flow over a bumpy topography. The problem is tackled in a local Cartesian frame. Then, we describe the transition from global to local problem, defining the geometry, the dynamical equations, and the method which allows us to introduce the effects of global geometry into the local model. Then, we present the boundary conditions on a bumpy boundary that can also be electrically conducting. We show how the different couplings at the boundary can be calculated. We have developed an original semi-analytical method to calculate the flow on the topography via a perturbation approach. The mathematical framework is described, followed by the resolution method used in our code.

2.1 Geometry and dynamical equations

2.1.1 Description of the problem

In this work, we investigate the boundary coupling between a planetary fluid layer and a solid domain (*e.g.* the solid inner core and/or the mantle). We focus on a spherical boundary with shape perturbations that are of small amplitude compared to the typical radius R. This geometry is then

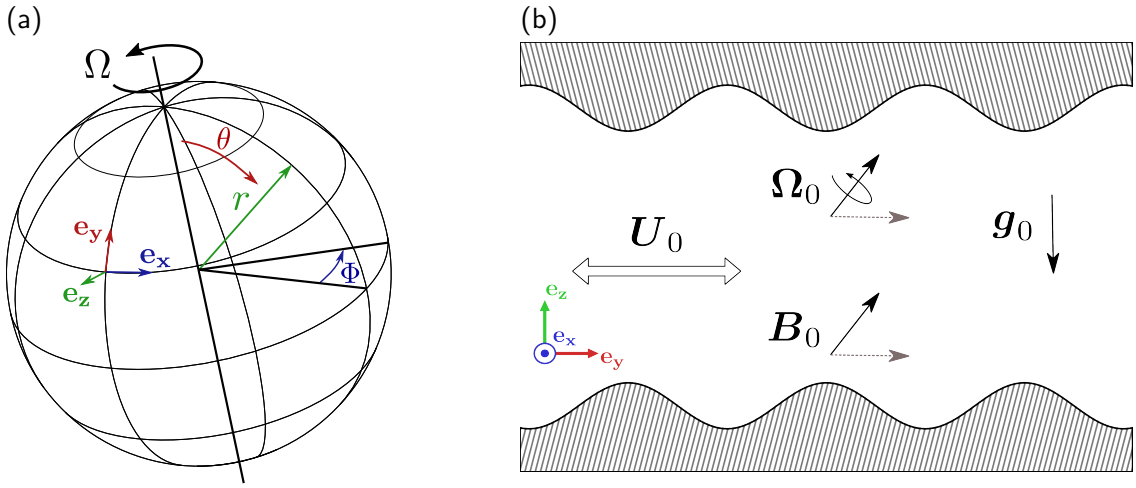

Figure 2.1: Perturbing the global geometry **(a)** by small wavelength topographies, a local Cartesian box model can be used **(b)**, imposing a basic flow $\boldsymbol{U}_0$ and a magnetic field $\boldsymbol{B}_0$ in a frame rotating at $\boldsymbol{\Omega}_0$, with the gravity vector $\boldsymbol{g}_0 = g_0\mathbf{1}_z$.

approximated by its tangent plane using a local model, and the problem is tackled in a periodic Cartesian frame. The spherical coordinate system $[\mathbf{1}_r, \mathbf{1}_\theta, \mathbf{1}_\Phi]$ (see figure 2.1a) is thus converted into a local frame with $\mathbf{1}_x = \mathbf{1}_\Phi$, $\mathbf{1}_y = -\mathbf{1}_\theta$ and $\mathbf{1}_z = \mathbf{1}_r$, with θ the colatitude r the radius and Φ the longitude. To account for planetary rotation, we work in the reference frame rotating at $\boldsymbol{\Omega}_0$, and the buoyancy effects are due to constant gravity $\boldsymbol{g}_0 = -g_0\mathbf{1}_z$ (figure 2.1b).

Assuming periodicity in the x and y directions, we first consider a semi-infinite fluid, which we then extend to a fluid layer enclosed between two boundaries. In both cases, boundary shapes can be three-dimensional (possibly time-dependent) polychromatic bumps (figure 2.3), which can be described with Fourier series

$$h(x,y,t) = z_0 + \epsilon_t \sum_j \Re\left[\mathrm{A}^{(j)} \mathrm{e}^{\mathrm{i}(\boldsymbol{k}_H^{(j)}\cdot\boldsymbol{r} - \omega^{(j)}t)}\right], \tag{2.1}$$

in dimensionless form. We note z_0 the boundary position without topographic perturbation. We note $\boldsymbol{r}$ the position vector, and for each topography component, $\mathrm{A}^{(j)}$ the amplitude, $\boldsymbol{k}_H^{(j)} = k_x^{(j)}\mathbf{1}_x + k_y^{(j)}\mathbf{1}_y$ the horizontal wave vectors in the $x-y$ plane, and $\omega^{(j)}$ the angular frequencies (*e.g.*, as required for rigid topographies studied in moving fluid frames, or for dynamical topography, Acheson, 1975). The relevant topography length for the flow is the one seen by the fluid along its motion. We choose the largest topography wavelength $1/\tilde{k}$ in the direction of the base flow as the unit of length. This defines the non-dimensional height $\epsilon_t = h_0\tilde{k} \ll 1$ of the topography, with h_0 the dimensional topography height (amplitude of the total topography). The parameter ϵ_t is considered small to handle the topography effects in a perturbative way.

We assume the presence of a basic flow $\boldsymbol{U}_0$ and magnetic field $\boldsymbol{B}_0$, of respective typical magnitudes $\tilde{U}$ and $\tilde{B}$. In the following, we use the time unit $1/(\tilde{U}\tilde{k})$ and the magnetic field unit $\tilde{U}(\rho_r\mu)^{1/2}$, using the fluid reference density ρ_r as the density unit and noting the fluid magnetic permeability

μ. Buoyancy effects are included in our model under the Boussinesq approximation. Assuming a linear equation of state for density changes, the dimensionless buoyancy $g_0\rho/(\tilde{U}^2\rho_r\tilde{k})$ is written as $a_0(z) + a$. The buoyancy anomaly a is then an unknown variable of the problem, and the dimensionless basic state $a_0(z)$ is characterised by the local (dimensional) Brunt-Väisälä frequency N through $N^2 = \tilde{U}^2\tilde{k}\partial_z a_0(z)$, where ∂_z denotes the partial differentiation with respect to z.

Considering a Newtonian fluid in the rotating frame of reference, the dimensionless velocity $\boldsymbol{u}$, the magnetic field $\boldsymbol{b}$, and the buoyancy anomaly a are thus governed by

$$\partial_t \boldsymbol{u} + (\boldsymbol{u}\cdot\nabla)\boldsymbol{u} = -2Ro^{-1}\boldsymbol{\Omega}\times\boldsymbol{u} - \nabla p + a\mathbf{1_z} + (\nabla\times\boldsymbol{b})\times\boldsymbol{b} + Re^{-1}\nabla^2\boldsymbol{u} \tag{2.2a}$$

$$\partial_t a + (\boldsymbol{u}\cdot\nabla)a = -u_z Fr^{-2} + Pe^{-1}\nabla^2 a, \tag{2.2b}$$

$$\partial_t \boldsymbol{b} = \nabla\times(\boldsymbol{u}\times\boldsymbol{b}) + Rm^{-1}\nabla^2\boldsymbol{b}, \tag{2.2c}$$

with the solenoidal constraints $\nabla\cdot\boldsymbol{u} = \nabla\cdot\boldsymbol{b} = 0$, and using the reduced pressure p which includes the centrifugal effect. Noting the fluid kinematic viscosity ν, the fluid magnetic diffusivity $\eta = (\mu\sigma)^{-1}$ with $\mu \approx \mu_0$ the permeability of the medium and μ_0 the one of the free space. σ is the electrical conductivity of the medium, and α the buoyancy diffusivity, we have used non-dimensional control parameters defined in Table 2.2. While the velocity and the density unknowns are only defined in the fluid domain, the magnetic field also has to be obtained in the conducting or insulating solid[1]. Then, two cases are considered. When the solid is insulating, the magnetic field $\boldsymbol{b}$ can be obtained from a scalar potential ψ using $\boldsymbol{b} = -\nabla\psi$ and $\nabla^2\psi = 0$. For an electrically conducting solid at rest, of uniform magnetic diffusivity η_s, $\boldsymbol{b}$ is governed by the diffusion equation

$$\partial_t \boldsymbol{b} = \tilde{\eta} Rm^{-1}\nabla^2\boldsymbol{b}, \tag{2.3}$$

with $\tilde{\eta} = \eta_s/\eta$ the ratio of fluid and solid (η_s) magnetic diffusivities.

In the following, we only consider the case of uniform stratification $a_0 \propto z$ and Fr is thus constant, our method only allowing for linear or periodic base density field. We will also consider the asymptotic limit $Re^{-1} = Pe^{-1} = 0$. Taking this limit has the advantage of removing the associated boundary layers. Their presence imposes indeed a severe upper bound on the maximum topography height ϵ_t that can be considered in our code (the perturbation approach requires ϵ_t being smaller than the viscous boundary layer thickness to ensure convergence of the series expansion, see section 2.4). This limitation is removed by considering an inviscid fluid.

[1] If pseudo-vacuum ($\boldsymbol{b}\times\boldsymbol{n} = 0$) or perfectly conducting ($\boldsymbol{b}\cdot\boldsymbol{n} = 0$) conditions are chosen, there is no need to know the field in the solid.

Parameters	Expression	$\tilde{k}^{-1} = 5$ km	$\tilde{k}^{-1} = 100$ km	Glane & Buffett (2018)
Rossby	$Ro = \tilde{U}\tilde{k}/\Omega_0$	2.74×10^{-4}	1.37×10^{-5}	4.32×10^{-4}
Froude	$Fr = \tilde{U}\tilde{k}/N$	2.74×10^{-4}	1.37×10^{-5}	2.16×10^{-5} - 4.32×10^{-4}
Magnetic Reynolds	$Rm = \tilde{U}/(\eta\tilde{k})$	6.25×10^{-1}	12.5	9.92
Reynolds$^{(a)}$	$Re = \tilde{U}/(\nu\tilde{k})$	5×10^5	10^7	∞
Peclet$^{(a)}$	$Pe = \tilde{U}/(\alpha\tilde{k})$	5×10^4	10^6	∞
Alfvén$^{(b)}$	$Al = \tilde{U}\sqrt{\rho_r\mu}/\tilde{B}$	2.24×10^{-2}	2.24×10^{-2}	8.62×10^{-2}
Global wavelength	$\chi = 1/\tilde{k}R$	1.43×10^{-3}	2.86×10^{-2}	0
Conductivity ratio$^{(a)}$	$\tilde{\eta} = \eta_s/\eta$	10^3	10^3	∞
Lehnert	$Le = Ro/Al$	1.22×10^{-2}	6.12×10^{-4}	5×10^{-3}
Elsasser	$\Lambda = RoRm/Al^2$	3.41×10^{-1}	3.41×10^{-1}	5.77×10^{-1}
Interaction parameter	Rm/Al^2	1.24×10^3	2.49×10^4	1.33×10^3

(a) Values for the Earth's core. But, unless specified, the calculations are for $Re^{-1} = Pe^{-1} = \tilde{\eta}^{-1} = 0$.

(b) Alfvén number does not appear in equation 2.2 but only through the amplitude of the basic magnetic field (equation 2.21).

Table 2.2: Expression of non-dimensional parameters used in this study and their typical values for Earth core-mantle boundary. We suppose $N/\Omega_0 = 1$ and that α is the thermal diffusivity. The value of $\tilde{U} = 10^{-4}\text{ms}^{-1}$ is the average zonal velocity at the CMB (Moffatt, 1977), and $\tilde{B} = 5 \times 10^{-4}\text{T}$ the typical magnitude of the magnetic field at the pole. We also show parameters used by Glane & Buffett (2018).

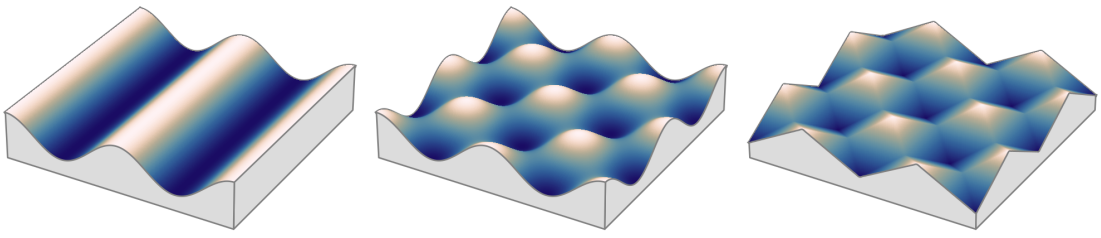

Figure 2.3: Typical topography handled by our code, from the simple 1D ridge shape (left) considered in previous studies (Buffett, 2010; Glane & Buffett, 2018; Jault, 2020), to the more complex and realistic 3D topographies considered in this work (middle: egg-box topography, right: pyramidal-egg-box topography).

2.1.2 Various β-plane approximations

The interaction between the sphericity of the Earth and its rotation introduces new physical effects, notably giving rise to what are referred to as Rossby waves (Cushman-Roisin & Beckers, 2011). In the case of local models, we have to capture these physics by adopting approximations that allow us to take into account these curvature effects. More generally, the so-called β-effect corresponds to the implications of Kelvin's circulation theorem (Bjerknes' theorem for rotating fluids) for barotropic fluids and of the conservation of potential vorticity, in spherical geometry. These theorems, detailed below, have a significant effect on the vorticity of the flow when subjected to variations in rotation or fluid height.

The conservation of potential vorticity is derived from the conservation of mass and energy (only true for adiabatic and diffusionless flows) and is helpful in understanding rotating flows (for an extensive picture of potential vorticity and its implication see chap. 4 of Vallis, 2017). Potential vorticity is a quantity proportional to the absolute vorticity $\boldsymbol{\zeta^a}$ multiplied by a vertical constraint on the fluid. In the case of a 2D flow, vertically bounded, as is the case for geostrophic flows and shallow water approximations, the conservation of potential vorticity is written as

$$D_t\left(\frac{\zeta_z^a}{h}\right) = D_t\left(\frac{(2Ro^{-1}\boldsymbol{\Omega} + \nabla\times\boldsymbol{u})\cdot\mathbf{1}_z}{h}\right) = 0 \tag{2.4}$$

with h the height of the fluid column and D_t the material derivative operator. This corresponds to Rossby's shallow layer potential vorticity (Rossby, 1939).

In the case of 3-dimensional and stratified flow, this equation is rather the conservation of the Ertel's potential vorticity (Ertel, 1942)

$$D_t\left(\boldsymbol{\zeta}^a\cdot\nabla a\right) = D_t\left[\left(2Ro^{-1}\boldsymbol{\Omega} + \nabla\times\boldsymbol{u}\right)\cdot\nabla a\right] = 0 \tag{2.5}$$

where the absolute vorticity is multiplied by the gradient of a materially conserved quantity, which is the buoyancy a. Looking at these equations, we can then separate β-effects into two families: Topographic-β and β-plane effects (Pedlosky, 2013).

Geometrical constraint: topographic β-effect

For topographic β-effect, the height of the fluid column (or its equivalent induced by stratification) is balanced with the vorticity to conserve the potential vorticity. For Earth applications, these topographic effects can be divided into two families: shallow and deep layer effects, which separate the ways of prescribing vertical variations of the flow.

For shallow topographic effects, the hydrostatic approximation imposes a z-invariance. The β effects are then due to the variation of the fluid height, which typically comes from a uniform bottom slope (*e.g.* the case of a coast with a varying bottom floor). This gives rise to the so-called topographic Rossby waves (Pedlosky, 2013). These waves exist locally in our framework, due to the topography, but better correspond in this case to the name inertial gravity waves, since these effects come from the small-scale topography and not from a length scale larger than the local box.

For deep topographic β-effect z-invariance comes from the Proudman-Taylor constraint in rotating fluid layers, such as the core. Deep β-effects are included in quasi-geostrophic (QG) calculations (Schaeffer & Cardin, 2005; Gillet & Jones, 2006; Gastine, 2019; Barrois *et al.*, 2022). When we directly derive equations from momentum conservation (following a method similar to Dellar (2011)), the full equation of Labbé *et al.* (2015), which describes β effects, can be obtained. Historically, QG models have used approximations of this equation. The height variation of the geostrophic column then introduces a corrective term in the equations, proportional to the gradient of the column height. At the equator, the slope becomes infinitely steep, invalidating this approach. This is not the case for the Labbé *et al.* (2015) equation (also used by Bardsley, 2018; Gerick *et al.*, 2020).

β-plane with varying Ω

The second β-effect comes from the variation in angle between the rotation vector and gravity due to the global shape. This is important for the flow either because of the hydrostatic assumption (for a free surface) or because the fluid is stratified. For shallow layers (*e.g.* oceans and atmosphere), the rotation vector $\mathbf{\Omega}$ is often simplified considering only its vertical component, which is the most influential since the velocity field is mainly horizontal. This approach is often called the f-plane approximation and is given by $\mathbf{\Omega} = \cos\theta \mathbf{1_z}$. For large length scale ($\chi = 1/(\tilde{k}R) \not\ll 1$), the local model needs to include curvature effects from the spherical geometry. For such perturbations, $\mathbf{\Omega}$ is no longer considered constant within the box. The β-plane corresponds to the series expansion of the f-plane for a small distance $\tilde{k}^{-1}y = \theta - \theta' R$ from a given colatitude θ. The dimensionless rotation vector is then expressed as

$$\mathbf{\Omega} = (\cos\theta + \chi y \sin\theta)\mathbf{1_z}, \tag{2.6}$$

which is relevant for thin fluid layers (Rossby, 1939). In a more general case it can be relevant to consider also the tangential component of the rotation vector, as

$$\mathbf{\Omega} = (\cos\theta + \chi y \sin\theta)\mathbf{1_z} + \sin\theta \mathbf{1_y}, \tag{2.7}$$

For deep layers, the so-called non-traditional β-plane includes, in addition, a linear variation $(\sin\theta - 2\chi y \cos\theta)\mathbf{1_y}$ for the tangential component (Grimshaw, 1975). It violates $\nabla\cdot\mathbf{\Omega} = 0$, necessary for the material conservation of the potential vorticity (Dellar, 2011). To solve this problem, an additional term $2\chi z \cos\theta \mathbf{1_z}$ is then required, related to the vertical variation of the radial component of $\mathbf{\Omega}$, which gives

$$\mathbf{\Omega} = \left[0, \quad \sin\theta - 2\chi y \cos\theta, \quad (1 + 2\chi z)\cos\theta + \chi y \sin\theta\right]^{\top}, \tag{2.8}$$

it corresponds to the equations 8.2 and 8.3 of Dellar (2011). The balance between the variation of the rotation vector and the vorticity (and possibly the stratification) gives rise to the so-called planetary Rossby waves (Longuet-Higgins, 1964). Note that planetary Rossby waves commonly refer to the 2D barotropic shallow layer expression of these waves. In our framework, we will prefer

to mention waves that involve β-plane, simply as Rossby waves. There is a direct analogy between planetary and topographic Rossby waves, since the dynamical equations are equivalent, changing the value of the prefactor of the term β (Cushman-Roisin & Beckers, 2011). This is useful for experimental setups. Using a rotating tank with a tilted bottom boundary can substitute for β-plane effects (for experiments of deep (QG) topographic β-effects see also Lemasquerier *et al.*, 2021).

These approximations of $\boldsymbol{\Omega}$ introduce linear dependencies in the equations. We take the curl of the equation 2.2a (called vorticity equations), which removes the unknown pressure and reveals the terms of β effect. Terms that still depend linearly on y and z are neglected, since the β-plane approximation is derived near $x = y = 0$. We need to remove two excess equations due to the solenoidal constraint on $\boldsymbol{b}$ and $\boldsymbol{u}$. We remove one of the horizontal equations for each of the induction and vorticity equations, depending on the orientation of the horizontal wave vector. To respect the symmetry of the problem, if $k_x \neq 0$ and $k_y = 0$, we remove the equation along x and if $k_y \neq 0$ and $k_x = 0$, we remove the one along y. If $k_x \neq 0$ and $k_y \neq 0$, we can choose any of them. In the end, we find the pressure field by resolving the component of equations 2.2a aligned with the base flow.

Polar and equatorial dynamics

Due to the spherical geometry, the effect of rotation is particular (and distinct) at both the pole and the equator.

At the pole, the leading order of the β-plane vanishes. To account for the variation of the rotation with latitude in polar regions, we are then required to consider the next higher-order term. This so-called γ (or δ) plane term arises from the Taylor series of the rotation vector, reading in its simpler form (Yang, 1987)

$$\Omega_z = \cos\theta + \underbrace{\chi y \sin\theta}_{=0 \text{ at the poles}} - \frac{(\chi y)^2}{2}\cos\theta + O(y^3). \tag{2.9}$$

Such a naive approach leads to a divergence of one component and has thus been later refined by Harlander (2005), showing that an additional term is required.

At the equator, the projection of the rotation vector on the gravity vector vanishes. Despite the numerous references to "equatorial β-planes" (*e.g.* Pedlosky, 2003; Boyd, 2018), these are nothing different from equation 2.6, and only highlight the absence of the 0-order f-plane term at the equator.

The symmetrical nature of the equator gives rise to several equatorial waves. These waves have the properties of being trapped at the equatorial latitude due to the β-plane effect. These include the equatorial Rossby waves, which are planetary Rossby waves. This also gives rise to equatorial Kelvin waves[2] for which the equator behaves like a solid coastline (Pedlosky, 2003). Finally, there are also Yanai waves, also known as mixed gravity-Rossby waves, that exist with the mixed influence of gravity and β-plane (Delplace & Venaille, 2019). These waves continuously transition between low-frequency Rossby waves and high-frequency Poincaré waves, whose restoring force is gravity.

[2]Kelvin waves are gravity waves that emerge in the presence of a coastline.

2.2 Boundary conditions

Boundary conditions complement the dynamical equations. When a semi-infinite geometry is considered, we impose the perturbations to vanish at infinity. In the following, we note with brackets [ ] the difference in quantities between both sides of the boundary and evaluated at $z = h$. We denote normal and tangential components by subscripts $_n$ and $_t$, respectively, which are calculated in practice using the unit normal vector $\boldsymbol{n} = \nabla F/|\nabla F|$, with $F(x, y, z, t) = z - h(x, y, t)$ as the boundary surface.

2.2.1 Kinematic conditions

On an arbitrary boundary, the normal kinematic boundary condition is $\mathrm{D}_t F|_{z=h} = 0$, which gives $\boldsymbol{u} \cdot \nabla F|_{z=h} = -\partial_t F|_{z=h}$. This boundary condition can be rewritten more simply, as

$$u_n - u_{sn} = 0, \tag{2.10}$$

with u_{sn} is the normal velocity of the boundary. It reduces to $\boldsymbol{u} \cdot \boldsymbol{n} = u_n = 0$ for steady boundaries and ensures that the fluid and the boundary move consistently and is sufficient to close the equations for inviscid fluids.

More conditions for the tangential components of $\boldsymbol{u}$ are required in the general case of viscous fluids, such as the no-slip condition

$$[\boldsymbol{u}_t] = \boldsymbol{0}. \tag{2.11}$$

We can also impose the continuity of the stress (called stress-free conditions if one medium is a solid or an inviscid fluid)

$$[(\boldsymbol{\sigma} \cdot \boldsymbol{n})_t] = \boldsymbol{0}, \tag{2.12}$$

with the dimensionless viscous stress tensor $\boldsymbol{\sigma} = Re^{-1} \left(\nabla \boldsymbol{u} + (\nabla \boldsymbol{u})^\top\right)/2$.

2.2.2 Magnetic conditions

The magnetic field normal component is continuous across the boundary.

$$[b_n] = 0. \tag{2.13}$$

However, when the solid is considered to be perfectly conducting, surface electrical currents may arise. Then, the tangential component can be discontinuous

$$[\boldsymbol{b}_t] = -\boldsymbol{n} \times \boldsymbol{\mathcal{J}}, \tag{2.14}$$

with $\boldsymbol{\mathcal{J}}$ the surface current density. These magnetic field conditions are sufficient for insulating solid domains, but in the general case they must be complemented by continuity conditions on the tangential components of the electrical field $\boldsymbol{E}$. When looking at a moving interface, the boundary conditions on $\boldsymbol{E}$ are modified, and we must therefore pay close attention to the reference frame (Thorne & Blandford, 2017). The electrical field is modified in a moving reference frame as $\boldsymbol{E'} =$

$\boldsymbol{E} + \boldsymbol{u} \times \boldsymbol{b}$. Integrating the Faraday law $\nabla \times \boldsymbol{E} = -\partial_t \boldsymbol{b}$ on a circuit moving with the boundary, we obtain the following

$$[\boldsymbol{E'}_t] = [\boldsymbol{E}_t + (u_{sn}\boldsymbol{n} \times \boldsymbol{b})_t] = \boldsymbol{0}. \tag{2.15}$$

The condition is then modified by the boundary velocity only if $\boldsymbol{b}$ is discontinuous, that is, if there is a surface current $\boldsymbol{\mathcal{J}}$. Note that the velocity in this expression is normal to the boundary, since $\boldsymbol{E}$ is modified by the velocity of the reference frame we consider. Rekier *et al.* (2023) have recently reconsidered the boundary condition on $\boldsymbol{E}$, arguing that the correct one includes the sliding velocity of the fluid on the interface. In the case of a tangential velocity discontinuity (stress-free), the additional term of equation 2.15, which reads, in this case, $(\boldsymbol{u} \times \boldsymbol{b})_t$, becomes thus non-zero[3]. This is opposed to the common approach (Thorne & Blandford, 2017) and is not the one to adopt. Indeed, the continuity equation results from the Stokes theorem applied to the Maxwell-Faraday equation for the change in the electrical field. This transformation necessitates that the Maxwell-Faraday equation is written in the same reference frame on either side of the boundary.

To implement these boundary conditions for our problem, we need to express it as a function of the magnetic field $\boldsymbol{b}$. We then use Ohm's law in a local moving frame, $\boldsymbol{j} = Rm(\boldsymbol{E} + \boldsymbol{u} \times \boldsymbol{b})$ as well as Ampere's law $\nabla \times \boldsymbol{b} = \boldsymbol{j}$. We obtain

$$\left[\frac{\mathcal{E}\nabla \times \boldsymbol{b}}{Rm} - (\boldsymbol{u} \times \boldsymbol{b}) + (u_{sn}\boldsymbol{n} \times \boldsymbol{b})\right]_t = \boldsymbol{0}, \tag{2.16}$$

with $\mathcal{E} = 1$ in the fluid and $\mathcal{E} = \tilde{\eta}$ in the solid.

2.3 General expression of the boundary stress

Through the pressure, viscous, and electromagnetic forces, the flow generates stresses on the boundary. The force $\boldsymbol{F}$ on the solid is written as

$$\boldsymbol{F} = \int_S p\boldsymbol{n}\,\mathrm{d}S - \int_S Re^{-1}\left[(\nabla \boldsymbol{u}) + (\nabla \boldsymbol{u})^\top\right]\boldsymbol{n}\,\mathrm{d}S + \int_V (\nabla \times \boldsymbol{b}) \times \boldsymbol{b}\,\mathrm{d}V, \tag{2.17}$$

with $\boldsymbol{n}$ the normal vector pointing inward of the solid, S the fluid-solid boundary surface and V the solid volume. The Lorentz force can also be obtained by integration on a closed surface (Roberts & Aurnou, 2012), writing it as $(\nabla \times \boldsymbol{b}) \times \boldsymbol{b} = \nabla \cdot \boldsymbol{\sigma^M}$, with the Maxwell stress tensor $\sigma^M_{i,j} \equiv b_i b_j - (b^2/2)\delta_{i,j}$ and the Kronecker symbol $\delta_{i,j}$. Equation 2.17 is thus transformed into

$$\langle \boldsymbol{F} \rangle = \frac{1}{S}\left(\int_S p\boldsymbol{n}\,\mathrm{d}S - \int_S Re^{-1}\left[(\nabla \boldsymbol{u}) + (\nabla \boldsymbol{u})^\top\right]\boldsymbol{n}\,\mathrm{d}S + \oint_{S_2}\left((\boldsymbol{n}\cdot\boldsymbol{b})\boldsymbol{b} - \frac{1}{2}b^2\boldsymbol{n}\right)\mathrm{d}S\right), \tag{2.18}$$

with S_2 the closed surface of the volume V. The brackets $\langle\rangle$ indicate the horizontal spatial average on x and y. In our model, the solid has a semi-infinite extent, where we need to satisfy our boundary condition of vanishing perturbation at infinity. For a steady flow on a conducting solid, the basic state has a linear vertical dependency, which does not satisfy our boundary condition (apart from a null perturbation). This linear dependency also introduces a non-physical infinite force on the

[3] while it should only be non-zero in the case of a current sheet at the interface.

solid. This problem can be solved by adding a second boundary, delimiting a conducting and layer and a semi-infinite insulating solid.

For oscillating flows, an exponential boundary layer emerges, solving this issue (see chapter 4). The decay length of the magnetic field perturbation, called the magnetic skin thickness δ, depends on the oscillation frequency ω as $\delta = \sqrt{2\tilde{\eta} Rm^{-1}\omega^{-1}}$ (Buffett, 2010). In the stationary case, δ is infinite. When $\boldsymbol{b}$ is periodic in the horizontal directions and vanishes at infinity, the integration on S_2 reduces to integration on the topography surface[4] S, and the mean force $\langle \boldsymbol{F} \rangle$ on the solid can finally be obtained as

$$\langle \boldsymbol{F} \rangle = \frac{1}{S} \int_S \left(p\boldsymbol{n} - Re^{-1} \left[(\nabla \boldsymbol{u}) + (\nabla \boldsymbol{u})^\top \right] \boldsymbol{n} + (\boldsymbol{n} \cdot \boldsymbol{b})\boldsymbol{b} - \frac{\boldsymbol{b}^2}{2}\boldsymbol{n} \right) \mathrm{d}S, \tag{2.19}$$

To estimate the stress, the unit normal vector $\boldsymbol{n} = \nabla F / |\nabla F|$ can be calculated exactly and used at the exact location of the boundary (which is done in the code, e.g. to evaluate $p\boldsymbol{n}$ at the boundary). To illustrate the discussion in the following, we provide the leading order of the series expansion of $\boldsymbol{n}$,

$$\boldsymbol{n} = \left[-\epsilon_t \partial_x h(x,y) + O(\epsilon_t^3), -\epsilon_t \partial_y h(x,y) + O(\epsilon_t^3), 1 + O(\epsilon_t^2) \right]. \tag{2.20}$$

Looking at this expression we see that the boundary horizontal stress 2.18 induced by the topography perturbation is of the order ϵ_t^2, which requires a priori a challenging second-order calculation. For the horizontal stress on the solid side, it appears in some cases that it can be obtained from simpler first-order linear solutions. The form of the horizontal component of the normal vector 2.20 which has no zeroth order, allows us to obtain the second-order horizontal pressure stress from the linear solution (Glane & Buffett, 2018; Jault, 2020). This can easily be extended to higher orders (*e.g.* order 2 solutions provide the tangential pressure stress at order 3). Note that this is not the case for viscous stress, which can only be calculated with a full second order.

Horizontal force on a stress-free boundary

Sometimes it is assumed that the stress-free boundary condition ensures zero drag on the boundaries. This is true only in the absence of topography. In fact, this boundary condition only ensures zero tangential stress. In the presence of topography, the sum of local normal stresses can produce a net drag (in the flow direction). This was also stressed for stress-free ellipsoids by Vidal & Cébron (2023).

2.4 Numerical method

2.4.1 Perturbative expansions

Starting from an imposed basic state for $\epsilon_t = 0$ (flat boundary), our objective is to calculate the perturbations due to topography. A direct integration of the dynamical equations is possible using a

[4] For a uniform $\boldsymbol{b}_0 = b_x \mathbf{1}_x + b_z \mathbf{1}_z$ the local Maxwell stress $(\boldsymbol{n} \cdot \boldsymbol{b})\boldsymbol{b} = b_z b_x \mathbf{1}_x$ is non-zero even for an insulating solid if integrated on S. Therefore, the integration must be performed on the closed contour S_2.

(brute-force) numerical method (*e.g.* finite element method), but it would not allow us to cope with planetary parameters or, more generally, to calculate flows with very small diffusivities. Instead, we follow an alternative approach, linearising the equations with perturbative expansions of the non-linear terms.

To express the perturbation caused by the topography, we write the variables as

$$\boldsymbol{u} = \boldsymbol{u}_0 + \sum_{m=1} \epsilon_t^m \boldsymbol{u}_m, \quad \boldsymbol{b} = Al^{-1}\boldsymbol{b}_0 + \sum_{m=1} \epsilon_t^m \boldsymbol{b}_m, \quad a = \sum_{m=1} \epsilon_t^m a_m, \tag{2.21}$$

The series expansion in ϵ_t allows us to linearise the equations for weak topography slopes. This approach is suitable if the basic states are steady and uniform (Jault, 2020) or if the non-linear terms are fully discarded in the dynamical equations (Buffett, 2010).

Indeed, nonlinearities can arise from two sources: the boundary conditions and the non-linear terms of dynamical equations. For the second one, a non-linear cascade arises if the basic state is varying in space and/or time. By cascade we mean that in the non-linear term, the spatial or temporal dependencies will multiply, creating a new term of shorter wavelength, which must be added to the solution at the same order. This will iteratively create an infinite number of increasingly small-scale terms within the same order[5]. To solve this issue, we then define a formalism that allows us to linearise all non-linear terms. To do that, the (dimensionless) imposed basic flow $\boldsymbol{u}_0 = \boldsymbol{U}_0/\tilde{\boldsymbol{U}}$ is written as $\boldsymbol{u}_0 = \boldsymbol{u}_{su} + \epsilon_v \tilde{\boldsymbol{u}}$, where $\tilde{\boldsymbol{u}}$ is a departure from a uniform steady flow $\boldsymbol{u}_{su}$, and ϵ_v is the parameters to be used for the series expansion. This decomposition is required if we want the basic field to be time or spatially dependent (and if we want to take into account weakly non-linear effects): oscillating velocity, viscous boundary layers, or flow on conducting solid, etc.

Calculation of boundary layers (through series expansions)

In certain cases, we want to construct a basic field that is uniform and steady far from the boundary, but that also satisfies the boundary conditions through an additional boundary layer flow (that needs to be obtained). In these cases, $\tilde{\boldsymbol{u}}$ and $\boldsymbol{u}_{su}$ (and similarly $\tilde{\boldsymbol{b}}$ and $\boldsymbol{b}_{su}$) must be of the same order ϵ_v. The uniform steady component $\boldsymbol{u}_{su}$ should be included in $\tilde{\boldsymbol{u}}$

In this work, the imposed magnetic field $Al^{-1}\boldsymbol{b}_0 = \boldsymbol{B}_0/(\tilde{U}\sqrt{\rho_r \mu})$ will always be assumed to be uniform and steady[6]. The perturbations from the basic state are obtained with the double-perturbation expansion

$$\boldsymbol{u} = \boldsymbol{u}_0 + \sum_{m,n=0} \epsilon_t^m \epsilon_v^n \boldsymbol{u}_{m,n}, \quad \boldsymbol{b} = Al^{-1}\boldsymbol{b}_0 + \sum_{m,n=0} \epsilon_t^m \epsilon_v^n \boldsymbol{b}_{m,n}, \quad a = \sum_{m,n=0} \epsilon_t^m \epsilon_v^n a_{m,n}, \tag{2.22}$$

where $\boldsymbol{u}_{0,0} = \boldsymbol{b}_{0,0} = \boldsymbol{0}$ and $a_{0,0} = 0$.

Combining the expansions 2.22 with the dynamical equations, we get a hierarchy of linear forced problems that can be solved iteratively. We use the same expansion for the pressure and

[5]For uniform and steady basic states, the non linear terms will only add new spatial and time dependences (of shorter wavelength) to the higher orders ($n \geq 2$), which remains tractable.

[6]Otherwise, similarly to $\boldsymbol{u}_0$, a new ϵ_b variable can be used in series expansions of $\boldsymbol{b}_0$ (not needed if ϵ_b is of the order of ϵ_t or ϵ_v).

calculation of the surface stress. Since we integrate on a curved boundary, the surface element used in equation 2.19 dS, is written as

$$\mathrm{d}S = \sqrt{\epsilon_t^2 \left(\partial_x h(x,y)\right)^2 + \epsilon_t^2 \left(\partial_y h(x,y)\right)^2 + 1}. \tag{2.23}$$

For illustration, it can also be written as a series expansion,

$$\mathrm{d}S = 1 + \epsilon_t^2 \left(\frac{\left(\partial_x h(x,y)\right)^2}{2} + \frac{\left(\partial_y h(x,y)\right)^2}{2} \right) + O\left(\epsilon_t^3\right) \mathrm{d}x\mathrm{d}y. \tag{2.24}$$

We see that this introduces a correction on the stress for orders $m > 2$.

We write the unknown perturbations $(\boldsymbol{u}_{m,n}, \boldsymbol{b}_{m,n}, a_{m,n})$ as a sum of harmonic plane waves of wave vector $\boldsymbol{k}^{(j)}$ and pulsation $\omega^{(j)}$. For the part of the flow forced by the non-linearities, $\omega^{(j)}$ and $\boldsymbol{k}^{(j)}$ are given directly by the terms of previous orders. The second part of the flow arises from the boundary conditions, which give the horizontal part $\boldsymbol{k_H}^{(j)} = k_x^{(j)}\mathbf{1}_x + k_y^{(j)}\mathbf{1}_y$ of $\boldsymbol{k}^{(j)}$. For each $\boldsymbol{k_H}^{(j)}$, the (homogeneous) dynamical equations provide $k_z^{(j)}$.

Example of perturbed equations

The order $\epsilon_t^0\epsilon_v^0$, $\epsilon_t^1\epsilon_v^0$ and $\epsilon_t^0\epsilon_v^1$ being straightforward to calculate, we show as an example the equations at order $\epsilon_t^1\epsilon_v^1$

$$\begin{aligned}\partial_t \boldsymbol{u}_{1,1} + (\boldsymbol{u}_{0,1}\cdot\nabla)\boldsymbol{u}_{1,0} + (\boldsymbol{u}_{1,0}\cdot\nabla)\boldsymbol{u}_{0,1} + (\boldsymbol{u}_{0,0}\cdot\nabla)\boldsymbol{u}_{1,1} = 2Ro^{-1}\boldsymbol{\Omega}\times\boldsymbol{u}_{1,1} - \nabla p_{1,1} \\ + a_{1,1}\mathbf{1_z} + Al^{-1}\left[(\nabla\times\boldsymbol{b}_{1,1})\times\boldsymbol{b}_{0,0}\right] + (\nabla\times\boldsymbol{b}_{0,1})\times\boldsymbol{b}_{1,0} + (\nabla\times\boldsymbol{b}_{1,0})\times\boldsymbol{b}_{0,1},\end{aligned} \tag{2.25}$$

$$\partial_t a_{1,1} + (\boldsymbol{u}_{0,1}\cdot\nabla)a_{1,0} + (\boldsymbol{u}_{1,0}\cdot\nabla)a_{0,1} = -(\boldsymbol{u}_{1,1}\cdot\mathbf{1}_z)Fr^{-2} + Pe^{-1}\nabla^2 a_{1,1}, \tag{2.26}$$

$$\begin{aligned}\partial_t \boldsymbol{b}_{1,1} = Al^{-1}\nabla\times(\boldsymbol{u}_{1,1}\times\boldsymbol{b}_{0,0}) + \nabla\times(\boldsymbol{u}_{0,0}\times\boldsymbol{b}_{1,1}) + \nabla\times(\boldsymbol{u}_{1,0}\times\boldsymbol{b}_{0,1}) \\ + \nabla\times(\boldsymbol{u}_{0,1}\times\boldsymbol{b}_{1,0}) + Rm^{-1}\nabla^2\boldsymbol{b}_{1,1},\end{aligned} \tag{2.27}$$

$$\nabla\cdot\boldsymbol{u}_{1,1} = \nabla\cdot\boldsymbol{b}_{1,1} = 0 \tag{2.28}$$

Note that some terms of this order are zero (*e.g.* $(\boldsymbol{u}_{1,1}\cdot\nabla)\boldsymbol{u}_{0,0}$) as $\boldsymbol{u}_{0,0}$ and $\boldsymbol{b}_{0,0}$ are uniform.

2.4.2 Basic states

A relevant basic state for planetary studies is provided by the solid body rotation around $\boldsymbol{\Omega}_0$ in the spherical geometry, leading to a uniform and steady basic flow $\boldsymbol{u}_0 = \sin\theta\mathbf{1_x}$ in the local model. We can also consider an oscillating flow, which is appropriate for tidal flows or motions forced by precession/nutation (Buffett, 2010, 2021). This kind of flow consists of an equatorial rotation and leads to a more complex 2D oscillating flow in the local geometry, written as (Buffett, 2010, 2021)

$$\boldsymbol{u}_0 = \left[-\cos\theta\cos(\omega t+\phi), \quad \sin(\omega t+\phi), \quad 0\right]. \tag{2.29}$$

Nutation and precession forcings lead to an equatorial rotation of the flow. For the libration motion (rotation along the rotation axis), performing local calculations in the fixed topography reference frame requires one to include a time oscillating $\mathbf{\Omega}$. This can be introduced in the framework of our code.

For simplicity, the basic magnetic field is considered to be uniform and steady in each local box model, varying in angle and magnitude as a function of the position of the local model with respect to the global geometry. Approximating the magnetic field as a dipole, we use

$$\boldsymbol{b}_0 = \left[0, \quad \sin\theta/2, \quad -\cos\theta\right]. \tag{2.30}$$

.

A magnetic β-plane

Following the principle of the β-plane for the rotation vector, we investigated the implementation of a "magnetic β-plane" that would use the same first-order spatial variations. Introducing linear variation in colatitude we obtain

$$\boldsymbol{b_0} = \left[0, \quad \sin\theta/2 - \chi y\cos\theta, \quad -\cos\theta - \chi y\sin\theta\right]. \tag{2.31}$$

We note that this approximation break the solenoidal constraint $\nabla\cdot\boldsymbol{B} = 0$ (as is it the case for $\mathbf{\Omega}$). In the same way as Dellar (2011), we need to introduce a vertical variation on the vertical component of $\boldsymbol{B}$, as

$$\boldsymbol{b_0} = \left[0, \quad \sin\theta/2 - \chi y\cos\theta, \quad (-1+\chi z)\cos\theta - \chi y\sin\theta\right]. \tag{2.32}$$

This introduces difficulties since $\boldsymbol{b_0}$ is included in the boundary conditions. This means that the perturbation must also allow for linear variations. This is not currently possible with our code, but could be implemented in the future. In practice, we then only use the uniform components of $\boldsymbol{b}_0$. Note that this can also be applied to the latitudinal variation of the velocity field, which is a key element for Ekman's pumping in spherical geometry. This initial exploration should be pursued for future models by rigorously defining the mathematical framework for this approximation and being cautious about its implementation.

2.4.3 Our semi-analytical code ToCCo

At each order, the perturbed unknowns $(\boldsymbol{u}_{m,n}, \boldsymbol{b}_{m,n}, a_{m,n})$ are searched as plane wave series forced by the previous order (*e.g.* the basic state) and boundary conditions. In this study, our aim is to go beyond the linear solution following previous approaches (Braginsky, 1998; Glane & Buffett, 2018; Jault, 2020). The double perturbative expansion 2.22 then has to be obtained at order m or n larger than 2, yielding higher accuracy and enabling the investigation of weakly non-linear effects. The orders are solved in an increasing way. For example, order $\epsilon_t^2\epsilon_v$ requires having previously calculated orders ϵ_v, ϵ_t, $\epsilon_t\epsilon_v$, and ϵ_t^2.

The solution is expressed as the sum of exponentials of the form $\sum_j \exp[\mathrm{i}(k_x^{(j)}x + k_y^{(j)}y + k_z^{(j)}z - \omega^{(j)}t)]$. Introducing this ansatz into equations 2.2, we obtain a linear system $\boldsymbol{AX} = \boldsymbol{c}$, which is non-homogeneous for orders $m + n \geq 2$ (*i.e.* $\boldsymbol{c} \neq \boldsymbol{0}$, where $\boldsymbol{c}$ consists of the nonlinear terms arising from previous orders). The homogeneous part of the solution is obtained by considering each horizontal harmonic separately. To ensure the existence of nonzero solutions, the zero determinant constraint provides the required values of $k_z^{(j)}$ (since the solution is not unique, the set of solutions is denoted $k_z^{(j,k)}$). To find all the solutions, we express the determinant in the form of a polynomial. We use the Berkowitz (1984) algorithm, which provides the determinant in the form of a fraction-free polynomial. Note that the degree of this polynomial is equal to the number of boundary conditions. For half-space, we only keep the modes for which the imaginary part of k_z yields a solution vanishing at infinity. Some polynomial determinants are therefore not analytically solvable due to their high degree (*e.g.* if there are two boundaries, a non-zero viscosity, or a solid conductor), which led us to use a numerical method. We numerically find each of the roots using the *polyroots* function of *mpmath*, based on the *Durand-Kerner* algorithm (Kerner, 1966).

For each $k_z^{(j,k)}$, we calculate the associated nonzero solution(s) $\boldsymbol{K}_{jk}$, called null spaces or kernel. Null spaces are found using the singular value decomposition of the matrix, which is based on the Golub & Reinsch (1971) algorithm. We again use a numerical method since the analytical calculation of matrix kernel is very expensive, except for simple cases that are tractable by symbolic calculations. The eigenvalues $k_z^{(j,k)}$ can be degenerate. In such a case, they yield several solutions $\boldsymbol{K}_{jk}$. In the following, we consider that the list $(k_z^{(j,k)})$ contains all k_z, even identical ones, and their associated solution $\boldsymbol{K}_{jk}$. The homogeneous solution vector is thus written as

$$\sum_j \left[\exp[\mathrm{i}(k_x^{(j)}x + k_y^{(j)}y)] \sum_k \left(C_{jk}\boldsymbol{K}_{jk} \exp(\mathrm{i}k_z^{(j,k)}z) \right) \right]. \tag{2.33}$$

For particular solutions, k_z is obtained directly from the expression of non-linear terms. It turns out that these k_z are not eigenvalues of $\boldsymbol{A}$, and consequently, we can solve the linear system $\boldsymbol{AX} = \boldsymbol{c}$. Finally, when the particular and homogeneous solutions are added, the constants C_{jk} are obtained from the boundary conditions.

Reference frames: non-zero base flow or moving boundary ?

Physics does not depend on the frame of reference. A steady, uniform base flow on a motionless boundary or the associated setup with a moving solid over fluid at rest is thus equivalent. However, switching from one to the other is not easy. Since none of the medium is time-dependent, one might think that a suitable plane-wave ansatz can be $\exp(\mathrm{i}(k_x x + k_y y + k_z z))$. This implies that the equations of motion are not identical because $(\boldsymbol{u}_{su}\cdot\nabla)\boldsymbol{u}$ is zero at order 1 in the second case. The ansatz needs to be chosen according to the boundary conditions. For a solid that moves horizontally, the fluid sees an oscillating boundary. For a boundary that moves at $u_{su}\mathbf{1}_x$ and a ridge-shaped topography, we have $n_x = \partial_x\left(\cos\left(k_x x\right)\cos\left(u_{su}k_x t\right)\right)$. This gives the ansatz $\exp(\mathrm{i}(k_x x + k_z z + u_{su}k_x t))$. We obtain

$$\partial_t \boldsymbol{u} = \mathrm{i}u_{su}k_x\boldsymbol{u}\exp(\mathrm{i}(k_x x + k_z z + u_{su}k_x t)), \tag{2.34}$$

which is equivalent, in the solid frame, to

$$(\boldsymbol{u}_{su}\cdot\nabla)\boldsymbol{u} = u_{su}\partial_x\boldsymbol{u} = \mathrm{i}u_{su}k_x\boldsymbol{u}\exp(\mathrm{i}(k_x x + k_z z)). \tag{2.35}$$

While flows naturally differ between reference frames, we thus recover the same vertical variations k_z in both cases. When $\boldsymbol{u}_{su}$ oscillates, a similar situation occurs (with fictitious forces related to the non-inertial oscillating frame).

The calculation involves a host of k_z wavenumbers, which results in very large expressions. To tackle this difficulty and the extreme values of the dimensionless parameters, we combine symbolic and arbitrarily precise calculations and perform linear algebra automatically. In our code, written in Python, symbolic calculations are achieved using the "Sympy" package (Meurer *et al.*, 2017). Extreme parameters can lead to badly conditioned matrices. Handling these matrices requires high-precision calculations, which are performed with the arbitrary precision package "mpmath" (The mpmath development team, 2023). The code is then fast enough to allow systematic exploration of parameter ranges. Typically, calculation at order 4 requires about ten hours on one computing core, for the simplest case of one harmonic topography, an inviscid fluid, and an insulating mantle.

2.4.4 Non-uniform basic states: example of Hartmann flow

For some configurations, notably for no-slip viscous flows and for a conducting solid, a uniform flow does not respect all the boundary conditions on a flat boundary. This requires a basic state that varies in space $(\tilde{b}, \tilde{u})$. The basic flow is then written as equation 2.22. As an illustrating example, we present in this section the derivation of a Hartmann layer (Jackson & Fox, 1999; Davidson & Belova, 2002; Dormy & Soward, 2007), which is a viscomagnetic boundary layer in the absence of rotation and stratification. This flow can be calculated by the code (to which topographic effects can then be added). Our code is able to handle weakly non-linear effects.

Here we consider a basic flow $\boldsymbol{u}_0 = \mathbf{1}_x$ and a basic magnetic field $\boldsymbol{b}_0 = Al^{-1}\mathbf{1}_z$ between two planes at $z = D$ and $z = -D$. This flow does not respect the no-slip boundary condi-

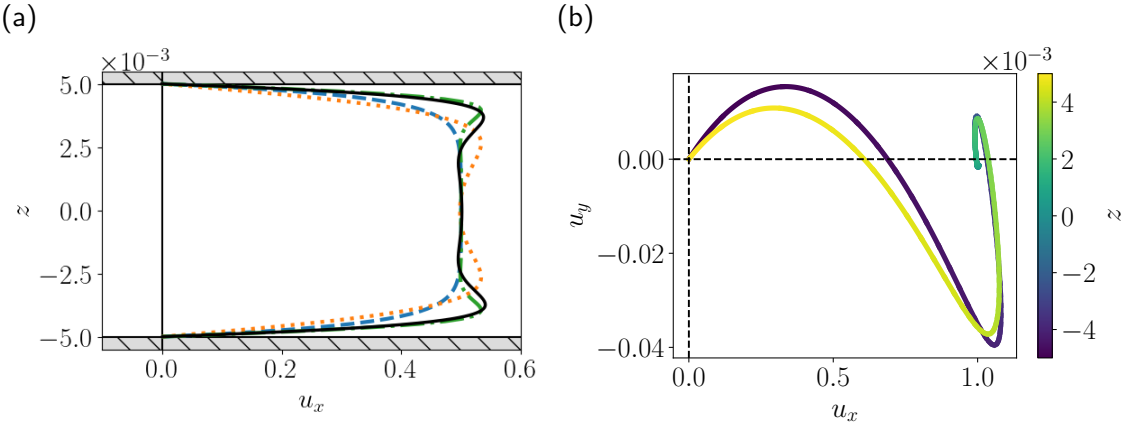

Figure 2.4: Illustrating case of Stokes-Ekman-Hartmann flow, considering a base flow oscillating as $\boldsymbol{u}_0 = \epsilon_v \cos(5\times10^5 t)\mathbf{1}_x$ at $t = 0$, in a rotating frame with $\boldsymbol{\Omega} = \mathbf{1}_z$ and $Ro = 2\times10^{-5}$, with a magnetic base field $\boldsymbol{b}_0 = \mathbf{1}_z$, and calculated at the order ϵ_v^2. **(a)** Compares u_x at order ϵ_v^2 (black line) to classical linear Ekman (dotted orange, $\boldsymbol{u}_0 = \epsilon_v\mathbf{1}_x$, $\boldsymbol{b}_0 = \mathbf{0}$, $Ro = 2\times10^{-5}$), Stokes (dashed-dotted green, $\boldsymbol{u}_0 = \epsilon_v \cos(5\times10^5 t)\mathbf{1}_x$ at $t = 0$, $\boldsymbol{b}_0 = \mathbf{0}$, $Ro^{-1} = 0$) and Hartmann (dashed blue, $\boldsymbol{u}_0 = \epsilon_v\mathbf{1}_x$, $\boldsymbol{b}_0 = \mathbf{1}_z$, $Ro^{-1} = 0$) flows. **(b)** u_x and u_y as a function of depth (colour). Parameters: $Al = 0.008$, $Rm = 12.5$, $Fr = 0$, $Re = 20$, $\chi = 0$, $\epsilon_v = 0.5$, $\tilde{\eta}^{-1} = 0$.

tions at the boundaries. We introduce a vertical variation $\exp(k_z z)$ and use the ansatz $\boldsymbol{u} = \boldsymbol{u}_0 + \left[u'_x, u'_y, u'_z\right]\exp(k_z z)$, $\boldsymbol{b} = \boldsymbol{b}_0 + \left[b'_x, b'_y, b'_z\right]\exp(k_z z)$ and $p = p_0 + p'\exp(k_z z)$. Since there is no rotation for the Hartmann layer and the basic magnetic field is along the z axis, the problem is 2D and $u'_y = b'_y = 0$. Due to solenoidal constraints $u'_z = b'_z = 0$. Taking this into account, the z component of the momentum equation is $k_z p' = 0$, then $p' = 0$. The equations set is then

$$k_z^2 u'_x Re^{-1} + b'_x k_z Al^{-1} = 0, \tag{2.36a}$$

$$k_z^2 b'_x Rm^{-1} + u'_x k_z Al^{-1} = 0. \tag{2.36b}$$

The solution for the velocity-field perturbation is

$$u_x = 1 + C_1\sqrt{ReRm^{-1}}\exp\left(zH_a\right) + C_2\sqrt{ReRm^{-1}}\exp\left(-zH_a\right), \tag{2.37}$$

with $H_a = \sqrt{ReRm}Al^{-1}$ the Hartmann number. Imposing the no-slip condition, $\boldsymbol{u}|_{z=D} = \boldsymbol{u}|_{z=-D} = \mathbf{0}$, we obtain

$$u_x = 1 - \frac{\cosh zH_a}{\cosh DH_a}. \tag{2.38}$$

This flow is shown in figure 2.4a (dashed blue). In the framework of our approach, we have checked that standard solutions on flat boundaries are easily retrieved, such as the Ekman, Hartmann, and Stokes boundary layer flows (equations of these flows are described in the Appendix A.1). The coloured lines illustrate in figure 2.4a these classical flows. We verified that our calculations agree perfectly with the theory.

Besides the simplest boundary layers, as an illustrative case, we consider a rotating and magnetised viscous fluid oscillating along $\mathbf{1}_x$ between two no-slip planes. This flow requires the integration of a polynomial of order 10, which prevents any explicit analytical expression of roots in the

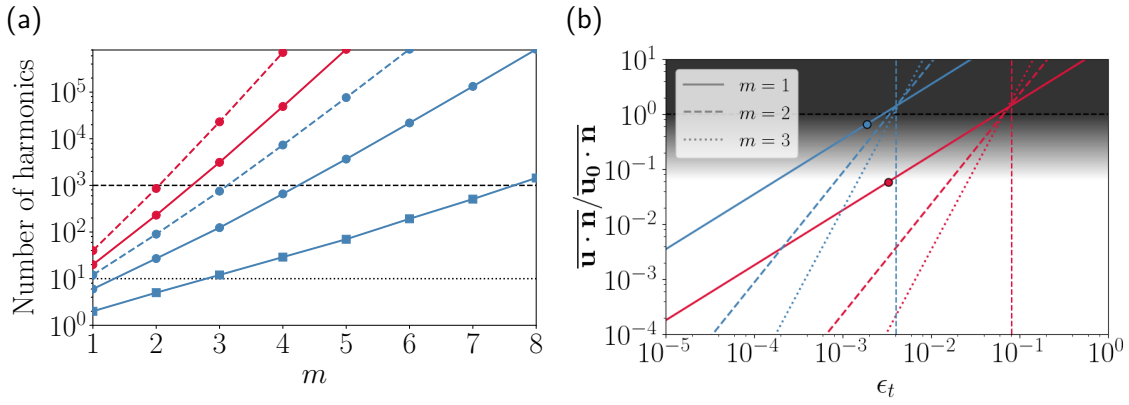

Figure 2.5: **(a)** Number of harmonics vs order m (at $n = 0$, see equation 2.22), for a steady basic flow $\boldsymbol{u}_0 = \mathbf{1}_x$ and an inviscid semi-infinite fluid (blue) or a viscous fluid between two boundaries (red). The topography is either a ridge ($h = \cos(k_x x)$, solid lines) or 3D ($h = \cos(k_x x)\cos(k_y y)$, dashed). The basic magnetic field is either zero (squares) or not (circles, $\boldsymbol{b}_0 = \mathbf{1}_z$). Horizontal lines: typical values for previous works (Buffett, 2010; Glane & Buffett, 2018; Jault, 2020) based on linear perturbations (dotted) and for one-day computations using our code on a laptop (dashed). **(b)** The normalised mean residual for boundary condition $\boldsymbol{u}\cdot\boldsymbol{n} = 0$ versus ϵ_t for three different orders of topography perturbation m (at $n = 0$). Circles: typical cases of Glane & Buffett (2018) with $N = 20\Omega$ (blue) and $N = \Omega$ (red). Vertical dashed lines: smallest length scale at $m = 1$. Grey shading: high residual or divergent series. Parameters: see table 2.2.

general case. In figure 2.4a and 2.4b, we show the solution of this flow, which is 2-dimensional[7] due to rotation (see figure 2.4b). This solution also includes weak nonlinear effects of order 2 (which would be the dominant leading-order effect in the Blasius boundary layers).

2.4.5 Beyond the linear order

Higher-order solutions are desired for their better accuracy, possibly allowing larger topography heights, but also because they can quantify the validity limits of lower-order solutions. However, the associated numerical cost can quickly become prohibitive. Figure 2.5a shows that the number of harmonics involved in the calculation grows exponentially with the orders. Moreover, this figure also shows that the number of harmonics can already be quite large at the lowest order $m = 1$ for the height of the topography. Having optimised our implementation, our code is typically capable of calculating order 3 hydromagnetic solutions with 3D topographies (requiring ~ 1000 harmonics). We can now use these higher-order solutions to quantify convergence with the order. For example, looking at the residual error on the non-penetration boundary condition, figure 2.5b shows that our perturbation-based method only converges below a certain value ϵ_t^c of ϵ_t, and ϵ_t^c being nearly independent of m. But the error can already be quite large for $\epsilon < \epsilon_t^c$, the case $N = 20\Omega$ of Glane &

[7]There is no vertical component, as would be expected from Ekman pumping. This is because there is no pumping for incompressible base flows without horizontal variations (with $\boldsymbol{\nabla}\cdot\boldsymbol{u} = \partial_z u_z = 0$, the no-slip condition yields $u_z = 0$). In our case, the pumping appears only because of the topography.

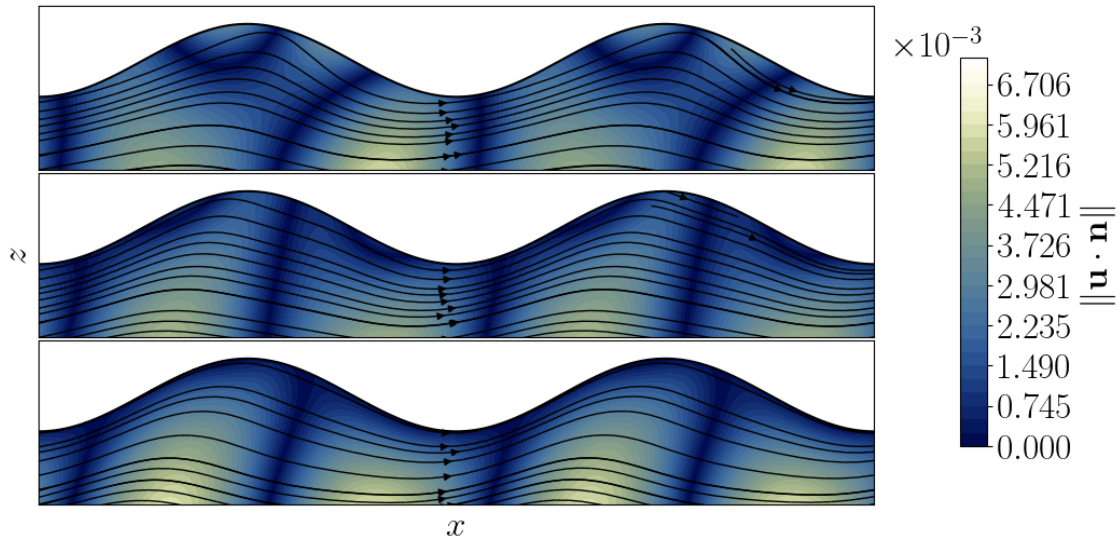

Figure 2.6: Flow streamlines and $\|\boldsymbol{u}\cdot\boldsymbol{n}\|$ (with an artificial n defined in the whole volume) field at order 1,2 and 4 (top to bottom). Parameters: $Al = 0.022$, $Rm = 12.5$, $Ro = Fr = 1.37\times10^{-5}$, $Re^{-1} = 0$, $\chi = \theta = 0$, $\epsilon_t = 6\times10^{-3}$ with an insulating solid ($\tilde{\eta}^{-1} = 0$) with 2D topography models $z = \epsilon_t\cos(x)$, $\boldsymbol{u}_0 = \mathbf{1}_x$ and $\boldsymbol{b}_0 = \mathbf{1}_z$.

Buffett (2018) requires an order $m = 3$ to reduce the error around 10%. These convergence issues are related to the smallest length scale of the problem (vertical dashed lines), either originating from the geometry or from the values of $k_z^{(j,k)}$. In the case considered in figure 2.5b, this limit is related to stratification through $\max(k_z^{(j,k)})$, which is proportional to Fr^{-1} for strong stratification (Jault, 2020). When $\epsilon < \epsilon_t^c$, figure 2.5b also confirms that higher orders allow the use of higher topographies for the same accuracy (*e.g.* one order of magnitude larger between orders $m = 1$ and $m = 3$). As allowed by our approach, considering such larger topography heights may be important to account for geophysical observations (Jault, 2020). As an explicit illustration of the accuracy gain provided by higher orders, figure 2.6 compares the flow at order 1, 2 and 4 for a typical hydromagnetic calculation. The flow is notably modified near the boundary to ensure better the non-penetration boundary condition.

Summary of the chapter

- In previous studies, CMB stresses were explicitly obtained by exploiting several assumptions (Table 2.7). Following a similar approach, the code ToCCo unlocks these limitations by combining numerical and symbolic computations.
- Complex geometries (arbitrary topography, two boundaries) can now be tackled, which will turn out to be crucial (*e.g.* compared to the ridge geometry). The large number of terms imposes the use of symbolic computational algorithms.
- Previous limitations on the accessible ranges of parameters (*e.g.* Glane, 2021) have been released by using arbitrary precision calculations.
- We have implemented the non-traditional β-plane devised by Dellar (2011) to improve the modelling of β effects for thick layers.
- Going beyond previous first-order solutions, our higher-order results increase the accuracy or the acceptable topography height. They also allow for quantification of the validity regime of lower-order solutions.

	Braginsky (1998)	Buffett (2010)	Glane & Buffett (2018)	Jault (2020)	This work
Lorentz force	✓	×	✓	✓	✓
Advection	×	×	✓	✓	✓
3D bumps	×	✓	×	$\times^{(a)}$	✓
β-plane	$\checkmark^{(b)}$	×	×	$\checkmark^{(b)}$	✓
Any tilt of $\boldsymbol{B}$ and $\boldsymbol{\Omega}$	×	×	×	$\checkmark^{(c)}$	✓
Weakly non-linear	×	×	×	×	✓
Two boundaries	$\checkmark^{(d)}$	×	×	×	✓
Non-uniform U, B, ρ	×	×	×	×	✓
Asymptotic limits	$Rm \ll Al^2 Ro^{-1}$			$Fr \ll 1$, $Ro \ll 1$ $Rm \ll Al^2 Fr^{-2}$	

(a) Preliminary results (see Appendix C of Jault (2020))
(b) $\boldsymbol{\Omega}$ is present only via its vertical component
(c) Only 2 orientations of $\boldsymbol{B}$ (vertical and horizontal)
(d) Flat second boundary; our code can consider one or two (possibly bumpy) boundaries

Table 2.7: Summary of the approximations used in previous studies

3 Steady flows - Length of the Day

Contents

Although simple, the limit of steady flows is relevant in many cases, as soon as their temporal variations are much longer than those induced by topography (*e.g.* $\omega \ll \|u_0\| k_z$). For example, length-of-the-day (LOD) variations over periods, 5 to 100 years are caused by fluctuating flows in the Earth's core. For geophysically relevant parameters, we can thus consider steady flows to model this problem.

In this chapter, we focus on steady flows over topography. We will characterise the boundary stress and investigate its variation with parameters. In particular, we will highlight the differences between the hydrodynamic and MHD calculations. Also, the importance of rotation and β plane effects. By considering the ideal MHD limit, we will also investigate diffusionless topographic wave drag and dissipative stress. The interaction between the imposed velocity field and the topography generates waves. We will study the properties of these waves as a function of the dimensionless numbers of the problem. The parameter space is then divided into different regions where a particular type of wave is responsible for most of the forces on the boundary. We will follow by adding a second solid boundary and study the effect of two very close surfaces. Finally, we consider geophysical cases, comparing our model with previous approaches. We investigate the stress on the solid as a function of the wavelength and estimate the total stress on the Earth's mantle from a typical spectrum of the core-mantle topography.

3.1 Characterisation of the stress

Due to the efficiency of our numerical model, we can systematically survey hydromagnetic topographic stresses for different topography shapes and wavelengths. We choose to investigate the rotation and magnetic field effects by calculating the average stress $\langle F_x \rangle$ as a function of Ro and the interaction parameter[1] Rm/Al^2 (figure 3.1), keeping the Lehnert number $Le = Ro/Al$ constant ($\tilde{k}$, Ω_0, $\tilde{B}$, and ρ_r constant in the figures)[2]. We exhibit various regimes and sharp transitions between these regimes. Considering the Earth's core radius $R = 3486$ km and the topography wavelengths $\tilde{k}^{-1} = 5$ km, we first show (top figures) the stress for a ridge topography, with $\chi = 0$ (f-plane, figure 3.1a) and with traditional β-plane effects (figure 3.1b). Then we investigate 3D topography (bottom figures), with traditional or non-traditional β-plane approximations (respectively, figures 3.1c and 3.1d). In these figures, typical values for the Earth's core and oceans (see Table 2.2) are also indicated to illustrate the strong influence of the magnetic field on the stress (even with insulating boundaries). For oceanic application ($R = 6371$ km), the topography wavelength is $\tilde{k}^{-1} = 9$ km, since χ is fixed.

Conducting solid and steady flow

At order $m = 0$ in topography, the non-zero conductivity of the solid generates a linear magnetic field perturbation in z. This is in contrast to our boundary condition of vanishing fields at infinity. This arises from our unbounded solid domain and is thus not physically relevant. Therefore, we will not discuss the conductivity of the solid in this section. For oscillating flows (section 4) the time dependency limits the spatial extent of the perturbation, which has an exponential solution. The effect of the solid conductivity can then be studied in a relevant regime.

The stress on the boundary is due to dissipative processes, but also to radiated waves, which exist for specific ranges of control parameters. Figures 3.1 show sharp changes in stress as a function of Ro and Rm/Al^2. We delineate regions in the parameter space, each corresponding to the propagation of different kinds of MHD waves. We have identified the waves that contribute the most to total stress (see Section 3.2, A.3 and A.2[3] of figure 3.1 and Appendix A.2 give the expression of dispersion relation of classical MHD waves) and reported their names in figure 3.1. The parameter space is divided into two, on either side of $Rm/Al^2 = 1$ (black dashed line). We characterise these regions by considering the asymptotic limits $Rm/Al^2 \gg 1$ (negligible diffusion in the induction equation, *i.e.* ideal MHD) and $Rm/Al^2 \ll 1$ (negligible role of the magnetic field *i.e.* hydrodynamic case). This helps us to find the limits of the major regions using the dispersion relation of waves (see section 3.2). In the hydrodynamic limit, the limit[4] of propagation of inertial-gravity

[1] Interaction parameter or Stuart number is defined as the ratio of electromagnetic to inertial forces, it gives an estimate of the importance of the magnetic field on the flow.

[2] Horizontal axis is $\propto Rm^2 \propto Al \propto Ro$.

[3] Section 3.2 detail the properties of waves present in figure 3.1, Appendix A.3 gives the derivation of line's equations.

[4] Originating from the bounded range for the frequency of (free) inertial waves.

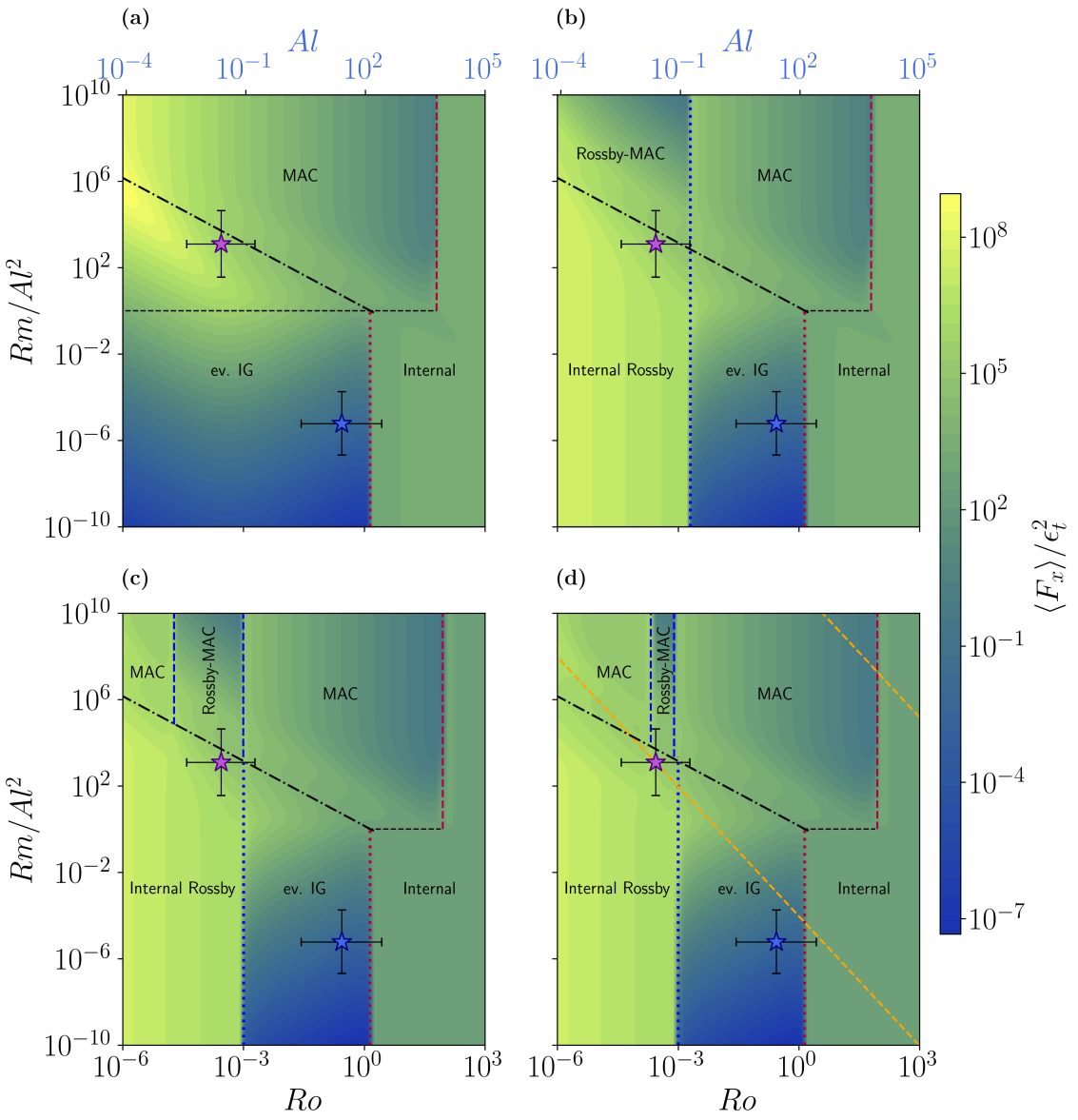

Figure 3.1: Normalised stress (colours) as a function of interaction parameter Rm/Al^2 and Ro at $\theta = \pi/4$ for (top) a ridge $h = \epsilon_t \cos x$, or 3D topography (bottom). Figure **(a)** is with $\mathbf{\Omega} = \cos\theta \mathbf{1}_z$ (f-plane) and $\boldsymbol{b}_0 = -\cos\theta \mathbf{1}_z$. In figures **(b,c)** $\mathbf{\Omega} = (\cos\theta + \chi \sin\theta)\mathbf{1}_z$, and **(d)** is with a non-traditional β-plane approximation. Figures **(b, c, d)** have a magnetic field $\boldsymbol{b}_0 = \sin(\theta)/2\mathbf{1}_y - \cos\theta \mathbf{1}_z$ (equation 2.8). The stress is estimated with $\chi = 0.0014$, *i.e.* $\tilde{k}^{-1} = 5$ km for the core and $\tilde{k}^{-1} = 9$ km for the ocean. The stars represent the Earth's core (purple) and the ocean (blue). The bounds for the internal waves are the red dotted line (equation 3.1) and the dashed line (equation 3.2). The limits for Rossby waves are the blue dotted line (equation 3.5) and the dashed blue ones (equation 3.6). The dashed-dotted black line is $\Lambda = 1$. The orange dashed lines are $Rm = 10^{15}$ and $Rm = 0.625$, for which figures 3.7a and 3.7b, respectively, have been obtained. Within each zone, the type of wave that contributes the most to the total stress is written. Parameters: $\tilde{\eta}^{-1} = 0$, $\boldsymbol{u}_0 = \mathbf{1}_x$, $Le = 0.0122$ (see Table 2.2 for other parameters at the corresponding wavelengths).

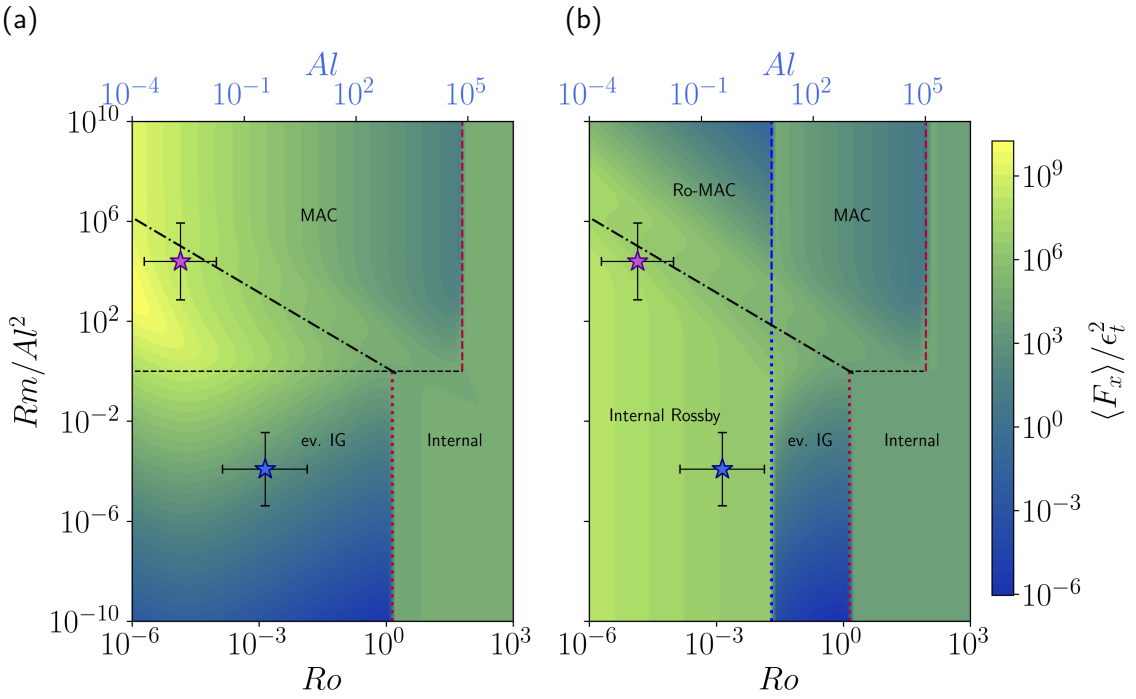

Figure 3.2: Normalised stress (colours) as a function of interaction parameter Rm/Al^2 and Ro at $\theta = \pi/4$ for (left) a ridge topography $h = \epsilon_t \cos x$, $\boldsymbol{b}_0 = -\cos\theta \mathbf{1}_z$ and $\boldsymbol{\Omega} = \cos\theta \mathbf{1}_z$ (f-plane), and (right) a 3D topography $h = \epsilon_t \cos x \cos y$, $\boldsymbol{b}_0 = \sin(\theta)/2\mathbf{1}_y - \cos\theta \mathbf{1}_z$ and non-traditional β-plane (equation 2.8). The stress is shown for $\chi = 0.0287$, that is, $\tilde{k}^{-1} = 100$ km for the core and $\tilde{k}^{-1} = 183$ km for the ocean. The stars represent the Earth's core (purple) and the ocean (blue). The lines are the same as the ones in figure 3.1. Parameters: $\tilde{\eta}^{-1} = 0$, $Le = 6 \times 10^{-4}$, $\boldsymbol{u}_0 = \mathbf{1}_x$ (see Table 2.2 for others parameters at corresponding wavelengths).

waves (red dotted line) can be written for f-plane approximation as

$$Ro > 2\cos\theta \tag{3.1}$$

in our limit $Fr \ll 1$. We find significant stress in the presence of internal waves that are almost independent of Ro. The stress in this zone can be reduced to the simple expression of the inertial gravity wave drag. In the opposite case $Ro < 2\cos\theta$, the waves are evanescent ($\Im(k_z) \gg \Re(k_z)$) and the stress is then negligible.

In the MHD case $Rm/Al^2 \gg 1$, the vertical dashed red line,

$$Al = 2k_H Fr^{-1} \cos\theta, \tag{3.2}$$

corresponds to the transition between MAC (Magneto-Archimede-Coriolis) waves on the left and internal waves, for $Fr \ll 1$ and $Ro \gg 1$. This gives the transition from Alfvén waves to internal waves. For $Ro \ll 1$, magnetic effects are important for the stress when the Elsasser number $\Lambda = RoRmAl^{-2}\cos\theta$, which compares the magnetic and Coriolis forces, is larger than 1 (dashed-dotted line). In this domain, the stress increases as Al^{-1}, a measure of the magnetic field strength.

A new family of waves, the Rossby waves, arises in the β-plane model (compare 3.1b to 3.1a). In the hydrodynamic case, internal Rossby waves only exist between two values of Ro, or below a

certain value of Fr, that are all given by the roots of

$$(k_H^2 - A^2 Fr^2) Ro^2 + 2\sin\theta (BFr^2 - 1)\chi Ro + CFr^2\chi^2 = 0, \tag{3.3}$$

where A, B and C, given in the appendix A.3.3, are only function of θ. The bound in Fr is then

$$Fr^2 < \frac{(Rok_H)^2 - 2\chi Ro\sin\theta}{(RoA)^2 - 2\chi RoB\sin\theta - \chi^2 C}, \tag{3.4}$$

which reduces to $Fr < k_H A^{-1}$ for $\chi \ll 1$, and further simplifies into $Fr < 1$ for ridge geometries ($k_H = 1$, $k_y = 0$). The two bounds in Ro can also be obtained exactly, giving

$$8\chi Fr^2 \cos\theta\cot\theta < Ro < 2\chi k_H^{-2}\sin\theta \tag{3.5}$$

for $Fr \ll 1$. The lower bound, related to the χ^2 term $CFr^2\chi^2$ in Equation 3.3, does not exist when considering Equation 2.7, and requires the more sophisticated approximation (2.8). This transition occurs at $Ro \approx 10^{-10}$ in the figure 3.1d, and is thus not visible.

This hydrodynamic regime now extends to $\Lambda = 1$. In this domain, the stress increases directly with $Ro^{-1/2}$ and is independent of the magnetic field. A domain of evanescent inertial-gravity waves remains between the regions where Rossby and internal waves propagate. For $\Lambda > 1$, the Rossby waves are significantly modified by the magnetic field, hence named Rossby-MAC, yielding weaker stress than in the f-plane case.

In the case of 3D topography, these Rossby-MAC waves only exist in a finite range of Ro (figures 3.1c and 3.1d). This extent of this domain is significantly shrunk for $\mathbf{\Omega}$ given by equation 2.8 (compare figure 3.1c calculated with equation 2.6 for $\mathbf{\Omega}$ and figure 3.1d). This domain is bounded by

$$k_H^2 Ro = \chi\sin\theta\left[1 \pm \sqrt{1 - (Frk_H)^2[\varpi_1(k_y/\chi)^2 + \varpi_2\cot^2\theta]}\right], \tag{3.6}$$

for $Fr, Ro \ll 1$, where (ϖ_1, ϖ_2) are $(1, 0)$, $(9, 0)$ and $(9, 16)$ when considering the three Coriolis force approximations given by Equations 2.6, 2.7, and 2.8, respectively.

The derivation of these limits is detailed in Appendix A.3 and are found imposing a zero determinant for the dynamical equations, using the calculated k_z values. Equation 3.6 illustrates the importance of 3D topographies ($k_y \neq 0$) and density stratification ($Fr \neq 0$) when considering $\chi \neq 0$.

We have also investigated in figure 3.2 a larger topography wavelength $\tilde{k}^{-1} = 100$ km for the core ($\chi = 0.0287$, leading to $\tilde{k}^{-1} = 183$ km for the ocean). Figures 3.2a and 3.2b can be compared, respectively, with figures 3.1a and 3.1d. Our results are mainly unchanged in the simplest case (f-plane, ridge topography). The domain of MAC waves extends to a weaker magnetic field (larger Al) with increasing topography wavelength. For 3D topography and non-traditional β-plane, the domain of Rossby-MAC waves extends to a wider range of Ro, in agreement with equation 3.6.

3.2 Steady topographic waves

To better understand the mechanism at play in establishing stress, we have carried out a more detailed study of the waves arising in figure 3.1d. We show in figure 3.3 the vertical wave numbers

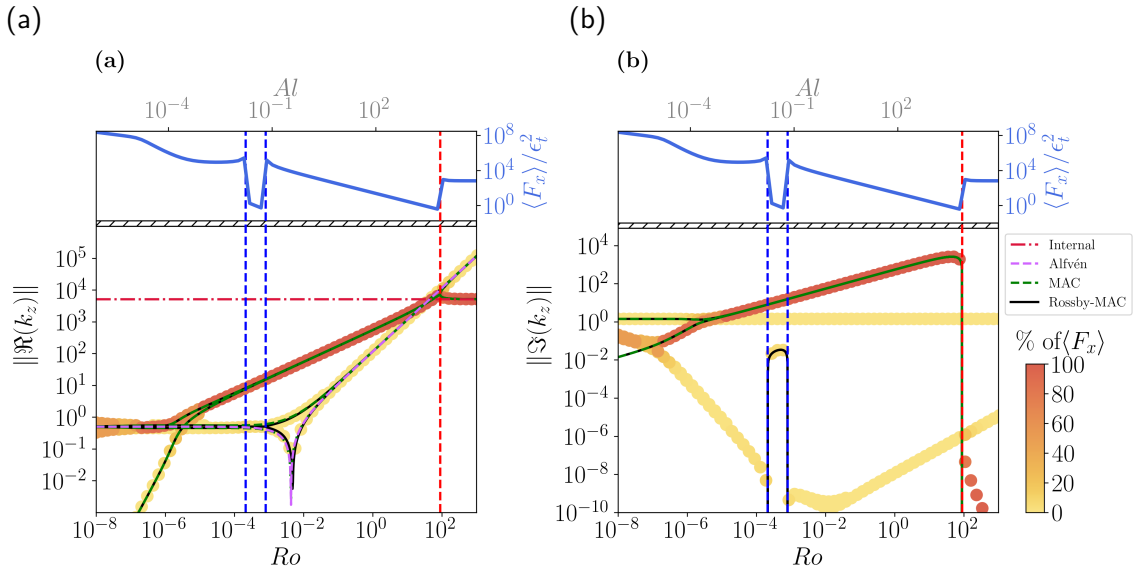

Figure 3.3: Normalised stress (blue solid line at the top of each figure) as a function of Ro and associated absolute value of the real **(a)** or imaginary **(b)** part of the vertical wavenumbers k_z. The results of our code are colour coded (yellow to orange) to show the relative contribution of each k_z to the total stress. Other lines show diffusion-less MHD wave dispersion relations (see appendix A.2 or Salhi *et al.*, 2017). The red vertical dashed line is the equation 3.2, and the blue lines correspond to the equation 3.6. The legend is shared with both figures. Parameters: same as figure 3.1d, with $RmAl^{-2} = 10^{10}$.

k_z as a function of Ro (or equivalently as a function of Al) for a fixed and large interaction parameter ($RmAl^{-2} = 10^{10}$) and a fixed $Le = 0.0122$ (same as in figure 3.1d) and compare them with the solution of the theoretical dispersion relation in the diffusionless limit. We also show the relative contribution of each wave to the total tangential stress. Because curvature effects related to the β-plane are not easily visible in the real part of k_z 3.3a, we show the imaginary part of k_z in figure 3.3b. Our results superimpose almost exactly on the dispersion relation MAC and Rossby-MAC waves. The remaining difference originates from diffusion.

In figure 3.3, the stress is driven mainly by the wave of highest $\Re(k_z)$, except for large Al, as given by equation 3.2. This branch consists of MAC waves since it involves magnetic field, rotation, and stratification. Another branch is well described by the dispersion equation for Alfvén waves (purple dashed curve). It has a small $\Re(k_z)$ and contributes negligibly to total stress. For large Al, the waves with the smallest $\Re(k_z)$ are responsible for most of the stress. Their wavenumbers obey the dispersion relation of the internal waves, and the stress depends only on Fr. Stratification turns out to be key in all stress mechanisms investigated here.

However, this does not explain the sudden drop in the stress that can be seen between the blue dashed lines of equations 3.6. Looking at the imaginary part, we observe the emergence of a domain where Rossby-MAC waves dispersion relation is distinct from MAC waves. In this parameter range, the solution consists of a combination of MAC and Rossby-MAC waves, the MAC waves carry most of the stress but have a negligible amplitude compared to Rossby-MAC waves.

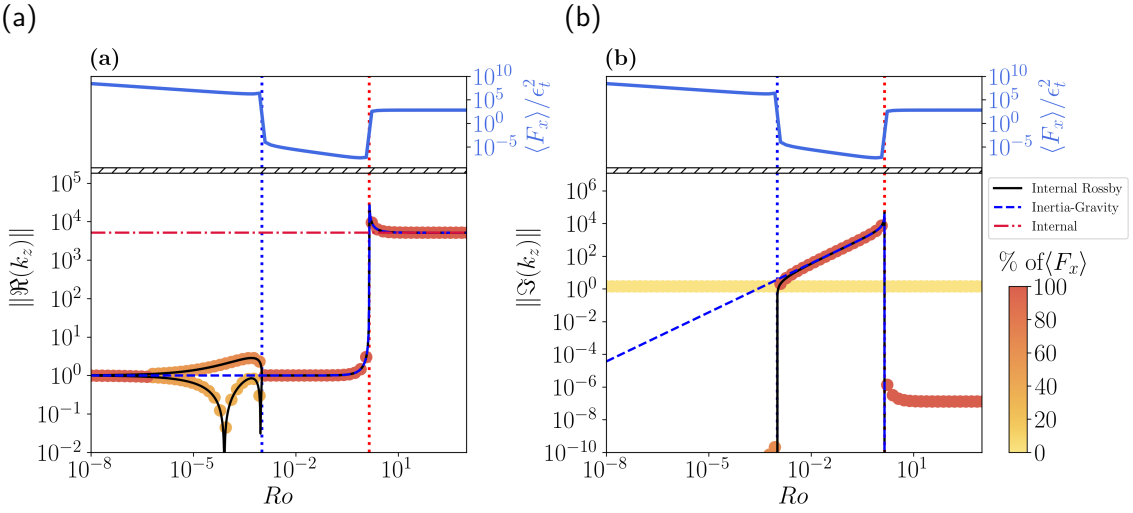

Figure 3.4: Normalised stress (blue solid line at the top of each figure) as a function of Ro and associated absolute value of the real **(a)** or imaginary **(b)** part of the vertical wavenumbers k_z. The results of our code are colour coded (yellow to orange) to show the relative contribution of each k_z to the total stress. They are calculated in the hydrodynamic limit, with a non-traditional β-plane. Other lines show diffusionless MHD wave dispersion relations (see appendix A.2 or Salhi *et al.*, 2017) . The vertical red dashed line is equation 3.1, and the blue line is equation 3.5. Parameters: same as figure 3.1d, with $RmAl^{-2} = 10^{-10}$.

Rossby-MAC waves are indeed very inefficient at driving boundary stresses and are key for this stress drop. By contrast, in the hydrodynamic limit, the Rossby waves at low Ro are very efficient in generating stress (figure 3.1d). We also provide k_z and the relative contribution of each wave in the hydrodynamic limit.

Figure 3.4 shows vertical wavenumbers k_z, as in figure 3.3, in the hydrodynamic limit ($RoAl^{-2} = 10^{-10}$). We see that the equation 3.1 (red dotted line) delimitate the propagation of internal waves on the right side and evanescent Inertial-gravity waves on the left part. We observe that on the left of the line given by equation 3.5 (blue dotted line), the wave numbers correspond to those of the Rossby waves modified by stratification effects (Internal Rossby waves).

Finally, we focus on the large stress values that are obtained at the limits of Rossby and Rossby-MAC wave domains (equations 3.5-3.6), which are too abrupt to be seen in figure 3.1d. This is illustrated in figure 3.5a, which shows the normalised stress along the horizontal lines $RmAl^{-2} = 10^{10}$ in the ideal MHD limit (orange) and $RmAl^{-2} = 10^{-10}$ in the hydrodynamic limit (blue). At the frontiers of Rossby wave domains, we observe sharp increases that suggest mode resonances. Calculating the eigenmodes of our problem, we obtain free steady (MAC-) Rossby modes that can be excited by the topography-forced waves, and which corresponds to 3.5-3.6. Looking at the associated wavenumber (figure 3.5b), at resonances, the wavevector is found to be perpendicular to the rotation vector in the hydrodynamic case (green dashed line) and perpendicular to the magnetic field (pink dashed line) in the ideal MHD limit (this helped us to find equation 3.6).

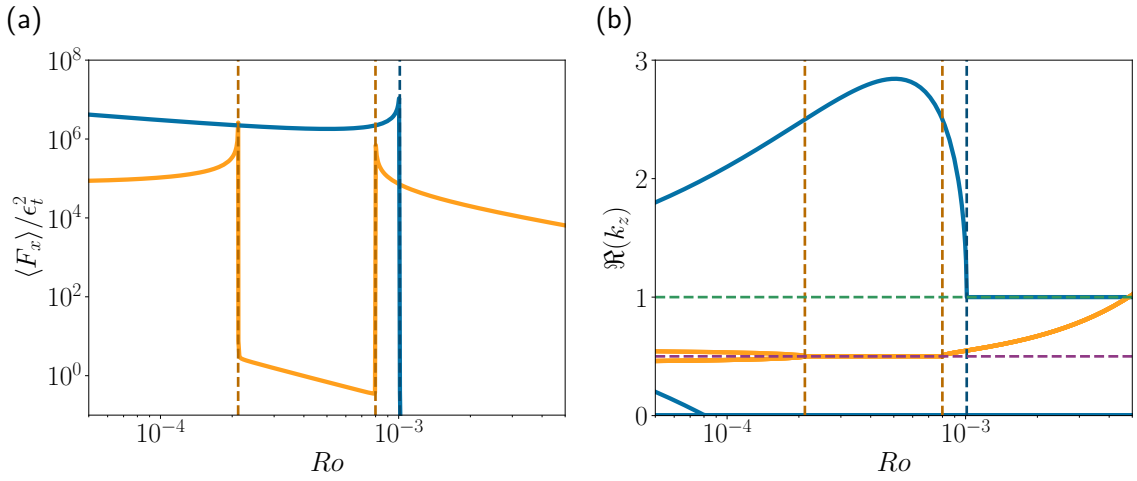

Figure 3.5: **(a)** Normalised stress vs Ro for $RmAl^{-2} = 10^{10}$ (ideal MHD, orange) and $RmAl^{-2} = 10^{-10}$ (hydrodynamic limit, blue), **(b)** Real part of vertical wavenumber vs. Ro. The vertical lines correspond to the theoretical limits for Rossby waves (equation 3.5, dashed blue) and MAC-Rossby waves (equations 3.6, dashed orange). Horizontal lines are $\boldsymbol{k} \cdot \boldsymbol{\Omega} = 0$ (green dashed line) and $\boldsymbol{k} \cdot \boldsymbol{b}_0 = 0$ (purple dashed line). Parameters: same as in figure 3.1d.

3.3 Non-diffusive flows

3.3.1 Inviscid hydrodynamic flows

In this section, we consider flows in the absence of magnetic fields and without any dissipative processes. This is motivated by the interest in bridging the gap between our research and studies conducted in atmospheric and oceanic sciences. Furthermore, opting for this approach is advantageous, as it allows for analytically feasible calculations, leading to explicit results.

For stratified rotating fluids without β-plane effects, inertial-gravity waves are radiated. We can calculate their vertical wave number for a steady flow $\boldsymbol{u}_0 = \mathbf{1}_x$ and f-plane approximation ($\boldsymbol{\Omega} = \cos\theta \mathbf{1}_z$), and obtain

$$k_z^2 = k_H^2 \frac{Fr^{-2} - 1}{1 - Ro_l^{-2}}, \tag{3.7}$$

with the local (scaled) Rossby number $Ro_l = Ro/(2\cos\theta)$. We then have propagating waves only for $Fr < 1 < Ro_l$ or $Ro_l < 1 < Fr$. In this thesis we exclusively focus on the first domain since flows at $Fr > 1$ are considered supercritical and are beyond the scope of our model.

The wave drag associated with inertial-gravity waves in a topography $h = \epsilon_t \cos(k_x x + k_y y)$ is

$$\langle F_x \rangle / \epsilon_t^2 = \left| \mathrm{Re}\ \frac{k_x}{2k_H} \sqrt{\left(Fr^{-2} - 1\right)\left(1 - Ro_l^{-2}\right)} \right|. \tag{3.9}$$

This equation give the stress for one ridge but can be summed (in the first linear approximation) to obtain the stress of a more complex topography. For an arbitrary (steady) topography

Perfect fluid and stress: radiation condition

In the limit case of non-dissipative fluid (inviscid, ideal MHD) the waves that emerge from topography do not vanish at infinity as we would like to meet our boundary condition. In such a case, which is often considered for ocean and atmosphere flows, we need to use the condition referred to as the radiation condition.
Solving the equations, we obtain a solution of the form

$$\boldsymbol{X} = \boldsymbol{A}\cos(x + k_z z) + \boldsymbol{B}\cos(x - k_z z) + \boldsymbol{C}\sin(x + k_z z) + \boldsymbol{D}\sin(x - k_z z) \tag{3.8}$$

given for ridge topography and one positive k_z for simplicity. $\boldsymbol{A}, \boldsymbol{B}, \boldsymbol{C}$ and $\boldsymbol{D}$ are positive. A positive vertical wave number (indicated by the + sign in front of kz_z) corresponds to an upward energy flux towards the boundary. This non-physical behaviour is prevented by the radiation condition, which imposes that every Fourier component needs to propagate toward infinity (for historical paper see Sommerfeld (1912) and for internal waves application see Bell (1975)). This gives $\boldsymbol{A} = \boldsymbol{C} = \boldsymbol{0}$. We then evaluate$\boldsymbol{B}$ and $\boldsymbol{D}$ thanks to the non-penetration boundary condition.
Note that for inertial-gravity wave drag (equation 3.9) coefficients A, B, C, D are of opposite sign on each side of the wave propagation domains ($Fr < 1 < Ro_l$ and $Ro_l < 1 < Fr$). This leads to eliminating different Fourier coefficients for each case, which results in the absolute value of equation 3.9.

$h = \epsilon_t \sum_j A^{(j)} \exp(\boldsymbol{k}_H^{(j)} \cdot \boldsymbol{r})$ (equation 2.1), we have

$$\langle F_x \rangle / \epsilon_t^2 = \sum_j \left| \mathrm{Re}\, \frac{k_x^{(j)}}{k_H^{(j)}} A^{(j)^2} \sqrt{\left(Fr^{-2} - 1\right)\left(1 - Ro_l^{-2}\right)} \right|. \tag{3.10}$$

For instance, the stress on an egg box topography $h = \epsilon_t \cos x \cos y$ is $2^{3/2}$ times lower than on a simple $h = \epsilon_t \cos x$ ridge. Equation 3.10 is formally similar to equation 20 of Legg (2021), see also Bell Jr. (1975) and Nikurashin & Ferrari (2010*b*). The limit $Ro_l^{-1} = 0$ corresponds to the gravity wave drag (*e.g.* Athanassiadou, 2003). This theoretical wave drag is important for estimating the stress in laboratory experiments with fast rotation and no magnetic field.

In section 3.1 we have seen that Rossby waves play a major role in the drag. Adding β-plane effects, we obtain a vertical wave number,

$$k_z^2 = \frac{(Fr^{-2} - 1)(Ro^2 k_H^2 - 2Ro\chi \sin\theta)}{Ro^2 - 2Ro\chi \sin\theta - 4\cos^2\theta}. \tag{3.11}$$

This equation corresponds to the thermal Rossby waves of figure 3.4. We see that waves propagate when $Fr > 1$ and $2\chi \sin\theta / k_H^2 < Ro < \sqrt{\chi^2 \sin^2(\theta) + 4\cos^2(\theta)} + \chi \sin(\theta)$, or if $Fr < 1$ and $Ro < 2\chi \sin\theta / k_H^2$ (equation 3.5) or $Ro > \sqrt{\chi^2 \sin^2(\theta) + 4\cos^2(\theta)} + \chi \sin(\theta)$. This corresponds to the "spectral gap" of (section 12.7 Gill, 1982). Calculating the associated horizontal stress, we

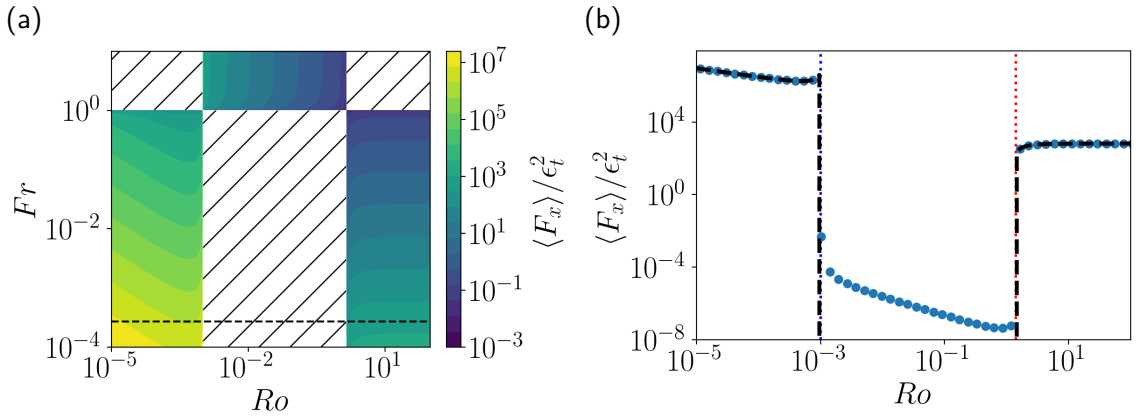

Figure 3.6: Horizontal stress calculated from equation 3.12. **(a)** Stress as a function of Ro and Fr. The black dotted line is the bottom of figure 3.1c and the dashed line of figure 3.6b. Hatches correspond to the absence of stress. **(b)** Theoretical stress (dashed black) as a function of Ro. We compare with results of figure 3.1d at $Rm/Al^2 = 10^{-10}$ (blue dots). The blue and red dotted lines are, respectively, equations 3.5 and 3.1. The parameters are those of figure 3.1c.

obtain

$$\langle F_x\rangle/\epsilon_t^2 = \sum_j \left| \mathrm{Re}\, k_x^{(j)} A^{(j)^2} \sqrt{\frac{\left(Fr^{-2}-1\right)\left(Ro^2 - 2Ro\chi\sin(\theta) - 4\cos^2\theta\right)}{Ro^2 k_H^{(j)^2} - 2Ro\chi\sin(\theta)}} \right|. \tag{3.12}$$

We observe non-zero stress when waves propagate, as can be seen in figure 3.6. The stress values at low interaction parameters in figure 3.1 (dotted line of figure 3.6a and blue dots of figure 3.6b) are well approximated by this formula (except for non-traditional β effects that are negligible in this case).

3.3.2 Ideal MHD

In real MHD flows the Ohmic dissipation arising from the dissipative term $Rm^{-1}\nabla^2\boldsymbol{u}$ in the induction equation plays an important role for the flows and the stress on the boundary. To disentangle the effects originating from non-dissipative wave generation and Ohmic dissipation, we aim to compare our calculation at moderate Rm with the limit case of the ideal MHD, which corresponds to the limit $Rm \gg 1$, making the dissipation term negligible. This limit corresponds to a perfectly conducting fluid when magnetic and kinetic energy can convert without loss. This has also the effect of "freezing" the fluid in the magnetic field lines, forcing the field lines and the fluid to move together. This effect is referred to as the frozen-flux theorem.

We compare in figures 3.7 the stress for almost ideal MHD (figures 3.7a and 3.7c) of weak diffusion[5] ($Rm = 10^{15}$) and for moderate $Rm = 0.625$ (figures 3.7b and 3.7d), which is a resistive

[5]The diffusion cannot be zero otherwise the stress would be exactly zero since our code cannot handle radiation boundary condition necessary in absence of diffusion.

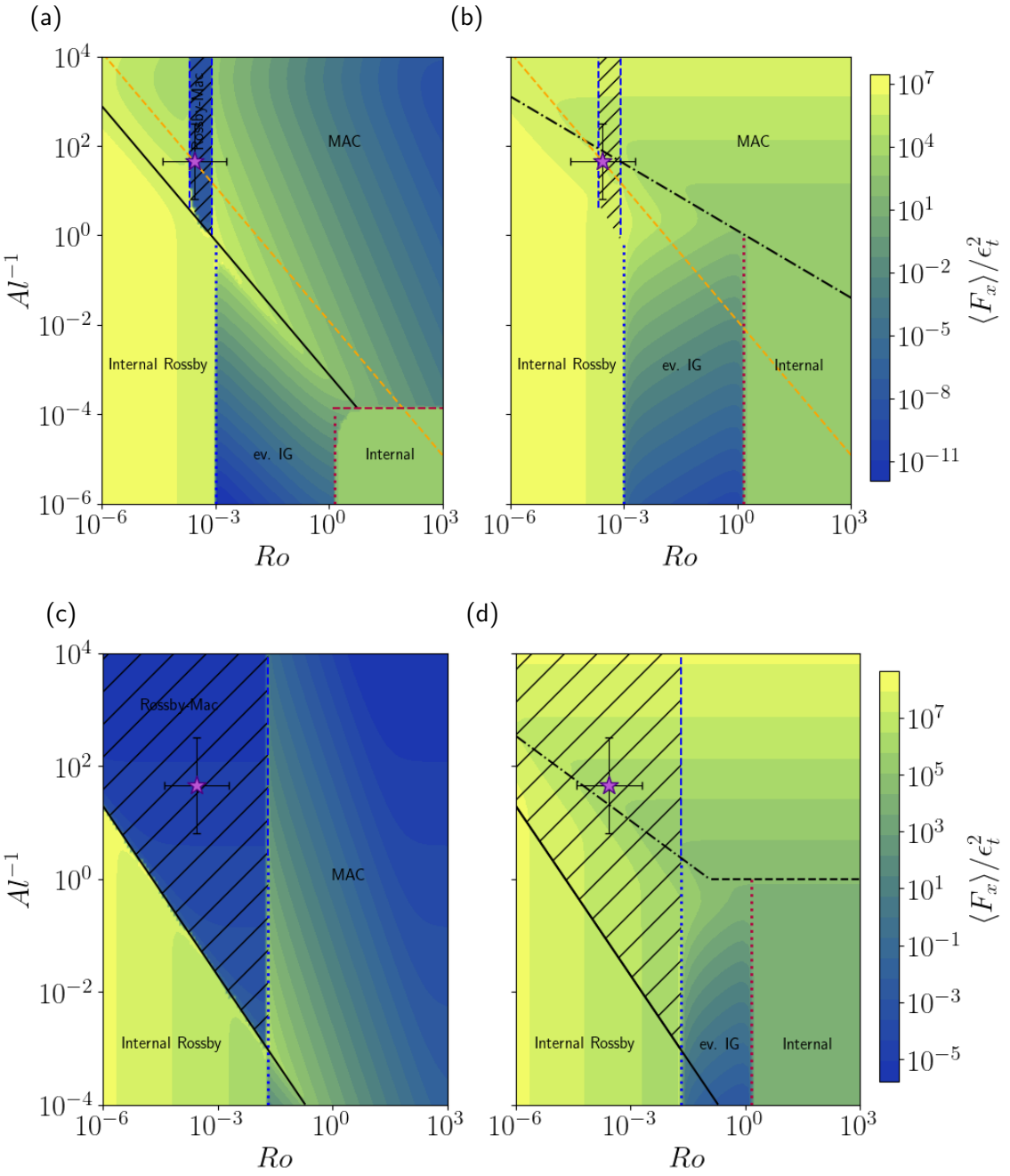

Figure 3.7: Normalised stress as a function of Al and Ro ($\theta = \pi/4$, $\tilde{\eta}^{-1} = 0$). The basic velocity is $\boldsymbol{u}_0 = \mathbf{1}_x$ and $\boldsymbol{b}_0 = \sin(\theta)/2\mathbf{1}_y - \cos\theta\mathbf{1}_z$, with a non-traditional β-plane, the other parameters are those of table 2.2 for $\tilde{k}^{-1} = 5$ km (top) and $\tilde{k}^{-1} = 100$ km (bottom). (left panel) ideal MHD approximation, $Rm = 10^{15}$, black solid line is $Le = 7.5 \times 10^{-4}$, delimiting the hydrodynamic and MHD zones. (right panel) Diffusive case, $Rm = 0.625$, dashed-dotted line is $\Lambda = 1$. The hatches correspond to the region where the stress is proportional to the dissipation ($\propto Rm^{-1}$). The black dashed line shows the Lehnert number of table 2.2, for which figures 3.1 and 3.2 have been calculated. Vertical lines and symbols as in figures 3.1 and 3.2.

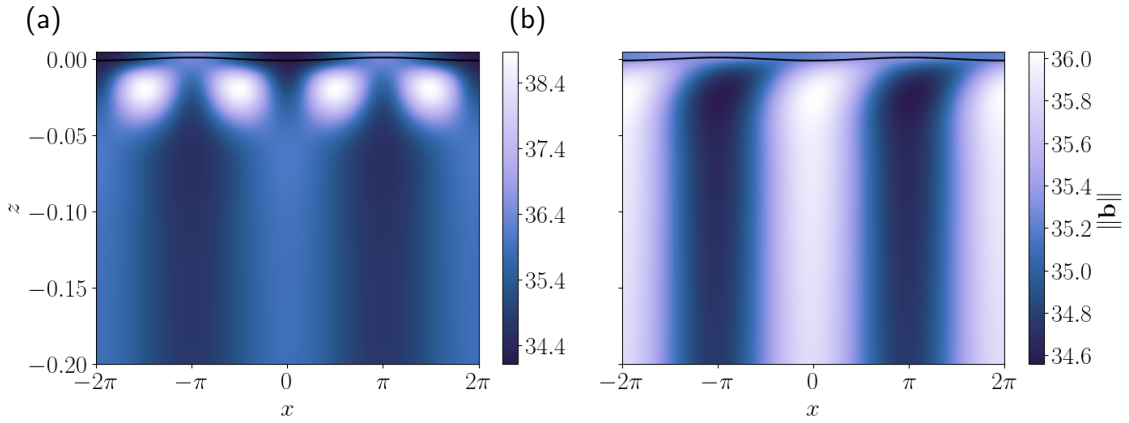

Figure 3.8: Magnetic field norm $\|\boldsymbol{b}\|$, **(a)** for $Rm = 10^{20}$ (ideal MHD) and **(b)** $Rm = 12.5$ (Earth's core). Parameters: $\epsilon_t = 10^{-3}$, others are those of table 2.2 for $\tilde{k_x}^{-1} = 100$ km.

MHD model. Figure 3.7 corresponds to the parameters of table 2.2 for 5 km (top) and 100 km (bottom).

Therefore, we investigate a 2D section of the parameter space (Ro, Al, Rm) that is different from the section explored in figures 3.1 and 3.2. At large Rm (figures 3.7a and 3.7c), the limit between the hydrodynamic and MHD cases corresponds to a constant Lehnert number instead of $\Lambda = 1$ for $Rm = O(1)$ or lower (figures 3.1, 3.2, and 3.7b and 3.7d). In some parts of the space (Ro,Al), the figures for the ideal and resistive MHD are identical, showing that the stress must be attributed only to wave generation. In contrast, we find a parameter range for which the stress varies as Rm^{-1} (hatched zone), showing that it comes mainly from Ohmic dissipation. This corresponds to the range of the Rossby number delimited by the equation 3.6, where the MAC-Rossby waves propagate.

For any wavelength considered here, we observe that at the Earth's core parameters, electrical resistivity plays an important role. At high $Rm \gg 1$ the stress scales directly as Rm^{-1}, while at the parameters of the Earth's core (around $Rm = 12.5$), it scales approximately as $Rm^{-1/4}$.

In figure 3.8 we show the norm of the magnetic field corresponding to Earth's parameters of figures 3.7c and 3.7d, again in the ideal MHD limit (figure 3.8a) and for a resistive MHD model 3.8b). We observe a strong influence on the geometry of the magnetic field. In the ideal MHD shape, the perturbation is localised close to the boundary while it propagates far away in the resistive case, as well as being smaller in amplitude.

3.4 Duct geometry

Braginsky (1998) proposed a model of a stratified layer at the top of the core. He considered a solid second boundary at this transition to mimic a sharp density jump between this layer and the well-mixed convective bulk. Even if this does not model perfectly a two-fluids interface, this avoids the problems that can be encountered in a semi-infinite domain, when the waves propagate further than the fluid layer we want to model, or even over distances about the core radius. In addition,

such a second boundary is relevant for laboratory experiments.

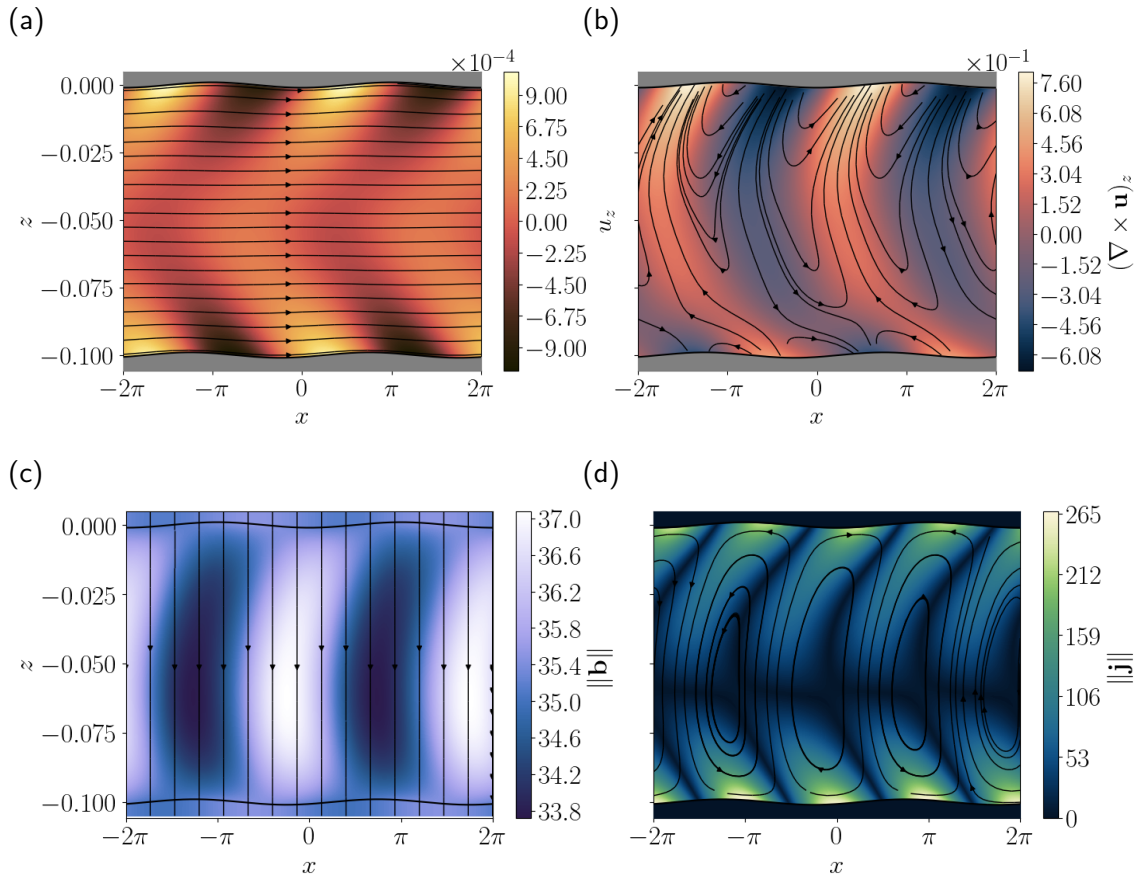

Figure 3.9: Illustrating flow between two boundaries. **(a)** Vertical velocity u_z and velocity streamlines. **(b)** vertical vorticity $(\nabla \times \boldsymbol{u})_z$ and vorticity streamlines. **(c)** Magnetic field amplitude $\|\boldsymbol{b}\|$. **(d)** Electric current density amplitude $\|\boldsymbol{j}\|$. Parameters: $\epsilon_t = 10^{-3}$, top topography $h = -\epsilon_t \cos(x)$, bottom topography $h = -\epsilon_t \cos(x + \pi/4) - 0.1$, $\boldsymbol{u}_0 = \mathbf{1}_x$, $\boldsymbol{b}_0 = \sin(\theta)/2\mathbf{1}_y - \cos\theta \mathbf{1}_z$, with $\theta = \pi/4$. Others are those of table 2.2 for $\tilde{k_x}^{-1} = 100$ km.

Therefore, we have introduced a second solid boundary in our model. The second boundary can also have an arbitrary topography, possibly different from the top boundary. In figure 3.9 we show an illustrating flow between two out-of-phase ridge topography.

The distance between the two boundaries corresponds to 10% of $\tilde{k}^{-1}$ (10 km) for Earth's parameters. We see that perturbations generated by the upper topography, which previously vanished to infinity, now encounter the perturbation coming from below. The interaction of these perturbations creates a different flow that is likely to modify the torque on the boundaries. The magnetic field (figure 3.9c) is also significantly modified. We notably observe that, in this case, the maximum magnetic perturbation is localised at the midpoint between the two boundaries.

To quantify the effects of a second boundary on stress, we show in figure 3.10 the stress as a function of the distance D between the two ridge boundaries. The stress is calculated for a flat second boundary and also for a collection of phase shifts between the two topographies.

As expected, the second boundary does not affect the stress when D is large enough (here for a

fluid layer thicker than 10 km). Conversely, the results are more complex for a thinner fluid layer. Focusing on the limit $D \ll 1$, we can obtain from our calculations a general scaling of the stress

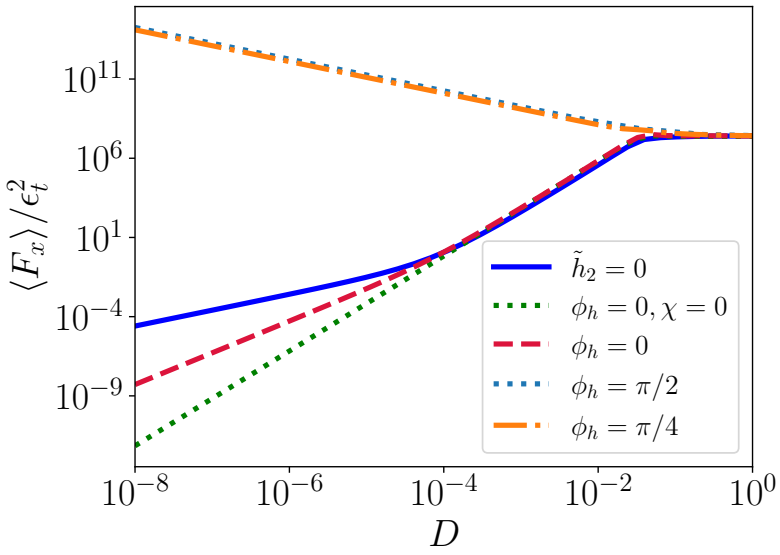

Figure 3.10: Normalised stress as a function of the distance between the two boundaries D, for different bottom boundary shapes. The basic velocity is $\boldsymbol{u}_0 = \mathbf{1}_x$ and $\boldsymbol{b}_0 = \sin(\theta)/2\mathbf{1}_y - \cos\theta\mathbf{1}_z$. The top boundary is $h = \epsilon_t \cos x$, and the bottom boundary is $h_2 = \epsilon_t \tilde{h}_2 \cos(x + \phi_h) - D$. When not specified otherwise, $\tilde{h}_2 = 1$ and $\chi = 0.0286$. $\theta = \pi/4$, $\tilde{\eta}^{-1} = 0$ and other parameters are the ones of Table 2.2 for $\tilde{k}^{-1} = 100$ km.

as a function of D. For $h/\epsilon_t = \cos x$ and $h_2/\epsilon_t = \tilde{h}_2 \cos(x + \phi_h) - D$, we have

$$\langle F_x \rangle / \epsilon_t^2 = f_0 D^{-1} + f_1 D + f_2 D^2 + \mathcal{O}(D^3). \tag{3.13}$$

Taylor expansion coefficients of equation 3.13 scale as $f_0 \propto \tilde{h}_2 \sin(\phi_h)/(\chi - \chi_c)$, $f_1 \propto (1 - \tilde{h}_2)$ and $f_2 \propto \chi_c \chi/(\chi - \chi_c)$, with χ_c the solution of equation 3.5. The stress on the top boundary vanishes when the topographies are in phase, whereas it diverges otherwise (a second flat boundary being seen as in phase).

Interestingly, the coefficients f_0 and f_2 can be positive or negative according to the value of χ. This corresponds to the presence or absence of MAC-Rossby waves. This differs from the semi-infinite case, where the pressure on the fluid side is always opposed to the basic flow. When the two boundaries are in phase ($\phi_h = 0$), axially invariant geostrophic motions are part of the solution. In another context, they have been shown to be ineffective in generating pressure stress (Gerick *et al.*, 2020).

3.5 Geophysical application

3.5.1 Previous approaches

To model the core-mantle coupling related to the length of the day variations, several works have created models using different approaches, assumptions, and approximations (see table 2.7). This

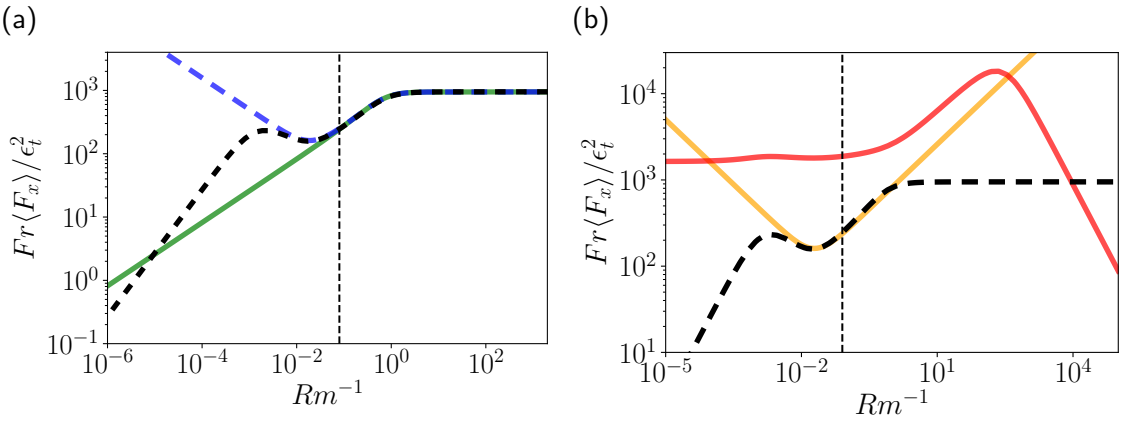

Figure 3.11: Stress as a function of Rm^{-1} (vertical dashed line shows a realistic geophysical value $Rm = 12.5$). **(a)** Comparison of our model with those of Jault (2020) (dashed blue) and Braginsky (1998) (green) which both include β-plane effects. **(b)** Comparison of $\langle F_x \rangle$ calculated with (black dashed) and without ($\chi \equiv 0$, solid red and orange) β terms. The limit $Fr \ll 1$ (orange) recovers the estimate obtained with the β term for Rm^{-1} in $0.01-1$. Parameters: $Ro = 1.37\times10^{-5}$, $Al = 2.24\times10^{-2}$, $\chi = 2.86\times10^{-2}$, $\boldsymbol{u}_0 = \mathbf{1}_x$ $\boldsymbol{b}_0 = \mathbf{1}_z$, $\theta = \pi/4$, $\tilde{\eta}^{-1} = 0$ and $h = \epsilon_t \sin x$.

section aims to compare our code with the results previously obtained.

First, these previous studies helped us validate our code with a variety of benchmarks. For instance, we have reproduced previous theoretical non-magnetic atmospheric (Athanassiadou, 2003) and oceanic (Legg, 2021) results, as well as classical hydromagnetic wave dispersion relations (Finlay, 2008; Salhi *et al.*, 2017). Furthermore, we have successfully validated our topography-driven MHD flows against Jault (2020), Glane & Buffett (2018) and Braginsky (1998) considering the various assumptions summarised in Table 2.7.

We then examined whether our results differed from the previous ones, particularly for the CMB parameters. Figure 3.11a compares our topographic stress results with studies that also use β-plane approximations, (*i.e.* Jault, 2020; Braginsky, 1998). Here, we consider a quite large CMB topography wavelength of $\sim$ 600 km. Because of the assumptions of these two previous works ($Rm^{-1} \gg RoAl^{-2}$ for Braginsky (1998), $Rm^{-1} \gg Al^{-2}Fr^2$ for Jault (2020)), these three models differ in the limit of large Rm but agree for small Rm values, notably at Earth's core parameters (vertical dashed line).

For large topography wavelength, the β-terms are crucial, as illustrated in figure 3.11b (compare dashed black and red curves). In a certain range of Rm, the model built in the limit $Fr \ll 1$ allows one, however, to retrieve the correct boundary stress, even without the β-plane terms (compare orange and dashed black curves).

3.5.2 Scale dependence of the core-mantle topographic stress

We have seen in figure 1.4 that the topography extends over a broad wavelength spectrum. Combining β-plane and 3D topographic effects, we can span a wide range of length scales, from the

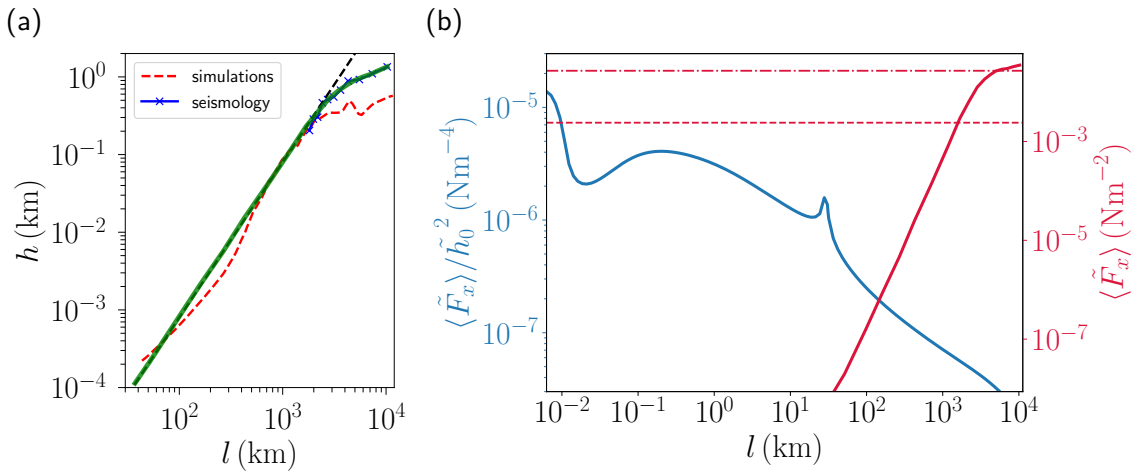

Figure 3.12: **(a)** Model of CMB topography (green) used in figure b. Our fit is superimposed on the values of figure 1.4 relevant for CMB (seismological data and mantle convection output). The black dashed corresponds to the scale l^2. **(b)** Topographic (dimensional) mean stress $\langle \tilde{F}_x \rangle / \tilde{h}_0^2 = \rho_r \tilde{U}^2 \langle F_x \rangle / \tilde{h}_0^2$ normalised by topography $\tilde{h}_0 = \epsilon_t / \tilde{k}_x$ (blue), or for a CMB topography model (red) as a function of topography wavelength $l = 2\pi \tilde{k_x}^{-1} = 2\pi\chi R$ for the Earth's core parameters. The red dashed horizontal line is the nominal stress value (2.4×10^{-3} Nm^{-2}) to explain the variations in LOD (Roberts & Aurnou, 2012), the dashed dotted line is the value of 2.7×10^{-2} Nm^{-2} adopted by Glane & Buffett (2018). Parameters: $h = \epsilon_t \cos x \cos y$, $\rho_r = 10^4$ kg.m^{-3}, $\tilde{U} = 10^{-4}$ m.s^{-1}, $B = 5 \times 10^{-4}$ T, $\eta = 0.8$ m^2.s^{-1}, $R = 3486$ km, $\Omega_0 = N = 7.29 \times 10^{-5}$ rad.s^{-1}, $\theta = \pi/4$, $\tilde{\eta}^{-1} = 0$.

viscous boundary layer thickness to the Earth's core radius. For a given height of the topography, figure 3.12 shows that the topographic mean stress varies in a non-trivial way over several decades. The sharp variation at 30 km corresponds to the transition between the Rossby-MAC and MAC waves given by equation 3.6. The mean normalised stress $\langle \tilde{F}_x \rangle / \tilde{h}_0^2$ maintains the same order of magnitude from 10 m to 50 km and then starts to decrease. This shows that the smallest wavelength (< 10 km) is more efficient in producing stress; however, this does not take into account the topography height which increases the stress quadratically. Therefore, we need to know the amplitude spectrum of the topography.

Our results can be combined with seismological estimates of Earth's core topography from 1.4 to provide the global torque on the core. Figure 3.12b gives the tangential stress for an illustrative but realistic example of core-mantle topography. We show in figure 3.12a the topography spectrum used. It fits the seismological data at large wavelengths available and is extended to smaller wavelengths using results from numerical simulations.

We observe that the larger wavelengths are predominant in the generation of stress. The height of large-scale topography more than compensates for the diminishing stress with increasing wavelength. We can expect these results to be different in other planetary layers, each characterised by distinct topographical shapes. This contrast is exemplified by the surface of Earth and Mars, where the amplitude decreases less rapidly as the wavelength diminishes. In conclusion, we can state that the most important topography components at the CMB are the largest ones (> 100 km). In

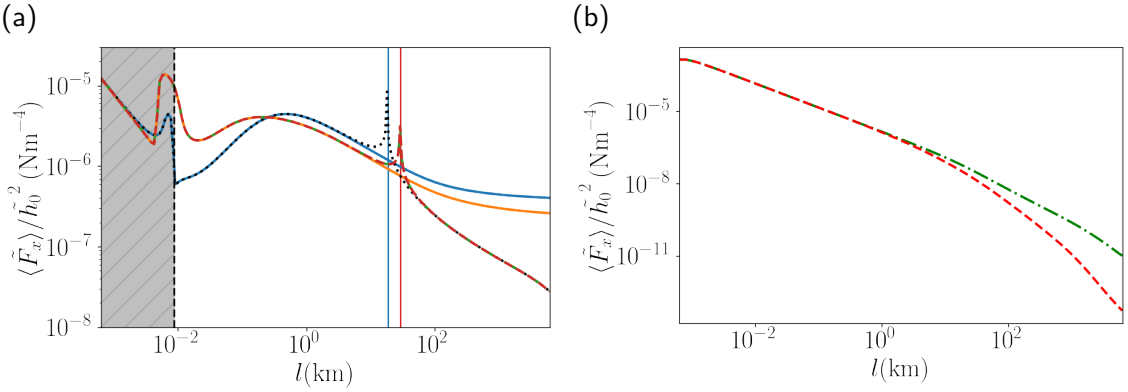

Figure 3.13: Topographic (dimensional) mean stress $\langle \tilde{F}_x \rangle / \tilde{h}_0^2 = \rho_r \tilde{U}^2 \langle F_x \rangle / \tilde{h}_0^2$ normalised by the topography as a function of topography wavelength l, for different approximations of $\mathbf{\Omega}$. **(a)** f-plane (solid blue), traditional β-plane (dotted black), tilted and uniform (solid orange). **(a,b)** tilted with β-effects on z-component (dashed-dotted green) and Dellar (2011) non-traditional β-plane (dashed red). In **(a)** the grey part corresponds to $Fr > 1$, the flow is then supercritical and beyond our framework. The parameters are the same as in figure 3.12 ($\Lambda = 0.341$). The blue and orange vertical lines are equation 3.14 for respectively $\varpi = 1$ and $\varpi = 9$. In **(b)** parameters correspond to a QG flow ($\Lambda = 3.41 \times 10^{-5} \ll 1$), with $B = 5 \times 10^{-5}$ T, $\eta = 8$ m^2.s^{-1}, $\Omega_0 = N = 7.29 \times 10^{-5}$ rad.s^{-1} and $Fr^{-1} = 0$. Other parameters are the same as figure 3.12.

this situation, we can see the importance of accounting properly for the global geometry, notably through the β-plane.

3.5.3 Which β-plane approximation for CMB stress estimation ?

All the previous sections have shown the importance of how the rotation vector is modelled locally for calculating the stress at the CMB. However, there are several approximations for it, which are more or less complex. The question here is to determine the most suitable approach to model the CMB and to establish what degree of precision we want to use. In figure 3.13a we show, in the same way as in figure 3.12b the dimensional normalised stress as a function of the topography wavelength and for Earth's core parameters. Stress is given for five different approximations of the rotation vector $\mathbf{\Omega}$, from the simplest f-plane to the non-traditional β-plane (equation 2.8). As we can see, having a titled rotation vector has a major impact on the stress on the whole spectrum (see differences between black/blue and red/orange/green curves). As expected, the β-effects play a significant role, at large wavelengths, when it is larger than the limit of Rossby waves (resonance), given by the dimensional form of equation 3.6

$$l = \pi \sqrt{2R\tilde{U}\left(\frac{k_H^2}{\Omega \sin\theta} + \frac{\varpi \Omega k_y^2 \sin\theta}{N^2}\right)} \tag{3.14}$$

It can be noted that the range of existence of Rossby waves is bounded here on one side only, contrary to figure 3.1, and as suggested by equation 3.6. This is because varying l maintains the

same Ro/Fr ratio, which is not the case in Figure 3.1 since Fr is constant. By varying Ω or N (not shown) we also find 2 limits for Rossby waves.

In figure 3.13a we see that the non-traditional beta plane has little effect, compared with the use of tilted $\mathbf{\Omega}$ with traditional β-plane. For the non-traditional β-plane to exert significant influence, perturbations must propagate far vertically. This scenario is applicable, for instance, in Quasi-Geostrophic flows ($\Lambda \ll 1$). However, in this case, stress is dominated by stratification effects, so rotation effects can only be seen if $Fr^{-1} \ll 1$. This configuration is illustrated in figure 3.13b showing the comparison between the complete non-traditional approach and the tilted traditional β-plane. We see that even in this case, variations are still low. In summary, non-traditional effects appear to be negligible for the majority of CMB-relevant parameters, most of the physical effects being carried in the tilted traditional approximation.

SUMMARY OF THE CHAPTER

- We reviewed and characterised the different stress regimes, from inviscid hydrodynamic flows to MHD.
- We described the wave propagation under subcritical laminar regimes (zone 1 and 4 of figure 3.14 for insulating fluid).
- Considering stress driven mainly by wave propagation, we describe the property of MHD topographic waves, distinguishing their different contributions to stress.
- We highlight the capital contribution of Rossby waves to surface stress, particularly for the CMB coupling.
- Therefore, we show that it is crucial to accurately model the variations of $\mathbf{\Omega}$ for the planetary layers employing the β-plane.
- It can be noted that tilted $\mathbf{\Omega}$ and traditional β-plane explain most of the physics, β-effects on horizontal component of $\mathbf{\Omega}$ inducing small effects

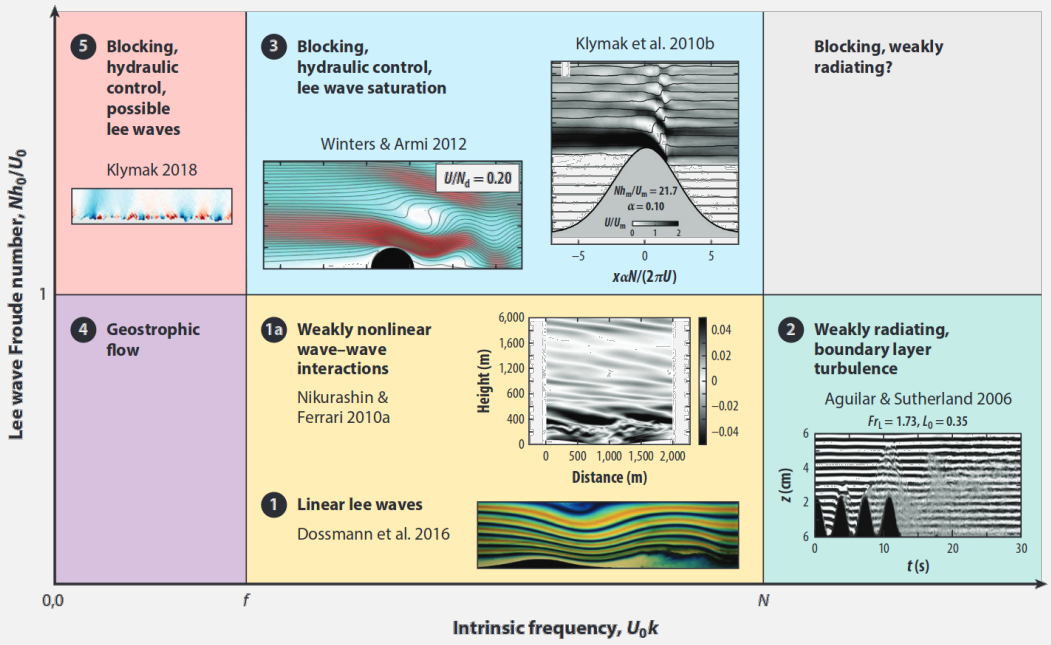

Figure 3.14: Regime diagram for oceanic lee waves, from Legg (2021). The upper part of the diagram corresponds to the flows where the Froude number constructed with the topography height is larger than one (supercritical flows). The right part of the diagram ($Frll1$) is also supercritical. Our model can only handle subcritical flows (1,1a, and 4), separated between two regimes: geostrophic flow and lee waves.

4 Oscillating flows - Nutation

Contents

Earth's motion of precession and nutation, whose equations are presented in the section 1.1.1, has oscillation frequency in the rotation axis frame comparable with the spin rate of the Earth. For this reason, contrary to the variation of the spin rate (LOD), we need to take these oscillations into account in our calculation. In this chapter, we study the physics of flows that oscillate on a topography and how they differ from steady flows. The emphasis will be on the imaginary part of the coupling (which is what we are interested in for nutation measurements) and on the associated energy dissipation. Unlike in chapter 3, the model is improved by adding electrical conductivity to the solid.

In this section, we first compare our non-rotating hydrodynamic results with direct numerical simulations. The oscillation of the fluid allows us to obtain a boundary layer in this configuration (Stokes layer), which allows us to handle the problem both by direct numerical simulations (DNS) and ToCCo. We will then study the effects arising from the electrical conductivity of the solid and its influence on the Ohmic dissipation, both on the fluid and solid sides. In section 4.3 we investigate the stress on the boundary for different frequencies and its link with dissipation processes. We then conclude with some geophysical applications in section 4.4.

4.1 Benchmark with DNS

Calculating the three-dimensional MHD flow of a stratified fluid on a bumpy solid (insulating or conducting) medium is difficult to achieve with DNS. To be able to benchmark our code, we place ourselves here in the 2D case of a simple Stokes boundary layer for parameters that are simple to achieve for the simulation. This setup can also be easily done with our code. The calculation can be 2D because there is neither rotation nor magnetic field, but also because we are using a ridge topography. The purpose here is to compare the DNS and our semi-analytical approach to validate

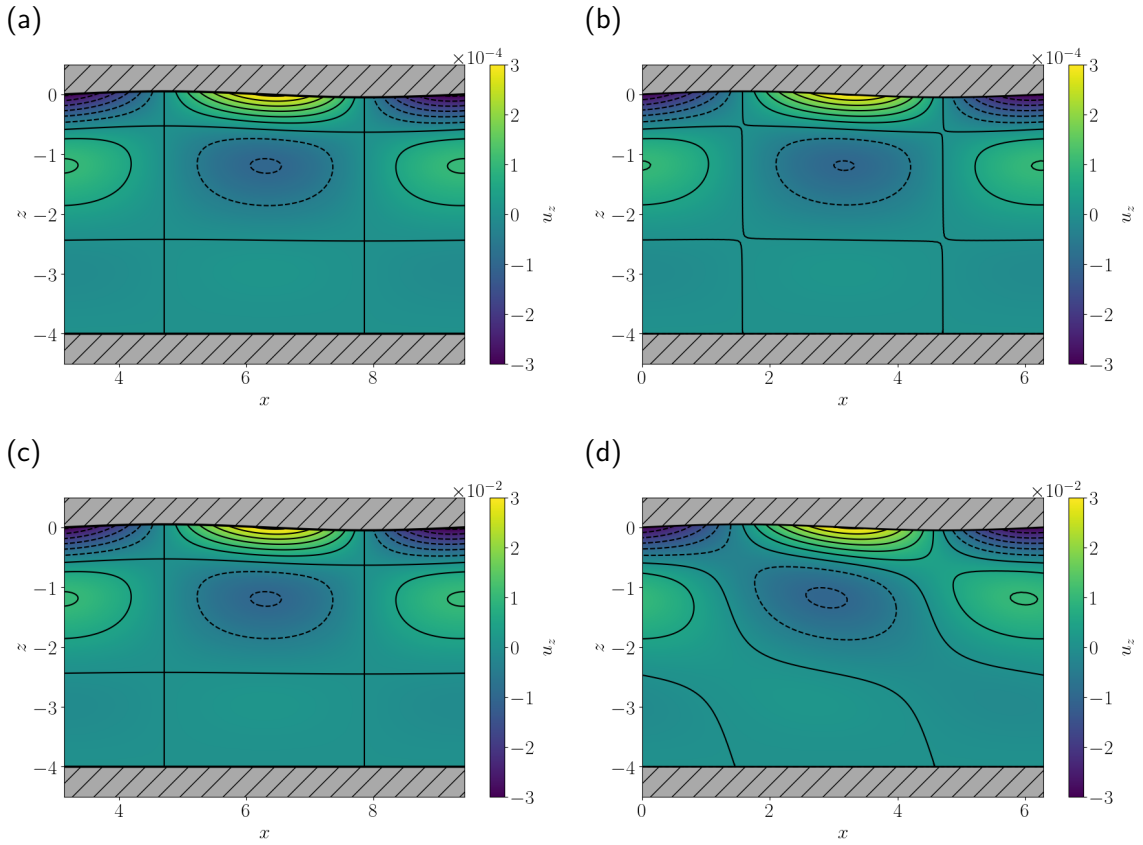

Figure 4.1: Comparison of the vertical velocity field between our code at order $m = 2, n = 1$ **(left)** and DNS calculations **(right)**, with $\epsilon_v = 10^{-2}$ **(top)** and $\epsilon_v = 1$ **(bottom)**. Calculations are performed without a magnetic field or rotation. The top boundary is stress-free and bumpy with a topography $h = 0.05 \sin x$, and the second boundary at $z = -D = -4$ is flat and no-slip. The base flow is $\boldsymbol{u}_0 = \epsilon_v \sin(t)\mathbf{1}_x$. Parameters: $Ro^{-1} = 0$ $Fr = 0.1$, $Re = Pe = 1$, $\tilde{\eta}^{-1} = 0$.

our code in a viscous case on a bumpy boundary.

To do so, a finite element model with a bumpy boundary has been developed with the COMSOL Multiphysics ® software to perform direct numerical simulations. To control numerical diffusion effects due to the mesh grid, this model uses finite diffusivities, and thus we consider in this section a non-zero viscous term in the Navier-Stokes equation 2.2a as well as a diffusive term $Pe^{-1}\nabla^2 a$ on the right-hand side of the density equation 2.2b (with the Peclet number Pe). This provides us with a simple benchmark. In figures 4.1 we show the vertical velocities for DNS and ToCCo calculations and for different ϵ_v. As expected, the flows are in very good agreement for $\epsilon_v = 10^{-2}$ (figures 4.1a and 4.1b). Increasing ϵ_v (figures 4.1c and 4.1d), calculations tend to disagree. This results from a bulk asymmetry of the flow DNS.

We then show, in figure 4.2a, the viscous and total stresses (viscous and pressure) on the top boundary. These are in excellent agreement. Figure 4.2b corresponds to the absolute difference between DNS and our code. As expected, the error is roughly of the order of ϵ_t^2 (black dotted line).

For these calculations, we perform our calculations in order $\epsilon_t^2 \epsilon_v$. The technique of using a

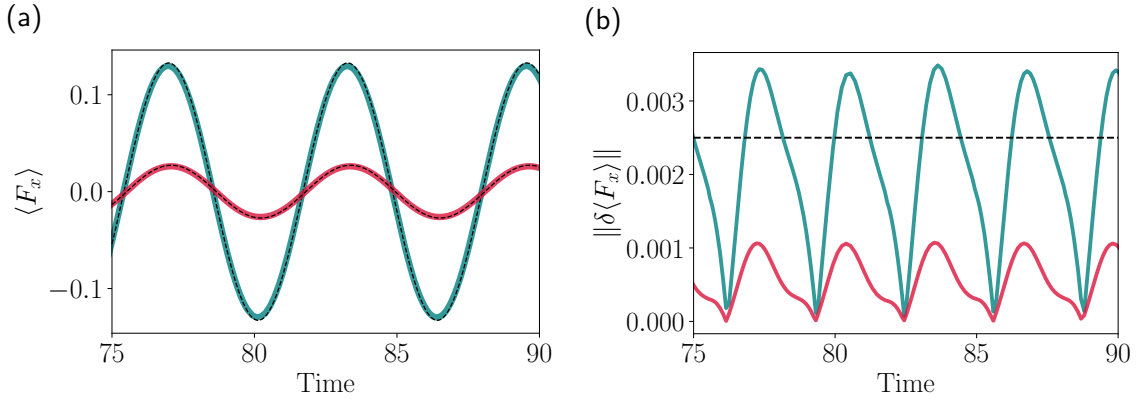

Figure 4.2: **(a)** Comparison of average horizontal stresses on a bumpy, stress-free boundary obtained with our code of order $\epsilon_t \epsilon_v$ (dashed) and with finite element DNS calculations (solid). The blue line represents the total stress, and the red line is the viscous one. **(b)** is the associated absolute difference. The black dashed line is $\epsilon_t^2 = 0.0025$ The parameters are the same as in the figure 4.1.

solution at a given order to find the stress at the next order does not work for viscous stress (see Section 2.3). Therefore, a second (or higher) order calculation must be performed[1]. Unlike flat boundaries, the viscous force along the basic flow direction is non-zero for a stress-free bumpy boundary. The topography indeed allows normal viscous stress to generate a non-zero horizontal viscous drag (see the box on page 34).

4.2 Electrically conducting (solid) boundaries

An electromagnetic coupling between the fluid core and the mantle has been proposed for a smooth spherical CMB and a conducting layer at the base of the mantle, to explain the decadal variation in the length of the day (Rochester, 1960; Roberts, 1972). Still, it appears to require a large conductance ($\approx 10^8$ S, see Holme, 1998). It has also been suggested that this could also explain some nutation observations (Buffett, 1992), leading to the same conductance value. Therefore, Buffett (2010), which will also be referred to hereafter as BF10, suggested combining topographic and electromagnetic coupling (in a local model) to explain the out-of-phase component of annual nutation. He used a conductivity of $\sigma_s = 10^3$ S/m, which is at the high end of the range expected for the lowermost mantle (which is between 2 S/m and 10^4 S/m, see Jault, 2015). He used total energy dissipation in the fluid and solid to estimate the coupling strength.

In this section, we consider a conducting solid to model the Earth's mantle and variations with latitudes of $\boldsymbol{\Omega}$ and $\boldsymbol{b_0}$. We consider oscillating flows, which localise magnetic perturbations close to the CMB. For a flat boundary, the propagation length of the perturbation $\delta_{f,s} = k_z^{-1}$ is given by (see equation 20 of BF10)

$$\delta_s = \sqrt{\frac{2\tilde{\eta}}{\omega Rm}}, \qquad \delta_f = \sqrt{\frac{2}{\omega Rm}}, \tag{4.1}$$

[1] which is intractable by hand.

$_s$ and $_f$ denoting the solid and fluid sides. The solid is modelled, in our case, by a semi-infinite medium. The oscillation frequency and conductivity are then the only parameters that drive the effective conductance of the solid. Therefore, this approximation is acceptable only for certain parameters if we are interested in a conductive layer of limited thickness (such that δ_s is smaller than this layer).

As in Buffett (2010), we investigate Ohmic dissipation, which corresponds to the phase shift of stress (imaginary part) to forcing, in the absence of other sources of dissipation. In this section, we use an illustrating simplified oscillating flow, $\boldsymbol{u}_{su} = \sin\theta\cos(\omega t)\mathbf{1}_x$, instead of using a geophysically relevant (but more complex) flow. We calculate the magnetic dissipation φ as the integral of $Rm^{-1}\,\tilde{\eta}\,j^2$ throughout the solid and $Rm^{-1}\,j^2$ throughout the fluid. Here, the fluid and solid are semi-infinite.

Taking first into account the order $m = 0$ corresponding to a flat boundary, we calculate the dissipation due to electromagnetic coupling as a function of the conductivity ratio $\tilde{\eta}$ (figure 4.3a). All curves are superimposed because the dissipation scales as $\omega^{-1/2}$. In the flat case considered here, our results agree in the whole range with the predictions obtained from equations 19 and 24 of BF10, which provide the mean dissipation in the solid (dashed orange), in the fluid (dashed blue), and their sum (dashed black). These two dissipations can actually be obtained from a single formula, which reads as follows in our notation.

$$\varphi_{s,f} = \frac{Rm\delta_{s,f}}{16Al^2\left(1+2\tilde{\eta}^{1/2}+\tilde{\eta}\right)}, \tag{4.2}$$

Then, for $\tilde{\eta} \ll 1$ (solid conductivity larger than the one of the fluid), the dissipation scales as $\tilde{\eta}^{1/2}$ for the solid and is $\varphi_f = \sqrt{2Rm}/(16Al^2\sqrt{\omega})$ for the fluid (thus independent of $\tilde{\eta}$). The total dissipation becomes then dominated by the dissipation on the fluid side. In the opposite limit $\tilde{\eta} \gg 1$, it is $\tilde{\eta}^{-1/2}$ for the solid and $\tilde{\eta}^{-1}$ for the fluid, leading to a total dissipation located mainly on the solid side.

Considering now a bumpy boundary, the topographic coupling leads to additional dissipation (figure 4.3b), which scales as ϵ_t^2. In the limit $\omega \gg 1$, the dissipation scales as $O(\omega^{1/2})$, which is the same scaling as for a flat boundary. It occurs mainly in the solid for $\tilde{\eta}^{-1} > 1$ and in the fluid otherwise. The vertical wave numbers k_z obtained vary as $\omega^{1/2}$ for $\omega \gg 1$ (This can be seen in the appendix in figure A.1). The stress scales as k_z, which explains the observed scaling $\varphi \propto \sqrt{\omega}$. However, the dissipation cannot increase indefinitely with ω and, in our model, it is limited by the acceptable limit on $\epsilon_t < O(k_z^{-1})$. Assuming k_z for a flat boundary is a good approximation of the magnetic skin thickness. For a value of $\eta = 0.8$ m^2 s^{-1} and a diurnal oscillation, we obtain a magnetic skin length of ≈ 148 m. This is the skin length on the fluid side, which is the smallest in the geophysically relevant limit $\tilde{\eta} > 1$.

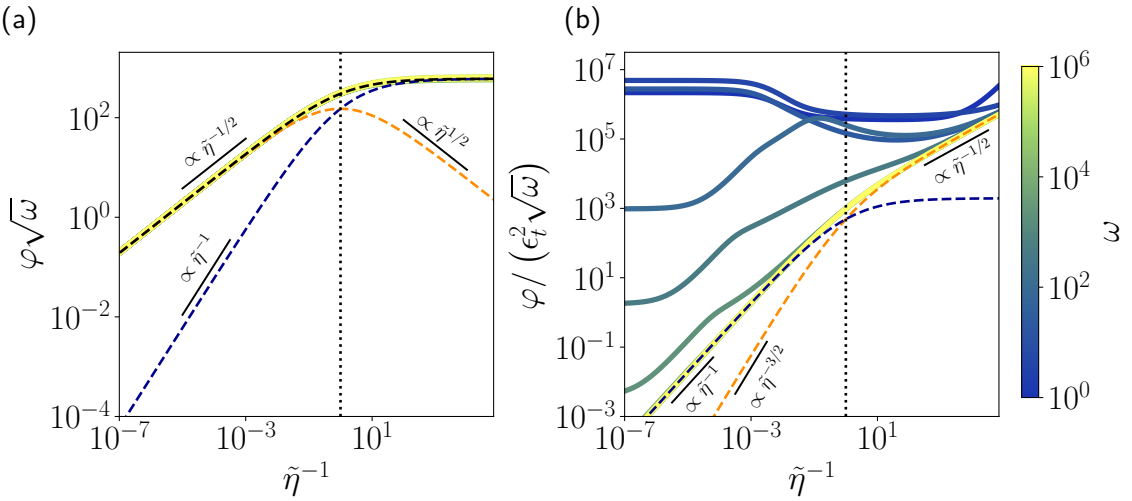

Figure 4.3: Normalised mean dissipation as a function of $\tilde{\eta}^{-1}$, at order in topography $m = 0, n = 2$ **(a)**, corresponding to a flat boundary, and the order $m = 2, n = 2$ alone **(b)**. Other orders terms are identically zero, and the full dissipation is the sum of both orders. Dissipation is calculated for a set of ω (colour), with $\boldsymbol{u}_{su} = \sin\theta\cos(\omega t)\mathbf{1}_x$. The vertical dotted line is $\tilde{\eta}^{-1} = 1$. The dashed lines are the theoretical results for total (black), fluid (blue) and solid (orange) dissipation, after the results of BF10 in figure **(a)**, and after our results at $\omega = 10^6$ in figure **(b)**. Parameters : $\boldsymbol{b}_0 = \sin(\theta)/2\,\mathbf{1}_y - \cos\theta\mathbf{1}_z$, $\boldsymbol{\Omega}$ is from equation 2.8 and $\theta = \pi/4$. Other parameters are those in Table 2.2 for $\tilde{k}^{-1} = 100$ km.

4.3 Waves stress and dissipation

In this section, as done in section 3.1 for steady flows, our objective is to characterise the dissipation due to an oscillating flow. We opted to maintain the same exploration of parameter space, investigating dissipation as a function of both the Rossby number (Ro) and the interaction parameter (Rm/Al^2). The Lehnert number is again kept constant. Since we already showed in previous chapters the importance of β-plane, we choose here to concentrate only on calculations with a rotation vector given by equation 2.7, which captures most of the β-effects (see section 3.5.3). Since the precession and nutation motions that have the largest amplitude are diurnal in the mantle frame, we consider $\omega = 1/Ro$ in figures 4.4a and 4.4b. We also explore in figures 4.4c and 4.4d the deviation from this diurnal frequency. In 4.4, in the same way as in figure 3.2, the different dimensionless parameters are evaluated in a way that keeps $\tilde{k}$, Ω_0, $\tilde{B}$, ρ_r, and η_s constant[2].

As seen before, we see that we can delimit two regimes: MHD regime when $Rm/Al^2 > 1$ and hydrodynamic regime when $Rm/Al^2 < 1$. The core of the Earth and the ocean are, respectively, in these two domains. In all the cases shown in figure 4.4 we observe a sharp transition at high Rossby. This corresponds to a property of gravito-inertial waves. This limit can then be derived from its dispersion relation. This effect then arises only on the fluid side. Finding the limit where the imaginary part of k_z becomes non-zero, we obtain the equation of this line, given by

$$Ro^2\left(-Fr^2Ro^2\omega^4k_H^2 + 4Fr^2\omega^2\left(k_x^2\cos^2\theta + k_y^2\right) + Ro^2\omega^2k_H^2 - 4k_H^2\cos^2\theta\right) = 0. \tag{4.3}$$

[2]Horizontal axis is $\propto Rm^2 \propto \omega^{-1} \propto Al \propto \tilde{\eta} \propto Ro$.

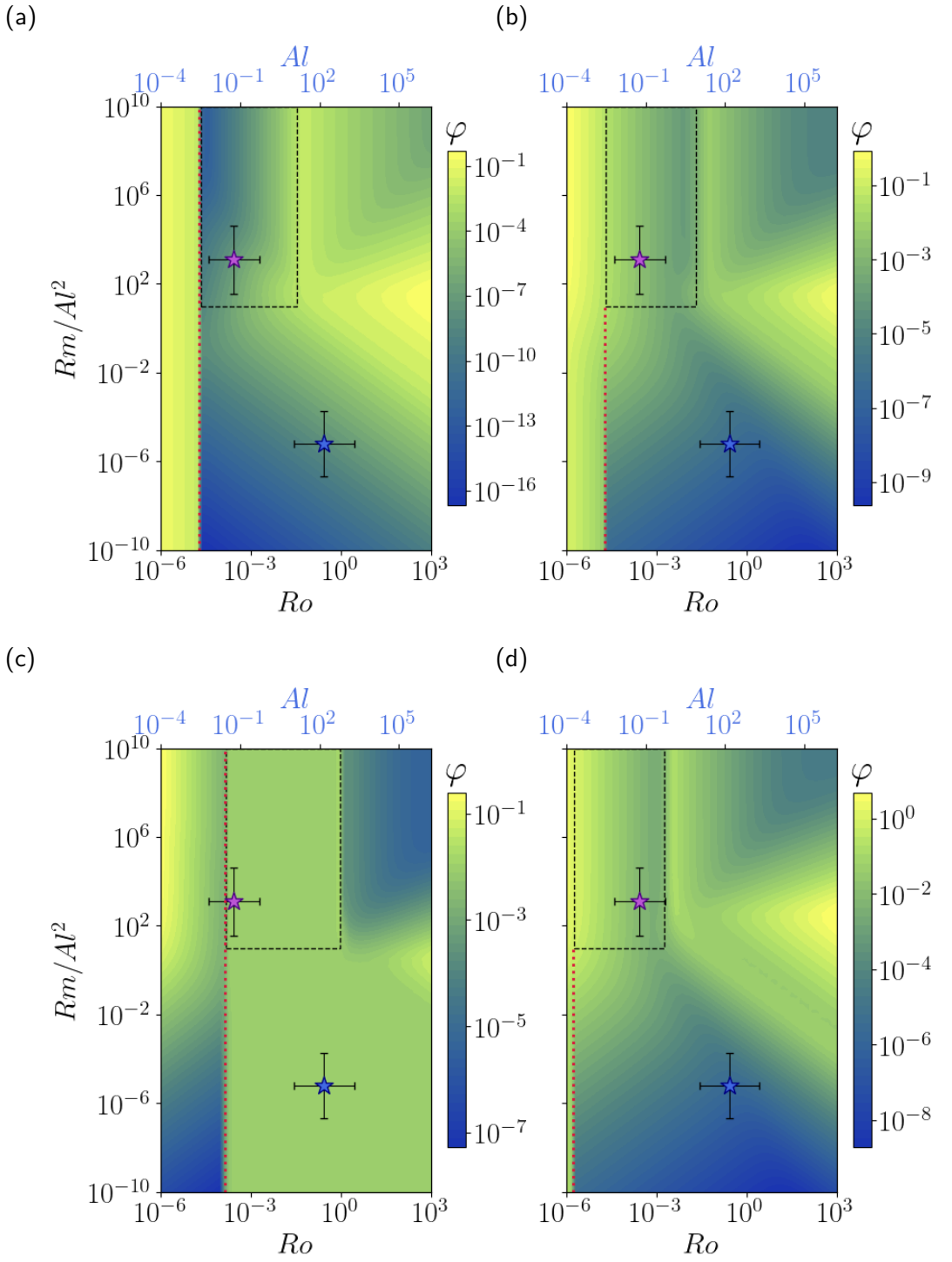

Figure 4.4: Dissipation (colours) as a function of interaction parameter Rm/Al^2 and Ro at $\theta = \pi/4$ for **(a)** an insulating solid and **(b,c,d)** an conducting solid at constant $\tilde{\eta} = 10^4$ (corresponding to a constant conductivity $\sigma_s = 50$ S/m). The topography has an eggbox shape with $\epsilon_t = 10^{-3}$, the base magnetic field is dipolar, and the rotation vector is that of equation 2.7 (traditional tilted β-plane). The base flow is equation 2.29 with $\omega = 1/Ro$ (diurnal oscillation) for **(a)** and **(b)**, $\omega = 10/Ro$ for **(c)** and $\omega = 0.1/Ro$ for **(d)**. dissipation is shown for $\chi = 0.0287$, that is, $\tilde{k}^{-1} = 100$ km for the core and $\tilde{k}^{-1} = 183$ km for the ocean. The stars represent the Earth's core (purple) and the ocean (blue). The red line is equation 4.3. Other parameters are those of table 2.2 at $\tilde{k}^{-1} = 100$ km.

Noting $\omega' = \omega Ro$, as it is the case in our figure, this expression can be simplified as

$$Ro = \omega' Fr \sqrt{1 - \frac{4k_y \sin^2\theta}{k_H^2 \left(\omega'^2 - 4\cos^2\theta\right)}}, \tag{4.4}$$

which gives $Ro = \sqrt{2}Fr$ for the parameters of figures 4.4a and 4.4b. In the MHD case, this sharp transition is smoothed out by solid dissipation. This zone, on the right of the line of equation 4.3, is where the influence of the conductivity of the mantle is most pronounced. Note that the Earth's core parameters are in this zone. In the appendix (figure A.2) we provide two analogous figures from figure 4.4b, for $\sigma_s = 0.1$ S/m and $\sigma_s = 10^3$ S/m, confirming the strong influence of solid conductivity.

For $Rm/Al^2 > 1$, we can identify another regime change, which is particularly clear in figure 4.4c. We have not managed to obtain this limit analytically. However, it clearly corresponds to a transition of the waves, from gravito-inertial waves on the left to Alfvén waves on the right side.

We focus now on the parameter range of interest for the Earth's core (black dashed box in the figure 4.4), located between the two limits discussed above. In cases where $\omega Ro \geq 1$, the waves become dependent on ωFr but independent of Ro in figure 4.4a, which explains why the waves (and thus the stress and dissipation) vary along the horizontal axis (ωRo being kept constant). Contrary to this insulating boundary case, the decreasing dissipation along the horizontal axis that can be observed in the figures 4.4b and 4.4d is mainly due to the dissipation of order $m = 0$ (flat boundary part) in the solid (see figure 4.3). We have checked that this decrease scales as expected from equation 4.2 at the limit $\tilde{\eta} \gg 1$ (see also figure 4.3). In figure 4.4c, the dissipation is constant, which is not the case for other values of ωRo. In fact, when $\omega Ro < 1$ (figure 4.4c), the waves behave mainly as inertial waves (which are independent of Fr). The value of ωRo being kept constant in this figure, the vertical wave number of the waves is constant (see the inertial wave dispersion relation A.6), as well as the stress and dissipation.

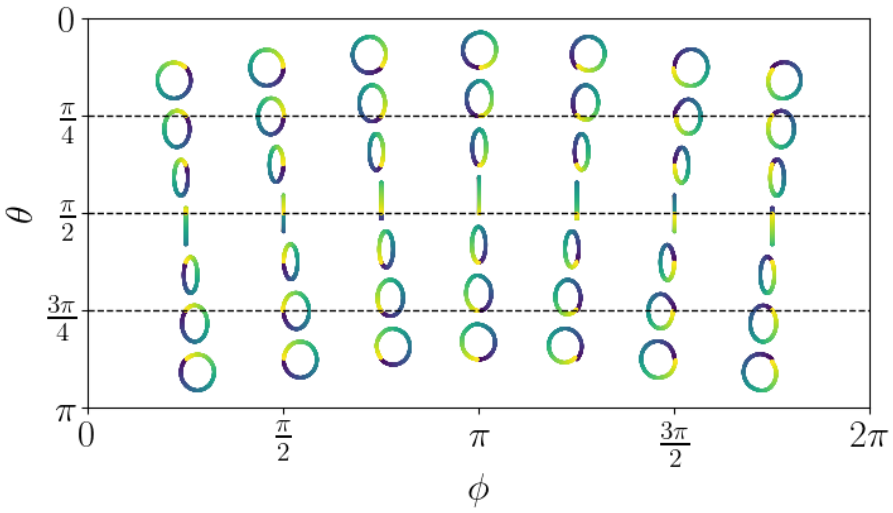

Figure 4.5: Trajectories of fluid particles at the CMB (numerically integrated), forced by nutation motion. This corresponds to the base flow of equation 2.29 rescaled with $\tilde{U} = 8 \times 10^{-5}$ ms^{-1} (see Buffett, 2010). A factor 5×10^5 amplifies the trajectories to make them visible. The colour corresponds to time (from yellow to blue), in a period $2\pi/\omega$.

4.4 Application to dissipation of nutation

Precession and nutation wobbles that lie on the equatorial axis induce oscillating flows through the pressure coupling as a result of the flattening of the Earth and the viscous coupling. These flows, given in their general form by the equation 1.1c, can be projected into the local frame. The leading order corresponds to the equation 2.29, given by BF10. We show in figure 4.5 the trajectories of fluid particles given by equation 2.29. It corresponds to an oscillating flow in the y direction at the equator, which progressively becomes a flow that gives circular trajectories toward the poles. This circular motion spans all flows' directions and shows us the importance of modelling the topography by a 3-dimensional shape.

In the case of the well-measured quasiannual nutation motion at $\approx$ 366.3 sideral days (see BF10), a phase lag is observed between response and forcing. This phase lag can be expressed as an Ohmic dissipation for an inviscid fluid. Buffett (2010) shows that a dissipation of approximately 9 MW is necessary to explain this discrepancy. In figure 4.6 we show the topography height needed as a function of the wavelength to obtain this value. As in BF10, the calculation is performed at one latitude[3] to obtain surface dissipation, then multiplied by the surface of the CMB ($\approx 1.52 \times 10^{14}$ m^2). We superpose our values obtained with the topography model of figure 3.12a. Figure 4.6a corresponds to the BF10 parameters (red square) for three colatitudes, 0, $\pi/4$, and $\pi/2$ rad (BF10 is at $\theta = 0$). We see that our results differ significantly between latitudes, especially for low stratification and mantle conductivity, and particularly for large wavelengths. In any case, with our CMB topography model (red dashed dotted line), it seems difficult to achieve this level

[3]Calculations are performed at the pole, we have done the same, but we also checked the robustness of this result by considering $\theta = \pi/4$ and $\theta = \pi/2$.

Precession flow

When projected in the local frame, the full expression of the precession flow is given by (Pais & Le Mouel, 2001)

$$\begin{aligned} \boldsymbol{u}_{su} = r\left[\delta_3 \sin\theta - (\delta_1 \cos(\omega t + \Phi) + \delta_2 \sin(\omega t + \Phi))\cos\theta\right]\mathbf{1}_x \\ - r\left[-\delta_1 \sin(\omega t + \Phi) + \delta_2 \cos(\omega t + \Phi)\right]\mathbf{1}_y, \end{aligned} \tag{4.5}$$

$\delta_{1,2,3}$ being the differential rotation coefficient corresponding to each component of the global Cartesian frame, δ_3 referring to the rotation axis.
The azimuthal drift term $\delta_3 \sin\theta$ is small because δ_3 is of the order of 2 compared to $\delta_{1,2}$ (see equations 15-16 of Pais & Le Mouel, 2001). We chose to neglect it in this work. For low polar flattening, we also have $\delta_1 \approx -\delta_2$ (see again equation 16 of Pais & Le Mouel, 2001). Assuming that, we obtain

$$\boldsymbol{u}_{su} = \sqrt{2}\delta_1 r\left[(\cos\theta\cos(\omega t + \Phi))\mathbf{1}_x - \sin(\omega t + \Phi)\mathbf{1}_y\right], \tag{4.6}$$

which is equivalent to the equations 11-12 of Buffett (2021) with $\tilde{\omega}_f = \sqrt{2}\delta_1$, and also to our non-dimensional equation 2.29.

of dissipation without sufficient stratification and/or high mantle conductivity. This would require them to be at least equal to or higher than those used here.

In appendix A.4 we also provide the same calculations for an insulating mantle. We observe that the conductivity of the mantle has a secondary influence for dissipation in the case of strong stratification (except for very large topography). In this case, we could say that mantle conductivity is not necessary to explain dissipation. This has also been shown by BF10 (see figure 3.b). However, non-zero mantle conductivity is essential for moderate stratification.

For every colatitude, we observe that we obtain results of the same order of magnitude as BF10 who only considered $\theta = 0$. In this specific case, our calculations differ by a factor of ≈ 2.5. There are several reasons for this. First, the approximations made (see table 2.7) inevitably cause our calculations to differ. Second, in BF10 equation 9 provides the topography used, which corresponds to a ridge topography orientated between the x and y axes. This does not correspond to figures 1 and 2 of his paper, which shows egg-box topography[4]. We chose to compare his results with our results in the case of an egg-box topography (which seems more relevant than tilted ridges). Using a ridge shape significantly reduces the gap between our calculations. The dissipations at order ϵ_v^2 are identical, since they correspond to a flat boundary. However, at order $\epsilon_v^2\epsilon_t^2$, the ridge topography dissipation φ_{ridge} and the egg-box one φ_{egg} are exactly related by $\varphi_{\text{ridge}} = 2\varphi_{\text{egg}}$. Finally, we noticed that the ansatz presented in equation 10 cannot solve the non-penetration condition as presented, as some terms were missing. Although this does not invalidate the whole calculation, it can easily explain a factor of 2.

In figure 4.6, we have followed the approach of Buffett (2010), calculating the dissipation with

[4]Equation 9 is equivalent to $h = \epsilon_t \sin(x + y)$, while figures 1 and 2 corresponds to $h = \epsilon_t \sin(x)\sin(y)$.

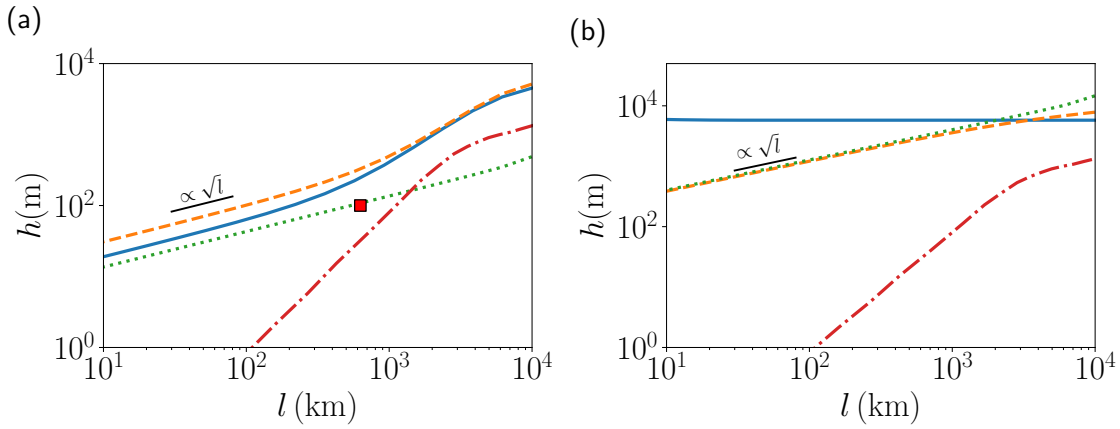

Figure 4.6: Topography height that is needed to explain the out-of-phase component of the annual nutation (calculated via Ohmic dissipation 9 MW). Surface dissipation is calculated at $\theta = 0$ (solid blue), $\theta = \pi/4$ (dashed orange), and $\theta = \pi/2$ (dotted green). This surface dissipation is then multiplied by the surface of the CMB. The red dashed-dotted line is the CMB topography model of figure 3.12a. The red square is the result of Buffett (2010). The base flow is equation 2.29 and the magnetic field is dipolar. The topography has an egg-box shape $h = \epsilon_t \cos x \cos y$. Parameters : $\tilde{B} = 5\times10^{-4}$ T, $\rho = 10^4$ kg m^{-3}, $\Omega_0 = \omega = 7.292 \times 10^{-5}$ s^{-1}, $\tilde{U} = 8 \times 10^{-5}$ m s^{-1}, $\eta = 1.592$ m^2 s^{-1} ($\sigma = 5 \times 10^5$ S m^{-1}), $\tilde{\eta} = 500$ ($\sigma_s = 10^3$ S m^{-1}). In **(a)**, $N/\Omega_0 \approx 1240$ and which is a parameter of BF10, and in **(b)**, $N/\Omega_0 = 1$ (Buffett, 2014).

a single latitude. While this should provide good orders of magnitude, we can expect the result to be significantly modified when considering the proper dissipation at each latitude and integrating the results on the whole sphere. Our method enables us to perform this calculation that will be done and discussed in section 5.1.1.

Summary of the chapter

- Motivated by the CMB flow driven by Earth's nutations, topographic effects with time-dependent basic flows have been investigated.
- Extending our semi-analytical code to viscous flows (with no-slip or stress-free topographies) and buoyancy diffusion, we successfully retrieve DNS results.
- As new boundary conditions, we introduce the electrical conductivity of the solid and observe its effect on stress. We have shown the important influence of the oscillation frequency and have explored the asymptotic cases.
- We ended up linking our dissipation calculations to nutation measurements and comparing with previous works.
- Although not addressed, our method could be applied to subsurface oceans of librating ice satellites (*e.g.* Kvorka *et al.*, 2018; Van Hoolst *et al.*, 2013).

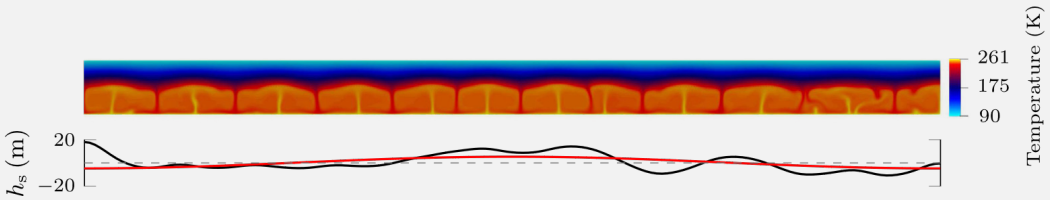

Figure 4.7: Snapshots of the temperature field and surface topography (black lines) obtained from numerical models. The red curve represents the long-wavelength component of the topographic signal and the black dashed line is the reference flat topography. (Figure from Kihoulou *et al.*, 2023).

5 Discussion and perspectives

Contents

In this concluding chapter, we return to the initial motivations for this work and discuss how extrapolating our local model results toward global geometries or to Earth models. We discuss how to better take into account the spatial variations of the CMB stress and how this complexity can be considered in the estimate of the coupling. We then point out some of the limitations of the local models that we have studied. We give some thoughts on how to fill the gaps in local models and why studies mixing local and global are needed. We end with a conclusion and some long-term perspective.

5.1 On-going work and short-term perspectives

We have begun to explore some paths that seem promising but could not be completed before the end of this thesis. To make additional progress, more effort or cooperation with other researchers would be necessary. I present here some preliminary work done as well as perspectives.

5.1.1 From local models to global geometries

Our model allows us to compute the average stress and dissipation per unit of surface at each latitude, taking into account the variation in latitude of the rotation and the magnetic field effects. Thereafter, we can integrate these results on the surface of the CMB. The overall value obtained

in this way should be more reliable than the extrapolation of a value calculated at a single latitude. Significant differences can exist when the angle between the magnetic field, the rotation vector, and the topography vary. Moreover, the coupling parameters in the AMD nutation models (Mathews *et al.*, 2002; Koot *et al.*, 2010), and the LOD models as well (Roberts & Aurnou, 2012) measure the strength of torques, which are integrated values.

In figure 5.1 and 5.2 we show the topography height needed to explain LOD data (typical torque of 10^{18} Nm, see Roberts & Aurnou, 2012; Jault, 2020) and nutation properties (typical dissipation of 9 MW, see Buffett, 2010), respectively. We choose to use the dissipation approach used by Buffett (2010) since the link between the stress provided by our code and the imaginary part of K_{CMB} remains to be addressed. We investigate this problem for an insulating mantle. In both cases, we did not consider any variations in the longitude of the parameters and performed the calculation only on the north hemisphere. This can be done because stress and dissipation are symmetric on both sides of the equator despite the opposite values of $\mathbf{1}_z \cdot \boldsymbol{b}_0$ and $\mathbf{1}_z \cdot \boldsymbol{\Omega}$. In figure 5.3a, we show the spatial variations of the stress used to integrate the torque. Here, we can see variations in stress of several orders of magnitude between latitudes. We have checked that the stress is indeed symmetrical. Figure 5.3b shows the stress as a function of latitude and its mirror image relative to the equator. The residual of their subtraction is exactly zero. We can then integrate the torque as follows

$$\tilde{\Gamma}_z = \int_0^{2\pi} 2 \int_0^{\pi/2} R \sin\theta \langle \tilde{F} \rangle \, R^2 \sin\theta \, \mathrm{d}\theta \mathrm{d}\phi = 4\pi R^3 \int_0^{\pi/2} \langle \tilde{F} \rangle \sin^2\theta \, \mathrm{d}\theta \tag{5.1}$$

where $\langle \tilde{F} \rangle$ depends on the colatitude θ.

For nutations calculations, the base flow is the one of equation 2.29. For LOD we consider as a first approximation that the average flow at the CMB is at first order a solid body rotation around the rotation axis Ω_0. Locally, the base flow can be written as $\boldsymbol{U}_0 = \tilde{U} \sin\theta \mathbf{1}_x$, with $\tilde{U} = 10^{-4}$ m s^{-1} (for CMB velocity estimates, see Gillet *et al.*, 2015).

In figure 5.1 we show the difference between a calculation made at mid-latitude with a torque integrated with latitude for the LOD application. We observe only a small difference between the two estimates since the mid-latitude calculation is close to the average value (contrary to the pole or the equator, see figure 5.3). We also compared our CMB topography model with these results and found that for large topography wavelengths, a weak stratification is sufficient (approximately $N/\Omega_0 = 0.1$).

We then did the same work for the dissipation of annual nutation, comparing the dissipation at the pole (figure 5.2a), as did Buffett (2010), with an integrated value. For this nutation problem, the results are more different between the pole and the integrated value. We see that in both cases, the stratification needed to explain the data with our topography model is high compared to what we expect for the core. Also, it does not seem possible to find parameters that account for both LOD and nutation. All this suggests that the pressure coupling is not sufficient on its own. Buffett (2010) already showed that electromagnetic coupling can, in the presence of topography, lead to a sufficient dissipation with weaker stratification.

We can perform calculations on a conducting boundary with rapidly oscillating flows. But

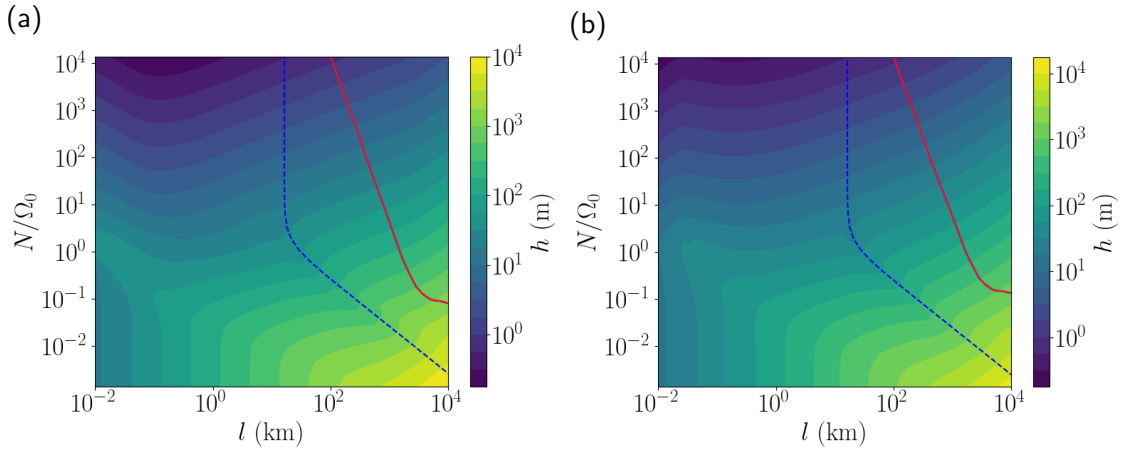

Figure 5.1: Topography height (colour) necessary to explain the LOD variations (10^{18} Nm, see Roberts & Aurnou, 2012; Jault, 2020) as a function of the wavelength of the topography l and the Brunt-Väisälä frequency N. In **(a)** value is estimated from the mean local value of the stress (2.4×10^3 Nm^2). Calculations are made at the colatitude $\theta = \pi/4$. In **(b)** the stress is calculated at 8 latitudes on one hemisphere and by symmetry is integrated on the surface of the CMB to obtain the torque. The red line is where the topography model of figure 3.12a corresponds to the estimate of h. The blue dashed line correspond to equation 3.14 The mantle is insulating. The base flow is $\boldsymbol{u}_0 = \sin\theta \mathbf{1}_x$ and the magnetic field is dipolar. Parameters: $\omega = \Omega_0 = 7.29\times10^{-5}$ s^{-1}, $\tilde{B} = 5\times10^{-4}$ T, $\tilde{U} = 10^{-4}$ m s^{-1} and $\tilde{\eta}^{-1} = 0$.

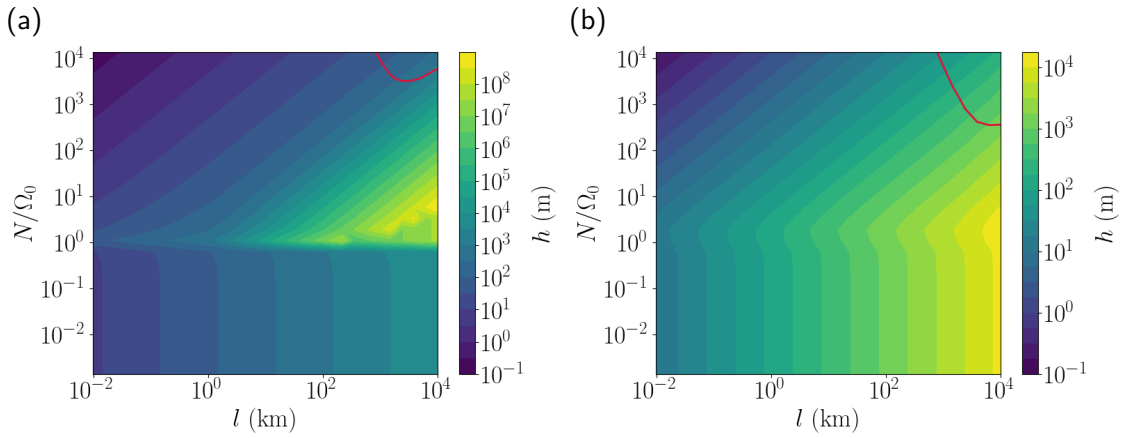

Figure 5.2: Topography height (colour) necessary to explain the dissipation of the annual nutation (9 MW, see Buffett, 2010) as a function of the wavelength of the topography l and the Brunt-Väisälä frequency N. In **(a)** dissipation is calculated at the pole and multiplied by the surface of the CMB (1.527×10^{14} m^2). This is the approach of Buffett (2010). In **(b)** the dissipation is calculated at 8 latitudes on one hemisphere and by symmetry is integrated on the surface of the CMB. The red line is where the topography model of figure 3.12a corresponds to the estimate of h. The mantle is insulating. The base flow is that of equation 2.29 and the magnetic field is dipolar. Parameters: $\omega = \Omega_0 = 7.29\times10^{-5}$ s^{-1}, $\tilde{B} = 5\times10^{-4}$ T, $\tilde{U} = 8\times10^{-5}$ m s^{-1} and $\sigma = 5\times10^5$ S m^{-1}.

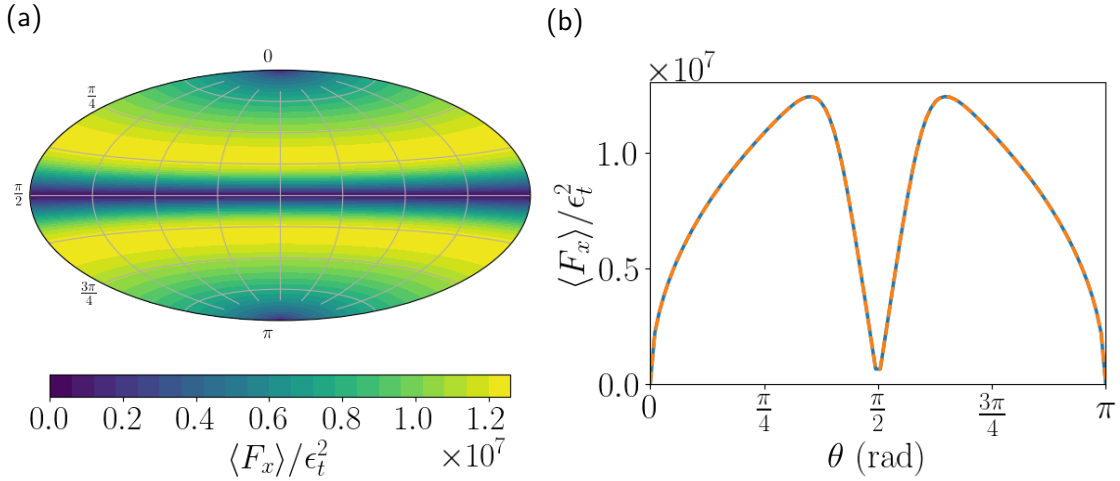

Figure 5.3: Stress as a function of latitude on both hemispheres for a solid body rotation flow. **(a)** Stress model extrapolated from calculations on the north hemisphere, used to calculate the torque. **(b)** Stress as a function of colatitude (solid line) and its mirror image relative to $\pi/2$. We see perfect symmetry around the equator. The parameters are those of table 2.2 for $\tilde{k}^{-1} = 100$ km.

because we assume an infinite half-space conducting mantle, we cannot do this calculation for a steady flow. A steady flow results in a linear solution of the magnetic field in the mantle. The perturbation therefore does not decay at infinity, which is a problem for the boundary conditions at infinity. This is also a problem for slowly oscillating flows, as it involves a very thick magnetic skin layer (see equation 4.1), which does not correspond to the conductive mantle we want to model. We then cannot compare our nutation results on the conducting boundary with their LOD equivalent, while it could make it possible to find a common model for both problems. As a perspective, a possible solution that could be implemented in our code is to separate the mantle into two layers, a lowermost conducting and an insulating one. This would add an interface with its own boundary conditions and a new domain in which to solve the induction equation. But this could be managed using our approach, and this is part of our future project to improve ToCCo.

5.1.2 Fluxes at infinity: limitation of periodic models

In the frame of our periodic model, we have been able to calculate mean stresses that are not balanced by the mean acceleration of the fluid. Similarly, we find that the mean magnetic stress on the fluid side is non-zero, although the mantle is electrically insulating. We interpret these results as a limitation of periodic box models.

We observe that the Coriolis and Lorentz mean forces in the fluid balance the mean pressure force on the boundary. In a closed problem, the presence of mean Coriolis and Lorentz forces would be non-physical. In our model, these forces arise, respectively, from the mean flux of mass and electrical currents at infinity. The same effect occurs when we calculate a Hartmann layer (see

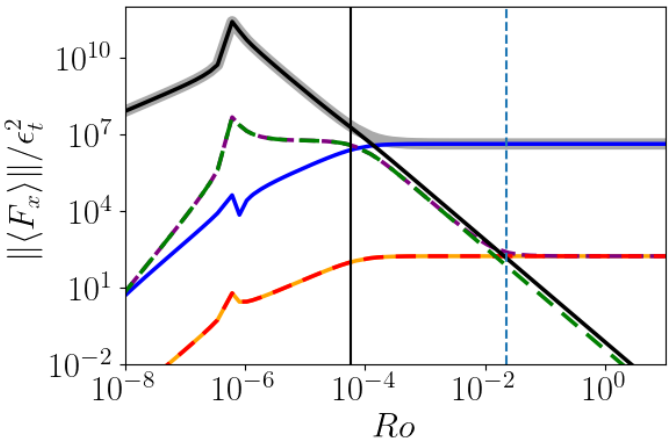

Figure 5.4: Magnitude of Lorentz (blue/purple), Coriolis (black/green) and $(\boldsymbol{u}\cdot\nabla)\boldsymbol{u}$ (orange/red) forces as a function of Ro, calculated at the surface (through the bumps, see equations 5.2, solid lines) and in the fluid interior (dashed). The grey line is the boundary pressure stress. The solid vertical line is $\Lambda = 1$, the dashed blue line is $Le = 1$. The parameters are those of table 2.2 for $\tilde{k}^{-1} = 100$ km, $\theta = 0$, $\tilde{\eta}^{-1} = 0$. The calculations are for a ridge topography with $\boldsymbol{\Omega} = \boldsymbol{b}_0 = \mathbf{1}_z$.

section 2.4.4), we obtain a steady flow and a mean stress corresponding to a pressure drop.

The linear solution induces a second-order volumetric flow rate and an electric current through the bumps (Jault, 2020) as

$$\mathcal{U} = \iint_S u_y(x,z),\mathrm{d}S = \int h(x)u_y(x,0)\,\mathrm{d}x, \qquad \mathcal{J} = \iint_S j_y(x,z)\,\mathrm{d}S = \int h(x)j_y(x,0)\,\mathrm{d}x, \tag{5.2}$$

where S is a plane of constant y, and $\boldsymbol{j}$ the electrical current density $\nabla\times\boldsymbol{b}$. These fluxes yield mean Coriolis $2Ro^{-1}\Omega_z\mathcal{U}$ and Lorentz forces $b_{0_z}\mathcal{J}$. Since we calculate second-order solutions, we are able to obtain the flux of mass and the current in the fluid interior and compare them with the fluxes through the bumps (figure 5.4, where $\theta = 0$ and a ridge topography are considered following Jault (2020)). First, the Lorentz, Coriolis, and inertial ($(\boldsymbol{u}\cdot\nabla)\boldsymbol{u}$) forces in the interior cancel out. Second, the $(\boldsymbol{u}\cdot\nabla)\boldsymbol{u}$ contribution at the surface exactly balances its contribution in the interior as a consequence of the non-penetration boundary condition and incompressibility. Finally, we find that for an Elsasser number $\Lambda < 1$ the Coriolis force is stronger than the Lorentz force and vice versa for $\Lambda > 1$ (as already shown by Jault, 2020, in section 4.2). In both cases, the force calculated through the bumps predominates. Our order two calculations are required to provide the correct balance of these mean fluxes. The problem at infinity remains but could be solved by relaxing the steadiness assumption (as discussed in long-term perspectives). Physically, these forces tend to oppose the differential velocity between the fluid and the solid. Then, the force feedback on the fluid and solid velocities is something that is missing from current models. Ultimately, we would like to construct a velocity profile knowing the velocity far from the boundary. Similarly, there will be feedback of the electrical field on the ambient magnetic field. The ways of avoiding these limitations are discussed in section 5.3.2.

5.1.3 Turbulence and flow detachment: towards experiments

If our intention was to investigate steep slopes or high Reynolds numbers, our model would not be appropriate due to turbulence and flow separation phenomena that occur downstream of the bumps. We can capture some of the non-linear effects by going to higher orders, but we are still limited by the perturbative approach. Effects that require the perturbation to be of the same order of magnitude as the base flow, such as recirculation, are untractable. DNS allow for this kind of flow but are often far from the desired parameters (e.g. small diffusivities). Despite that there are no experiments of magnetised fluid over a topography, laboratory experiments seem to be an appropriate way of studying the non-linear effects of stratified rotating flows over bumps.

Analogue experiments are underway as part of the project funding this work. One of the aims of these experiments is to use the theoretical results presented in this thesis to predict the surface drag and also disentangle the non-linear effects from the wave drag predicted by the linear theory. We have already started working on the theoretical aspect of turntable experiments, as shown in figure 5.5, which schematically displays the different regimes to be expected in the experiments.

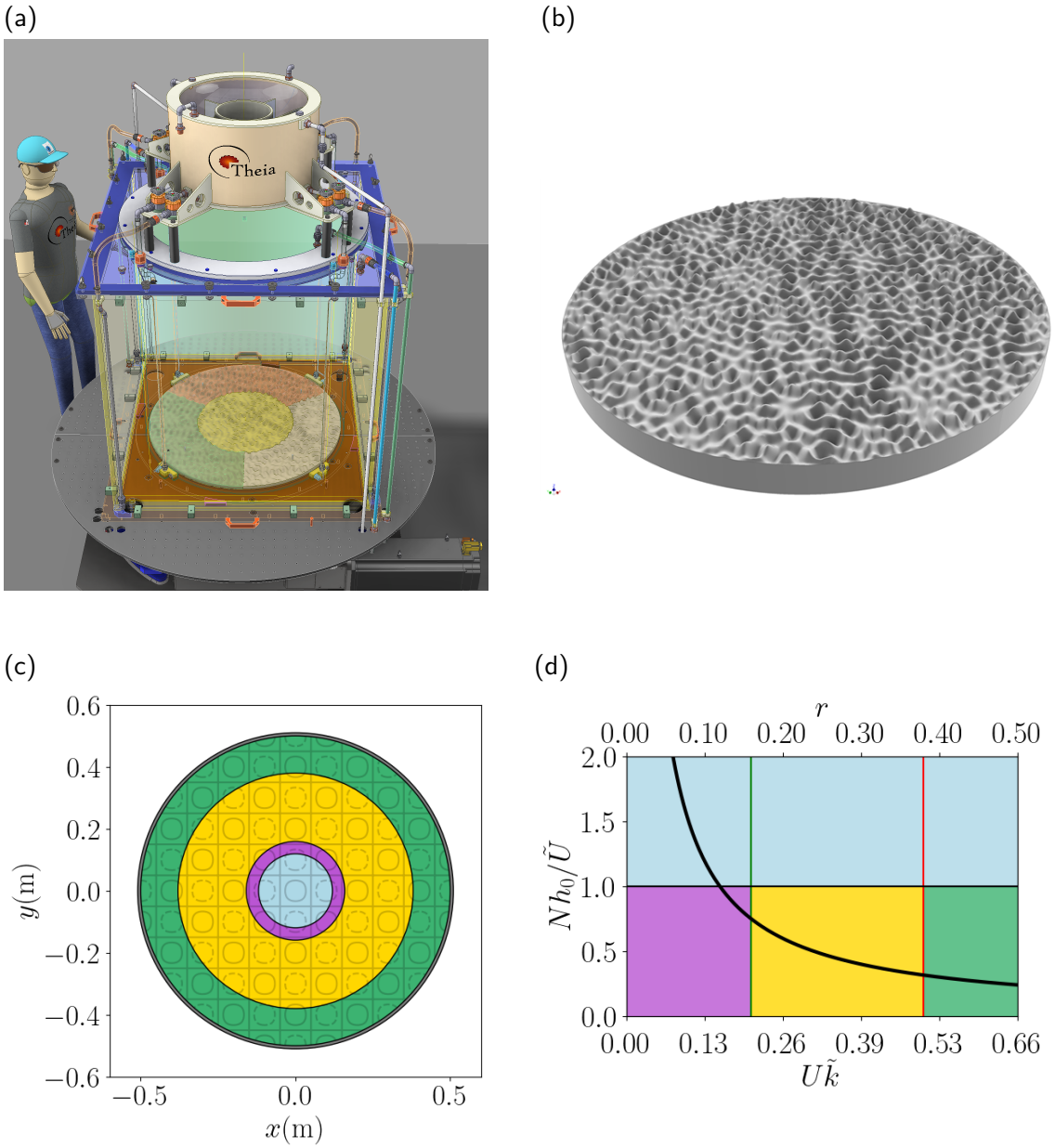

Figure 5.5: **(top)** 3D models of turntable experiments **(a)** and bottom topography of the experiment **(b)**, both from Max Solazzo (private communication). **(bottom)** Schematic of flow behaviour in a rotating cylindrical tank with the bottom covered with an egg box topography of 20 cm wavelength, rotating differentially with the fluid. The blue and green domains correspond to supercritical flows, the pink domain is a geostrophic flow, and the yellow domain corresponds to the propagation of inertial-gravity waves. **(c)** Top view of the experiment, with the colour corresponding to the different regimes. Figure **(d)** gives the Froude number based on the height of the topography $Nh_0/\tilde{U}$ as a function of the intrinsic frequency defined by the Doppler shift of the flow with topography $\tilde{U}\tilde{k}$ (proportional to the tank radius r). This provides the fluid regime. The vertical green line is $\tilde{U}\tilde{k} = 2\Omega_0$ and the red line is $\tilde{U}\tilde{k} = N$. This figure is similar to figure 2 of Legg (2021) (reproduced her in figure 3.14). Parameters: $\Omega_0 = 1$ rpm, $\tilde{U}/r = 0.4$ rpm, $N = 0.5$ s^{-1} and $h_0 = 2 \times 10^{-3}$ m.

5.2 Conclusion

Questions remain about the coupling mechanisms between the core and the mantle that would explain the rotation observations. Notably, the limitations of electromagnetic coupling have motivated the investigations of other coupling mechanisms, such as topographic coupling. Although this topographic coupling has been studied for a long time, there were still some limitations at the beginning of this work to properly model it. This thesis aimed to follow the most advanced theoretical perturbative calculations and adapt it to a semi-analytical method which would allow us to remove many of the approximations made and also to explore weakly non-linear effects as well as global geometry effects. We also wanted our method to be able to handle both hydrodynamics and MHD. One of our initial aims was also to reconcile the topographic coupling models for variation of length of the day and the ones for nutation, which was not the case before.

Thanks to our new method, we have been able to carry out a detailed study of the topographic coupling mechanism, in particular wave drag. We have highlighted the contribution of different types of fluid waves, and in particular Rossby waves, which were absent from previous models. These Rossby waves are relevant for the case of the core-mantle coupling in which we are interested, as they significantly modify the torque. With our higher perturbation order, we have been able to investigate the convergence of this type of local model and have estimated the upper bound of the topography height that can be safely considered and that has sometimes been exceeded in previous studies. Using our model and integrating in latitude, we have compared the results with a CMB topography model. This allowed us to better constrain the parameters required to account for rotation data.

The local models that we use allow for a detailed understanding of the physical processes at play at the boundary. This work is the latest of a long series of models, each of which provides elements of the answer. Our method tried to combine all of these advances and fill in the gaps between the different studies. Today, the missing elements for modelling the CMB coupling correctly are to be found, probably elsewhere than in the local perturbative models. As discussed, the global model makes it possible to take into account the boundary feedback on the bulk flow and thus correctly model the variations of the core angular momentum. Today, advances in local models, notably the semi-analytical method that we developed, allow parameterisations and coupling with global models. A second problem remains, even locally, that is, turbulence effects. The solution to this problem can come from laboratory experiments or numerical simulations.

The topic of CMB coupling, like many geophysical problems, shows the importance of using a variety of methods. However, our approach allowed us to address most of the research questions asked at the beginning. Topographic wave dynamics took up a larger part of the work than expected. This implies that, on the other hand, work is still to be done in terms of comparison with the data and geophysical applications. However, we have today a code ready to be employed, which we plan to use for future studies.

5.3 Long-term perspectives

In light of what we have learnt during this work, several new questions have been raised. The method developed in this thesis potentially allows us to address questions that remain open at the end of this work. Most of them require some extension of the code. In this concluding section, we present some long-term prospective developments in this work.

5.3.1 Increasing the physical complexity of the lowermost mantle

We have already mentioned the 2-layer model in section 5.1.1, but we can also refine the physics of the lowermost solid mantle. The electrical conductivity of the lower mantle may have lateral heterogeneities (Tarits & Mandéa, 2010; Velímský & Knopp, 2021), and can significantly modify the flow and electromagnetic torque at the CMB (Wicht & Jault, 2000; Dumberry & More, 2020), depending on the conductivity distribution. Even if this effect does not seem to be effective for LOD (Wicht & Jault, 2000), one can imagine other applications (*e.g.* nutation). This heterogeneity can be implemented in our code for sinusoidal variations of conductivity in the local frame, which requires slightly modifying the dynamical equations (magnetic diffusivities have to be included in the divergence operator). We can also introduce these variations through the integration of our CMB model with latitude and longitude.

Moreover, some studies proposed that the lowermost mantle is porous to the core flow. This modifies the interaction between the core and the mantle. This mechanism has been proposed to explain the conductivity of the lower mantle (with a potential application to the electromagnetic torque and the LOD changes, Kanda & Stevenson, 2006). This would appear to be an interesting extension of our work. This effect can be introduced into our code by adding a velocity field in the solid driven by the Brinkman (1949) equations[1]. This requires some work, but it can be done in our framework.

5.3.2 Global models and time evolution

As it stands, our code can only consider harmonic time dependencies imposed by the bulk basic flow. One perspective is to remove this limitation. One possible way is to consider the pulsation ω as an unknown of the problem. Letting ω be complex allows us to study the damping of the flow or possible instabilities. Initially, we can leave only the complex parts free and stay periodic, which allows exponential instability. On the other hand, another method to release the constraints on time dependency is to introduce time-stepping in the code. It allows us to integrate the equations over time (with the limitation of having to reach an established regime) and to calculate time variations of the flow.

As shown earlier in section 5.1.2, there are limitations of periodic box models. The pure numerical model can deal with small-scale topography, but this is numerically expensive because of the considerable difference between the large and small scales of the problem. Moreover, these

[1]Brinkman equations are chosen instead of Darcy equations to ease the coupling between the porous solid and the underlying fluid flow.

calculations are almost intractable with magnetic fields, which is one of the main limitations for us. Coupling our local model with numerical dynamo numerical simulations could be a promising solution. One possible approach to move forward consists of coupling a local estimation of the instantaneous stresses at the boundary (knowing $\boldsymbol{u}_0$, $\boldsymbol{b}_0$ and $\boldsymbol{\Omega}_0$ as done in this study) with a numerical model (possibly axially symmetric) in spherical geometry for the time evolution of $\boldsymbol{u}_0$ and $\boldsymbol{b}_0$ as a function of the surface stresses. This is possible but requires either directly coupling the global and local models, or alternatively, an analytic stress parameterisation could be inferred from the local model and used as a stress boundary condition in the DNS.

5.3.3 Thickness of the stratified layer

As stated in the introduction chapter 1, the thickness of the (possible) stratified layer at the top of the core is expected to be of the order of (or less than) a few hundred kilometres. We can consider that the CMB flows given by our local model are incorrect when the perturbations propagate further than the stratified layer.

An analogy can be made with atmospheric studies, which may be relevant for the core stratified layer. In the atmosphere, the change in density profile is a place where waves can break and deposit their momentum. It also creates trapped lee waves, which are waves that remain guided in the stratified part where they were born due to the change of stratification above the layer (Wurtele *et al.*, 1996). Theories have been developed for these waves in the atmosphere and have shown their impact on ground topographic pressure stress (Teixeira, 2014). We propose to do the same in our code by separating the fluid into a stratified layer and a homogeneous (or weakly stratified) layer. Assuming that the perturbation generated by the topography will be of small amplitude at the density change, we can consider at first approximation a non-moving interface with a continuity of velocity and magnetic field. A true free surface condition would actually be more relevant but implies a non-linear relationship between the boundary conditions and the dynamical equations, which is more challenging to implement.

A Appendix

Contents

A.1 Classical boundary layer flows

Here we give the analytical expression boundary layer flows between two flat boundaries that are shown in figure 2.4b. These viscous flows are the Hartmann layer (magnetic field only), the Ekman layer (rotation only), and the Stokes layer (oscillating flow).

For a base flow along the x axis between two horizontal no-slip plates located at $z = -D$ and $z = D$ we can explicitly calculate the resulting boundary layer.

In a non-rotating frame, with a basic state $\boldsymbol{u_0} = \mathbf{1}_x$ and $\boldsymbol{b_0} = Al^{-1}\mathbf{1}_z$ we obtain a Hartmann layer.

$$\boldsymbol{u} = \left(1 - \frac{\cosh zH_a}{\cosh DH_a}\right)\mathbf{1}_x, \tag{A.1}$$

with $H_a = \sqrt{RmRe}/Al$ the Hartmann number.

In a frame rotating at $\boldsymbol{\Omega} = \mathbf{1}_z$ without magnetic field and a base flow $\boldsymbol{u_0} = \mathbf{1}_x$, we obtain an Ekman layer

$$\begin{aligned}\boldsymbol{u} = &\left(1 - \frac{\cos\left(\frac{z(1+\mathrm{i})}{\sqrt{E}}\right)}{2\cos\left(\frac{D(1+\mathrm{i})}{\sqrt{E}}\right)} - \frac{\cosh\left(\frac{z(1+\mathrm{i})}{\sqrt{E}}\right)}{2\cosh\left(\frac{D(1+\mathrm{i})}{\sqrt{E}}\right)}\right)\mathbf{1}_x \\ &+ \mathrm{i}\left(-\frac{\cos\left(\frac{z(1+\mathrm{i})}{\sqrt{E}}\right)}{2\cos\left(\frac{D(1+\mathrm{i})}{\sqrt{E}}\right)} + \frac{\cosh\left(\frac{z(1+\mathrm{i})}{\sqrt{E}}\right)}{2\cosh\left(\frac{D(1+\mathrm{i})}{\sqrt{E}}\right)}\right)\mathbf{1}_y,\end{aligned} \tag{A.2}$$

with the Ekman number $E = Ro/Re$.

With an oscillating basic flow $\boldsymbol{u_0} = \cos(\omega t)\mathbf{1}_x$ and no magnetic field nor rotation, we obtain a Stokes layer

$$\boldsymbol{u} = \Re\left[\left(1 - \frac{\cosh(\sqrt{\mathrm{i}}\lambda z)}{\cosh(\sqrt{\mathrm{i}}D\lambda)}\right)\exp(\mathrm{i}\omega t)\right]\mathbf{1}_x. \tag{A.3}$$

with $\lambda = \sqrt{\omega Re}$ and $\sqrt{\mathrm{i}} = (1+\mathrm{i})/\sqrt{2}$.

A.2 Dispersion relation of MHD waves

Considering an ansatz $\exp(\mathrm{i}(\omega t + k_x x + k_y y + k_z))$, we can write the dispersion relation of diffusionless (and without β-plane), Alfvén, Gravity and Inertial waves (Salhi *et al.*, 2017)

$$\omega_M = (\boldsymbol{b_0}\cdot\boldsymbol{k})Al^{-1}, \tag{A.4}$$

$$\omega_A = k_H k^{-1} Fr^{-1}, \tag{A.5}$$

$$\omega_C = 2(\boldsymbol{\Omega}\cdot\boldsymbol{k})Ro^{-1}k^{-1}, \tag{A.6}$$

$$\tag{A.7}$$

with $\boldsymbol{k}$ the wave vector and $k_H = \sqrt{k_x^2 + k_y^2}$ the horizontal wave number.

We can then write the dispersion relation of Inertia-Gravity waves

$$\omega = \sqrt{\omega_C^2 + \omega_A^2}, \tag{A.8}$$

Magneto Coriolis Waves

$$\left(\omega^2 - \omega_C\omega - \omega_M^2\right)\left(\omega^2 + \omega_C\omega - \omega_M^2\right) = 0, \tag{A.9}$$

and MAC waves

$$\left(\omega^2 - \omega_M^2\right)\left(\omega^2 - \omega_M^2 - \omega_A^2\right) - \omega^2\omega_C^2 = 0. \tag{A.10}$$

A.3 Noteworthy limits of figure 3.1

We presented several equations of limits of figure 3.1. For the sake of clarity and repeatability, we detail their derivations in the following.

A.3.1 Limit in Ro of inertial gravity waves for $Rm/Al^2 \ll 1$

To find the limit

$$Ro > 2\cos\theta, \tag{A.11}$$

we impose a zero determinant for the system of dynamical equations (without a magnetic field and no beta plane), leading to

$$-Rok_x^4 + 4k_x^2 Ro^{-1}\cos^2\theta k_z^2 - k_x^6 - k_x^4 k_y^2 + Fr^{-2}(k_x^4 + k_x^2 k_y^2) = 0, \tag{A.12}$$

which gives the following solution for k_z,

$$k_z = \pm RoFr^{-1}k_H\sqrt{\frac{1-(Frk_x)^2}{(Rok_x)^2-4\cos^2\theta}}, \tag{A.13}$$

whose real part is searched to be non-zero. Assuming $Fr^2k_x^2 < 1$, this leads to

$$Rok_x > 2\cos\theta, \tag{A.14}$$

which does not depend on Fr.

A.3.2 Limit in Ro of inertial gravity waves for $Rm/Al^2 \gg 1$

To find the equation 3.2

$$Al = 2k_HFr^{-1}\cos\theta, \tag{A.15}$$

which delimit the transition between MAC and internal waves, we consider the equations in the limit $Rm^{-1} = 0$ without β-plane. Imposing a zero determinant, and removing the smallest terms (regarding their values in our diagram) we obtain

$$\frac{k_x^2\cos^4\theta}{Al^4}k_z^6 - \frac{2k_x^4\cos^2\theta}{Al^2}k_z^4 + \frac{Al^2Fr^2k_x^6 + k_x^4\cos^2\theta + k_x^2k_y^2\cos^2\theta}{Al^2Fr^2}k_z^2 - \frac{k_x^6+k_x^4k_y^2}{Fr^2} = 0 \tag{A.16}$$

whose complex solutions for k_z are given by

$$k_z = \pm\sqrt{\frac{Al}{2Fr}}\frac{\sqrt{Alfrk_x^2 \pm \sqrt{\Delta}}}{|\cos\theta|}, \tag{A.17}$$

with $\Delta = Al^2Fr^2k_x^4 - 4k_x^2\cos^2\theta - 4k_y^2\cos^2\theta$. The limit is then obtained with $\Delta = 0$.

A.3.3 Rossby waves limits

The two following equations (equations 3.5 and 3.6)

$$8\chi Fr^2\cos\theta\cot\theta < Ro < 2\chi k_H^{-2}\sin\theta, \tag{A.18}$$

$$k_H^2Ro = \chi\sin\theta\left[1 \pm \sqrt{1-(Frk_H)^2[\varpi_1(k_y/\chi)^2 + \varpi_2\cot^2\theta]}\right], \tag{A.19}$$

are respectively derived in the hydrodynamic and ideal MHD limits. Imposing a zero determinant, removing the smallest terms (regarding their values in our figure) and prescribing the k_z values from figure 3.5b ($k_z = -k_y\tan\theta$ for the hydrodynamic and $k_z = k_y\tan\theta/2$ for the ideal MHD limits, respectively), we obtain

$$(k_H^2 - A^2Fr^2)Ro^2 + 2\sin\theta(BFr^2-1)\chi Ro + CFr^2\chi^2 = 0, \tag{A.20}$$

for the hydrodynamic limit, with

$$A^2 = (k_H^2-k_y^2)^2 + \frac{(k_Hk_y)^2 - k_y^4}{\cos^2\theta}, \tag{A.21}$$

$$B = k_H^2 + 2k_y^2 + \frac{k_y^2}{\cos^2\theta}, \tag{A.22}$$

$$C = 16\cos^2\theta. \tag{A.23}$$

Equation A.18 is obtained for $Fr \ll 1$.

For the ideal MHD limit, we obtain the matrix

$$\begin{bmatrix} \frac{k_x(-Rok_y \tan\theta+4i\sin\theta)}{2Ro} & -\frac{4\chi\cos\theta+ik_y\sin\theta}{Ro} & k_x^2+\frac{ik_y\sin\theta\tan\theta}{Ro} & -\frac{ik_x}{Fr^2} & 0 & 0 & 0 \\ \frac{k_x(Rok_y+2i\cos\theta)}{Ro} & \frac{-Rok_x^2+2\chi\sin\theta+2ik_y\cos\theta}{Ro} & \frac{4\chi\cos\theta-2ik_y\sin\theta}{Ro} & 0 & 0 & 0 & 0 \\ ik_x & ik_y & \frac{ik_y\tan\theta}{2} & 0 & 0 & 0 & 0 \\ 0 & 0 & -1 & ik_x & 0 & 0 & 0 \\ 0 & 0 & 0 & 0 & ik_x & ik_y & \frac{ik_y\tan\theta}{2} \\ 0 & 0 & 0 & 0 & 0 & ik_x & 0 \\ 0 & 0 & 0 & 0 & 0 & 0 & ik_x \end{bmatrix} \tag{A.24}$$

Equation A.19 can be obtained by cancelling the determinant in the limit $Fr, Ro \ll 1$. Note that this matrix is given for non-traditional β-plane and is modified for other approximations.

A.4 Supplementary material for chapter 4

In this section we give some figures on which the assertions made in chapter 4 are based but which had no place in the body of the text.

In section 4.2 we argue that the dissipation scales as $\omega^{1/2}$ in figure 4.3 when $\omega \gg 1$ because the vertical wave number k_z has the same scaling. In figure A.1 we show the variation of k_z with the base flow oscillation frequency. The figure A.2 shows the equivalent of figure 4.4 at different

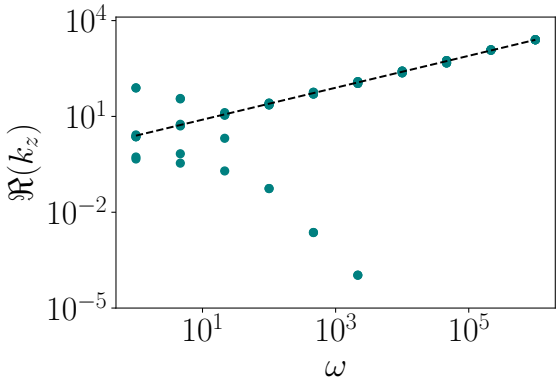

Figure A.1: Real part of the vertical wave numbers as a function of the oscillation frequency of the base flow ω. The dashed line indicates the $\sqrt{\omega}$ scaling. The parameters are the same as in figure 4.3b.

solid conductivity ($\sigma_s = 0.1$ S m^{-1} and $\sigma_s = 10$ S m^{-1}) for a diurnal oscillation. This confirms the strong influence of solid conductivity. The figure A.3 shows the equivalent of figure 4.6 with an insulating mantle. This shows the respective influence of stratification and mantle conductivity.

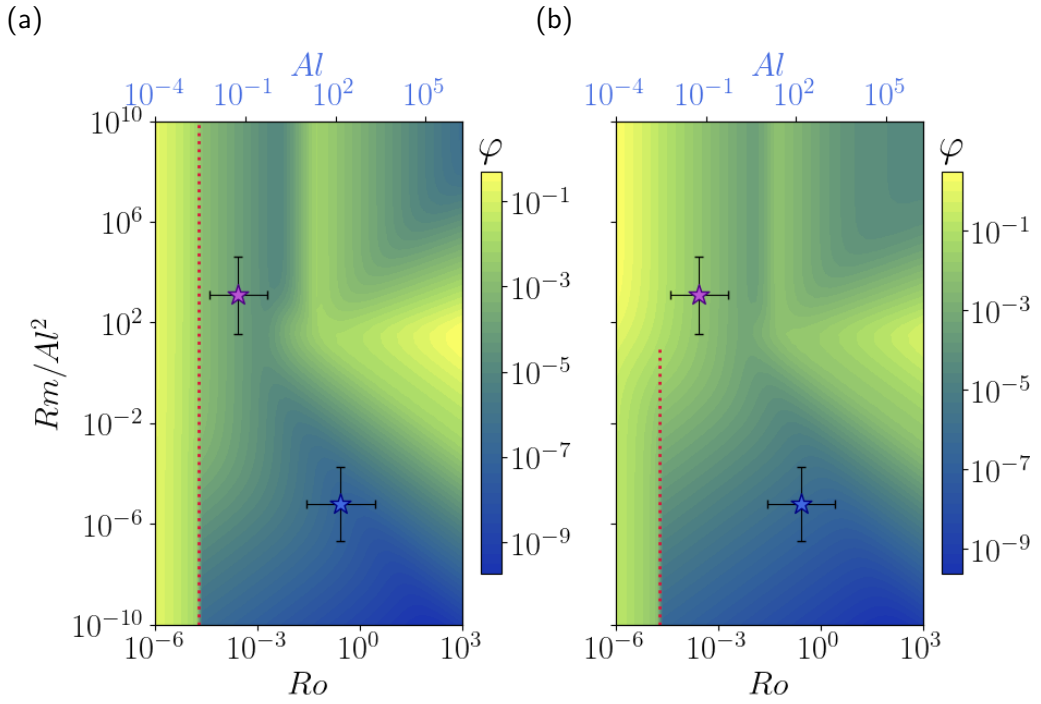

Figure A.2: Dissipation (colours) as a function of the interaction parameter Rm/Al^2 and Ro at $\theta = \pi/4$ for a conducting solid at constant $\sigma_s = 0.1$ S/m **(a)** and $\sigma_s = 10$ S/m **(b)**. The topography has an eggbox shape with $\epsilon_t = 10^{-3}$, the base magnetic field is dipolar, and the rotation vector is that of equation 2.7 (traditional tilted β-plane). The base flow is the equation 2.29 with $\omega = 1/Ro$ (diurnal oscillation). Dissipation is shown for $\chi = 0.0287$, that is, $\tilde{k}^{-1} = 100$ km for the core and $\tilde{k}^{-1} = 183$ km for the ocean. The stars represent the Earth's core (purple) and the ocean (blue). The red line is equation 4.3. Other parameters are those of table 2.2 at $\tilde{k}^{-1} = 100$ km.

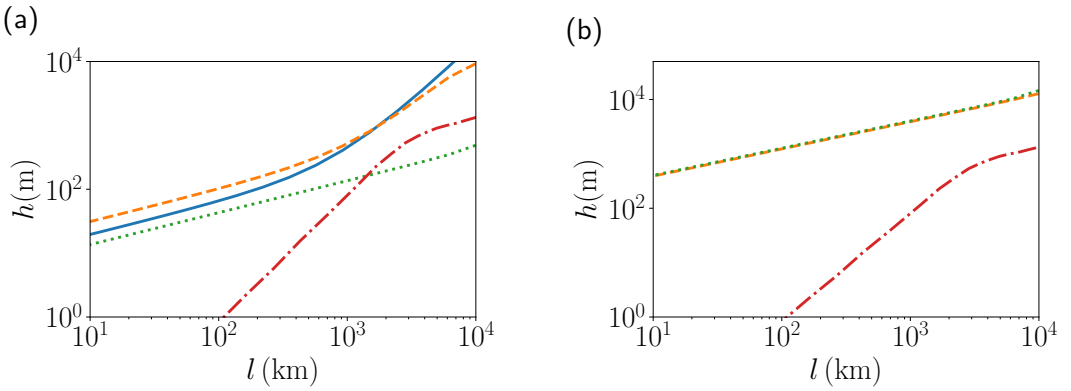

Figure A.3: Topography height that is needed to explain the out-of-phase component of the annual nutation (calculated via Ohmic dissipation). Surface dissipation is calculated at $\theta = 0$ (solid blue), $\theta = \pi/4$ (dashed orange), and $\theta = \pi/2$ (dotted green). This surface dissipation is then multiplied by the surface of the CMB. The red dashed-dotted line is the CMB topography model of figure 3.12a. The solid is insulating and the other parameters are those of figure 4.6.

Bibliography

Acheson, 1975, On Hydromagnetic Oscillations within the Earth and Core–Mantle Coupling. *Geophys. J. Int.* **43** (1), 253–268. [13, 22, 26].

Aguilar & Sutherland, 2006, Internal wave generation from rough topography. *Physics of Fluids* **18** (6). [21].

Aguilar, Sutherland, & Muraki, 2006, Laboratory generation of internal waves from sinusoidal topography. *Deep Sea Research Part II: Topical Studies in Oceanography* **53** (1-2), 96–115. [21].

An & Ding, 2022, Revisiting the period and quality factor of the Chandler wobble and its possible geomagnetic jerk excitation. *Geodesy and Geodynamics* **13** (5), 427–434. [9].

Arnould, Coltice, Flament, & Mallard, 2020, Plate tectonics and mantle controls on plume dynamics. *Earth and Planetary Science Letters* **547**, 116439. [15].

Athanassiadou, 2003, Wave and form drag: Their relation in the linear gravity wave regime. *Tellus A: Dynamic Meteorology and Oceanography* **55** (2), 173–180. [52, 58].

Baines, 2022, *Topographic Effects in Stratified Flows*, , vol. 22. Cambridge university press. [20, 21].

Baines, Boyer, & Xie, 2005, Laboratory simulations of coastally trapped waves with rotation, topography and stratification. *Dynamics of atmospheres and oceans* **39** (3-4), 153–173. [22].

Baines & Hoinka, 1985, Stratified flow over two-dimensional topography in fluid of infinite depth: A laboratory simulation. *Journal of atmospheric sciences* **42** (15), 1614–1630. [21].

Bardsley, 2018, Could hydrodynamic Rossby waves explain the westward drift? *Proc. R. Soc. A.* **474** (2213), 20180119. [30].

Barrois, Gastine, & Finlay, 2022, Comparison of quasi-geostrophic, hybrid and 3-D models of planetary core convection. *Geophysical Journal International* **231** (1), 129–158. [30].

Bell, 1975, Lee waves in stratified flows with simple harmonic time dependence. *Journal of Fluid Mechanics* **67** (4), 705–722. [20, 52].

Bell Jr., 1975, Topographically generated internal waves in the open ocean. *Journal of Geophysical Research (1896-1977)* **80** (3), 320–327. [52].

Berkowitz, 1984, On computing the determinant in small parallel time using a small number of processors. *Information Processing Letters* **18** (3), 147–150. [38].

Bizouard, Lambert, Gattano, Becker, & Richard, 2019, The IERS EOP 14C04 solution for Earth orientation parameters consistent with ITRF 2014. *J Geod* **93** (5), 621–633. [9].

Bouffard, Landeau, & Goument, 2020, Convective Erosion of a Primordial Stratification Atop Earth's Core. *Geophysical Research Letters* **47** (14), e2020GL087109. [13].

Boyd, 2018, *Dynamics of the Equatorial Ocean*. Berlin, Heidelberg: Springer Berlin Heidelberg. [31].

Boyer, 1987, Stratified rotating flow over and around isolated three-dimensional topography. *Phil. Trans. R. Soc. Lond. A* **322** (1564), 213–241. [21].

Boyer & Biolley, 1986, Linearly stratified, rotating flow over long ridges in a channel. *Phil. Trans. R. Soc. Lond. A* **318** (1544), 411–438. [21].

Boyer & Davies, 2000, Laboratory Studies of Orographic Effects in Rotating and Stratified Flows. *Annu. Rev. Fluid Mech.* **32** (1), 165–202. [21, 22].

Boyer & Zhang, 1989, The interaction of time-dependent rotating and stratified flow with isolated topography. *Dynamics of atmospheres and oceans* **14**, 543–575. [21].

Braginsky, 1998, Magnetic Rossby waves in the stratified ocean of the core, and topographic core-mantle coupling. *Earth Planets Space* **50** (8), 641–649. [13, 22, 37, 43, 55, 58].

Bretagnon, Rocher, & Simon, 1997, Theory of the rotation of the rigid Earth. *Astronomy and Astrophysics, v. 319, p. 305-317* **319**, 305–317. [9].

Brinkman, 1949, A calculation of the viscous force exerted by a flowing fluid on a dense swarm of particles. *Appl. Sci. Res.* **1** (1), 27. [82].

Buffett, 2014, Geomagnetic fluctuations reveal stable stratification at the top of the Earth's core. *Nat* **507** (7493), 484–487. [13, 72].

Buffett, Knezek, & Holme, 2016, Evidence for MAC waves at the top of Earth's core and implications for variations in length of day. *Geophysical Journal International* **204** (3), 1789–1800. [13].

Buffett, 1992, Constraints on magnetic energy and mantle conductivity from the forced nutations of the Earth. *Journal of Geophysical Research: Solid Earth* **97** (B13), 19581–19597. [13, 14, 22, 65].

Buffett, 1996, Gravitational oscillations in the length of day. *Geophys. Res. Lett.* **23** (17), 2279–2282. [12, 18, 22].

Buffett, 2010, Chemical stratification at the top of Earth›s core: Constraints from observations of nutations. *Earth Planet. Sc. Lett.* **296** (3-4), 367–372. [9, 13, 14, 17, 18, 22, 28, 34, 35, 36, 41, 43, 65, 66, 70, 71, 72, 75, 76].

Buffett, 2021, Conditions for turbulent Ekman layers in precessionally driven flow. *Geophys. J. Int.* **226** (1), 56–65. [36, 71].

Buffett & Christensen, 2007, Magnetic and viscous coupling at the core—mantle boundary: Inferences from observations of the Earth's nutations. *Geophysical Journal International* **171** (1), 145–152. [13].

Buffett, Mathews, & Herring, 2002, Modeling of nutation and precession: Effects of electromagnetic coupling. *Journal of Geophysical Research: Solid Earth* **107** (B4), ETG–5. [16].

Burmann & Noir, 2018, Effects of bottom topography on the spin-up in a cylinder. *Phys. Fluids* **30** (10), 106601. [21].

Carnevale, Kloosterziel, & Van Heijst, 1991, Propagation of barotropic vortices over topography in a rotating tank. *Journal of Fluid Mechanics* **233**, 119–139. [21].

Chan & Chin, 2023, Turbulent boundary layer flow over a three-dimensional sinusoidal surface. *Journal of Fluid Mechanics* **975**, A19. [21].

Chao & Hsieh, 2015, The Earth's free core nutation: Formulation of dynamics and estimation of eigenperiod from the very-long-baseline interferometry data. *Earth and Planetary Science Letters* **432**, 483–492. [11].

Coltice, Husson, Faccenna, & Arnould, 2019, What drives tectonic plates? *Science Advances* **5** (10), eaax4295. [14, 15].

COMSOL, 1998, Introduction to COMSOL multiphysics®. *COMSOL Multiphysics, Burlington, MA, accessed Feb* **9** (2018), 32. [64].

Correia, 2006, The core–mantle friction effect on the secular spin evolution of terrestrial planets. *Earth and Planetary Science Letters* **252** (3-4), 398–412. [17].

Cushman-Roisin & Beckers, 2011, *Introduction to Geophysical Fluid Dynamics: Physical and Numerical Aspects*. Academic press. [20, 29, 31].

Davidson & Belova, 2002, An Introduction to Magnetohydrodynamics. *American Journal of Physics* **70** (7), 781. [39].

Davies, Stegman, & Dumberry, 2014, The strength of gravitational core-mantle coupling. *Geophys. Res. Lett.* **41** (11), 3786–3792. [12, 15].

Dehant, 1987, Integration of the gravitational motion equations for an elliptical uniformly rotating Earth with an inelastic mantle. *Physics of the earth and planetary interiors* **49** (3-4), 242–258. [17].

Dehant, Campuzano, De Santis, & van Westrenen, 2022, Structure, Materials and Processes in the Earth's Core and Mantle. *Surv Geophys* **43** (1), 263–302. [15].

Dehant, Hinderer, Legros, & Lefftz, 1993, Analytical approach to the computation of the Earth, the outer core and the inner core rotational motions. *Physics of the earth and planetary interiors* **76** (3-4), 259–282. [16].

Dehant & Mathews, 2015, *Precession, Nutation and Wobble of the Earth*. Cambridge University Press. [9].

Deleplace & Cardin, 2006, Viscomagnetic torque at the core mantle boundary. *Geophys. J. Int.* **167** (2), 557–566. [13, 22].

Dellar, 2011, Variations on a beta-plane: Derivation of non-traditional beta-plane equations from Hamilton's principle on a sphere. *J. Fluid Mech.* **674**, 174–195. [30, 37, 43, 60].

Delplace & Venaille, 2019, De la topologie dans les ondes équatoriales. *La gazette des mathématiciens* **161**. [31].

Dormy & Soward, 2007, *Mathematical Aspects of Natural Dynamos*. CRC Press. [39].

Dumberry, 2009, Influence of elastic deformations on the inner core wobble. *Geophysical Journal International* **178** (1), 57–64. [16].

Dumberry & More, 2020, Weak magnetic field changes over the Pacific due to high conductance in lowermost mantle. *Nature Geoscience* **13** (7), 516–520. [82].

Ermakov, Park, & Bills, 2018, Power Laws of Topography and Gravity Spectra of the Solar System Bodies. *JGR Planets* **123** (8), 2038–2064. [15].

Ertel, 1942, Ein neuer hydrofynamischer Wirbelsatz. *Meteor.Z.* **59**, 277–282. [29].

Ferrándiz, Gross, Escapa, Getino, Brzeziński, & Heinkelmann, 2022, Report of the IAU/IAG Joint Working Group on Theory of Earth Rotation and Validation. In *Beyond 100: The Next Century in Geodesy* (ed. Jeffrey T. Freymueller & Laura Sánchez), *International Association of Geodesy Symposia*, vol. 1, pp. 99–106. Cham: Springer International Publishing. [16].

Ferrándiz, Navarro, Martínez-Belda, Escapa, & Getino, 2018, Limitations of the IAU2000 nutation model accuracy due to the lack of Oppolzer terms of planetary origin. *A&A* **618**, A69. [16].

Finlay, 2008, Course 8 Waves in the presence of magnetic fields, rotation and convection. pp. 403–450. Elsevier. [58].

Finlay, Gillet, Aubert, Livermore, & Jault, 2023, Gyres, jets and waves in the Earth's core. *Nature Reviews Earth & Environment* pp. 1–16. [18, 19].

Friis-Christensen, Lühr, Knudsen, & Haagmans, 2008, Swarm – An Earth Observation Mission investigating Geospace. *Advances in Space Research* **41** (1), 210–216. [11].

Garcia & Souriau, 2000, Amplitude of the core–mantle boundary topography estimated by stochastic analysis of core phases. *Phys. Earth Planet. In.* **117** (1-4), 345–359. [15].

Gastine, 2019, Pizza: An open-source pseudo-spectral code for spherical quasi-geostrophic convection. *Geophysical Journal International* **217** (3), 1558–1576. [30].

Gastine, Aubert, & Fournier, 2020, Dynamo-based limit to the extent of a stable layer atop Earth's core. *Geophysical Journal International* **222** (2), 1433–1448. [13].

Gérard-Varet, 2003*a*, Convergence of the rotating fluids system in a domain with rough boundaries. *Journées équations aux dérivées partielles* pp. 1–15. [20].

Gérard-Varet, 2003*b*, Highly rotating fluids in rough domains. *Journal de Mathématiques Pures et Appliquées* **82** (11), 1453–1498. [20].

Gérard-Varet & Dormy, 2006, Ekman layers near wavy boundaries. *Journal of Fluid Mechanics* **565**, 115–134. [20].

Gerick, Jault, Noir, & Vidal, 2020, Pressure torque of torsional Alfvén modes acting on an ellipsoidal mantle. *Geophys. J. Int.* **222** (1), 338–351. [30, 57].

Gill, 1982, *Atmosphere-Ocean Dynamics*, , vol. 30. Academic press. [20, 52].

Gillet, Gerick, Jault, Schwaiger, Aubert, & Istas, 2022, Satellite magnetic data reveal interannual waves in Earth's core. *Proc. Natl. Acad. Sci.* **119** (13), e2115258119. [11].

Gillet, Jault, & Finlay, 2015, Planetary gyre, time-dependent eddies, torsional waves, and equatorial jets at the Earth's core surface. *JGR Solid Earth* **120** (6), 3991–4013. [11, 22, 75].

Gillet & Jones, 2006, The quasi-geostrophic model for rapidly rotating spherical convection outside the tangent cylinder. *Journal of Fluid Mechanics* **554**, 343–369. [30].

Glane, 2021, Variations in the length of day of the earth due to topographic core-mantle coupling in a stratified layer. PhD thesis, Technische Universitaet Berlin (Germany). [43].

Glane & Buffett, 2018, Enhanced Core-Mantle Coupling Due to Stratification at the Top of the Core. *Front. Earth Sci.* **6**. [13, 22, 28, 34, 37, 41, 43, 58, 59].

Golub & Reinsch, 1971, Singular Value Decomposition and Least Squares Solutions. pp. 134–151. Berlin, Heidelberg: Springer Berlin Heidelberg. [38].

Grimshaw, 1975, A note on the β-plane approximation. *Tellus* **27** (4), 351–357. [30].

Gross, Fukumori, Menemenlis, & Gegout, 2004, Atmospheric and oceanic excitation of length-of-day variations during 1980–2000. *J. Geophys. Res.* **109** (B1), 2003JB002432. [18].

Gunell, Maggiolo, Nilsson, Wieser, Slapak, Lindkvist, Hamrin, & De Keyser, 2018, Why an intrinsic magnetic field does not protect a planet against atmospheric escape. *Astronomy & Astrophysics* **614**, L3. [8].

Guo & Shen, 2020, Formulation of a Triaxial Three-Layered Earth Rotation: Theory and Rotational Normal Mode Solutions. *Journal of Geophysical Research: Solid Earth* **125** (3), e2019JB018571. [16].

Gwinn, Herring, & Shapiro, 1986, Geodesy by radio interferometry: Studies of the forced nutations of the Earth: 2. Interpretation. *Journal of Geophysical Research: Solid Earth* **91** (B5), 4755–4765. [17].

Hardy & Wong, 2019, Stably stratified layers within Earth's core. *Astronomy & Geophysics* **60** (3), 3–30. [13].

Harlander, 2005, A high-latitude quasi-geostrophic delta plane model derived from spherical geometry. *Tellus A: Dynamic Meteorology and Oceanography* **57** (1), 43–54. [31].

Hassan & Eltayeb, 1982, On the topographic coupling at the core-mantle interface. *Physics of the Earth and Planetary Interiors* **28** (1), 14–26. [22].

Helffrich & Kaneshima, 2010, Outer-core compositional stratification from observed core wave speed profiles. *Nat* **468** (7325), 807–810. [13].

Herring, Gwinn, & Shapiro, 1986, Geodesy by radio interferometry: Studies of the forced nutations of the Earth: 1. Data analysis. *Journal of Geophysical Research: Solid Earth* **91** (B5), 4745–4754. [17].

Hide, 1969, Interaction between the Earth's liquid core and solid mantle. *Nat* **222** (5198), 1055–1056. [13].

Hide, 1989, Fluctuations in the Earth's rotation and the topography of the core-mantle interface. *Philosophical transactions of the Royal Society of London. Series A: Mathematical and physical sciences* **328** (1599), 351–363. [22].

Hirose, Labrosse, & Hernlund, 2013, Composition and State of the Core. *Annu. Rev. Earth Planet. Sci.* **41** (1), 657–691. [13].

Holme, 1998, Electromagnetic core—mantle coupling—I. Explaining decadal changes in the length of day. *Geophysical journal international* **132** (1), 167–180. [13, 14, 22, 65].

Holme & De Viron, 2013, Characterization and implications of intradecadal variations in length of day. *Nature* **499** (7457), 202–204. [18].

Huang, Dehant, Liao, Van Hoolst, & Rochester, 2011, On the coupling between magnetic field and nutation in a numerical integration approach. *J. Geophys. Res.* **116** (B3), B03403. [17].

Huang, Jin, & Liao, 2001, A new nutation model of a non-rigid earth with ocean and atmosphere. *Geophysical Journal International* **146** (1), 126–133. [17].

Iess, Rappaport, Jacobson, Racioppa, Stevenson, Tortora, Armstrong, & Asmar, 2010, Gravity Field, Shape, and Moment of Inertia of Titan. *Science* **327** (5971), 1367–1369. [20].

Irving, Cottaar, & Lekić, 2018, Seismically determined elastic parameters for Earth's outer core. *Sci. Adv.* **4** (6), eaar2538. [13].

Jackson & Fox, 1999, Classical Electrodynamics, 3rd ed. *Am. J. Phys.* **67** (9), 841–842. [39].

Jault, 2015, Illuminating the electrical conductivity of the lowermost mantle from below. *Geophysical Journal International* **202** (1), 482–496. [11, 13, 14, 65].

Jault, 2020, Tangential stress at the core–mantle interface. *Geophys. J. Int.* **221** (2), 951–967. [13, 22, 28, 34, 35, 37, 41, 42, 43, 58, 75, 76, 78].

Jault & Finlay, 2015, Waves in the core and mechanical core-mantle interactions. pp. 225–245. Elsevier. [12].

Jault, Gire, & Le Mouël, 1988, Westward drift, core motions and exchanges of angular momentum between core and mantle. *Nat* **333** (6171), 353–356. [12, 18].

Jault & Le Mouël, 1990, Core-mantle boundary shape: Constraints inferred from the pressure torque acting between the core and the mantle. *Geophysical Journal International* **101** (1), 233–241. [22].

Jault & Mouël, 1989, The topographic torque associated with a tangentially geostrophic motion at the core surface and inferences on the flow inside the core. *Geophysical & Astrophysical Fluid Dynamics* **48** (4), 273–295. [13].

Jeffreys & Vicente, 1957, The theory of nutation and the variation of latitude. *Monthly Notices of the Royal Astronomical Society* **117** (2), 142–161. [16].

Kanda & Stevenson, 2006, Suction mechanism for iron entrainment into the lower mantle. *Geophysical Research Letters* **33** (2), 2005GL025009. [82].

Kaneshima, 2018, Array analyses of SmKS waves and the stratification of Earth's outermost core. *Physics of the Earth and Planetary Interiors* **276**, 234–246. [13].

Kerner, 1966, Ein gesamtschrittverfahren zur berechnung der nullstellen von polynomen. *Numerische Mathematik* **8** (3), 290–294. [38].

Kihoulou, Čadek, Kvorka, Kalousová, Choblet, & Tobie, 2023, Topographic response to ocean heat flux anomaly on the icy moons of Jupiter and Saturn. *Icarus* **391**, 115337. [20, 73].

Koelemeijer, 2021, Toward Consistent Seismological Models of the Core–Mantle Boundary Landscape. chap. 9, pp. 229–255. American Geophysical Union (AGU). [14, 15].

Koot, 2009, Etude de la structure interne de la Terre à partir des observations de la précession et des nutations. PhD thesis. [17].

Koot, Dumberry, Rivoldini, De Viron, & Dehant, 2010, Constraints on the coupling at the core–mantle and inner core boundaries inferred from nutation observations. *Geophys. J. Int.* **182** (3), 1279–1294. [9, 75].

Koot, Rivoldini, De Viron, & Dehant, 2008, Estimation of Earth interior parameters from a Bayesian inversion of very long baseline interferometry nutation time series. *Journal of Geophysical Research: Solid Earth* **113** (B8). [16].

Kuang & Bloxham, 1993, On the effect of boundary topography on flow in the Earth's core. *Geophysical & Astrophysical Fluid Dynamics* **72** (1-4), 161–195. [22].

Kuang & Chao, 2001, Topographic core-mantle coupling in geodynamo modeling. *Geophysical Research Letters* **28** (9), 1871–1874. [13].

Kvorka & Čadek, 2024, The role of subsurface ocean dynamics and phase transitions in forming the topography of icy moons. *Icarus* **412**, 115985. [20].

Kvorka, Čadek, Tobie, & Choblet, 2018, Does Titan's long-wavelength topography contain information about subsurface ocean dynamics? *Icarus* **310**, 149–164. [73].

Labbé, Jault, & Gillet, 2015, On magnetostrophic inertia-less waves in quasi-geostrophic models of planetary cores. *Geophysical & Astrophysical Fluid Dynamics* **109** (6), 587–610. [30].

Landeau, Olson, Deguen, & Hirsh, 2016, Core merging and stratification following giant impact. *Nature Geoscience* **9** (10), 786–789. [13].

Lau, Mitrovica, Davis, Tromp, Yang, & Al-Attar, 2017, Tidal tomography constrains Earth's deep-mantle buoyancy. *Nature* **551** (7680), 321–326. [12].

Legg, 2021, Mixing by oceanic lee waves. *Annu. Rev. Fluid Mech.* **53**, 173–201. [20, 52, 58, 62, 80].

Legros, Hinderer, Lefftz, & Dehant, 1993, The influence of the solid inner core on gravity changes and spatial nutations induced by luni-solar tides and surface loading. *Physics of the earth and planetary interiors* **76** (3-4), 283–315. [16].

Lemasquerier, 2021, Experimental and numerical study of Jupiter's dynamics: Jets, vortices and zonostrophic turbulence. PhD thesis, Aix-Marseille Université. [21].

Lemasquerier, Favier, & Bars, 2021, Zonal jets at the laboratory scale: Hysteresis and Rossby waves resonance. *Journal of Fluid Mechanics* **910**, A18. [31].

Liouville, 1858, Développements sur un chapitre de la Mécanique de Poisson. *Journal de Mathematiques pures et Appliquees* **3**, 1–25. [16].

Liu, Lambert, Zhu, & Liu, 2020, Systematics and accuracy of VLBI astrometry: A comparison with Gaia Data Release 2. *Astronomy & Astrophysics* **634**, A28. [9].

Long, 1955, Some Aspects of the Flow of Stratified Fluids. *Tellus* **7** (3), 341–357. [21].

Longuet-Higgins, 1964, Planetary waves on a rotating sphere. *Proceedings of the Royal Society of London. Series A. Mathematical and Physical Sciences* **279** (1379), 446–473. [30].

Lowes, 1974, Spatial power spectrum of the main geomagnetic field, and extrapolation to the core. *Geophysical Journal International* **36** (3), 717–730. [13].

Lundin, Lammer, & Ribas, 2007, Planetary Magnetic Fields and Solar Forcing: Implications for Atmospheric Evolution. *Space Sci Rev* **129** (1-3), 245–278. [8].

Mandea, Gibert, Le Mouël, Hulot, & Saracco, 1999, An estimate of average lower mantle conductivity by wavelet analysis of geomagnetic jerks. *J. Geophys. Res.* **104** (B8), 17735–17745. [13].

Mathews, Herring, & Buffett, 2002, Modeling of nutation and precession: New nutation series for nonrigid Earth and insights into the Earth's interior. *Journal of Geophysical Research: Solid Earth* **107** (B4), ETG–3. [11, 16, 17, 75].

Mathews, Buffett, Herring, & Shapiro, 1991, Forced nutations of the Earth: Influence of inner core dynamics: 1. Theory. *Journal of Geophysical Research: Solid Earth* **96** (B5), 8219–8242. [16].

Maxworthy, 1977, Topographic effects in rapidly-rotating fluids: Flow over a transverse ridge. *Journal of Applied Mathematics and Physics (ZAMP)* **28** (5), 853–864. [21].

Maxworthy & Browand, 1975, Experiments in Rotating and Stratified Flows: Oceanographic Application. *Annu. Rev. Fluid Mech.* **7** (1), 273–305. [22].

Mayer & Fringer, 2020, Improving Nonlinear and Nonhydrostatic Ocean Lee Wave Drag Parameterizations. *Journal of Physical Oceanography* **50** (9), 2417–2435. [20].

Meurer et al., 2017, SymPy: Symbolic computing in Python. *PeerJ Comput. Sci.* **3**, e103. [39].

Mineev & Funtikov, 2004, Viscosity measurements on metal melts at high pressure and viscosity calculations for the earth's core. *Physics-Uspekhi* **47** (7), 671. [12].

Moffatt, 1977, Topographic coupling at the core-mantle interface. *Geophysical & Astrophysical Fluid Dynamics* **9** (1), 279–288. [13, 22, 28].

Molodensky, 1961, The theory of nutation and diurnal Earth tides. *Commun. Observ. Roy. Belg.* **188**, 25–56. [16, 17].

Narteau, Le Mouël, Poirier, Sepúlveda, & Shnirman, 2001, On a small-scale roughness of the core–mantle boundary. *Earth and Planetary Science Letters* **191** (1), 49–60. [14].

Nikurashin & Ferrari, 2010*a*, Radiation and Dissipation of Internal Waves Generated by Geostrophic Motions Impinging on Small-Scale Topography: Application to the Southern Ocean. *Journal of Physical Oceanography* **40** (9), 2025–2042. [21].

Nikurashin & Ferrari, 2010*b*, Radiation and Dissipation of Internal Waves Generated by Geostrophic Motions Impinging on Small-Scale Topography: Theory. *Journal of Physical Oceanography* **40** (5), 1055–1074. [20, 52].

Nimmo & Bills, 2010, Shell thickness variations and the long-wavelength topography of Titan. *Icarus* **208** (2), 896–904. [20].

Nimmo & Pappalardo, 2016, Ocean worlds in the outer solar system. *JGR Planets* **121** (8), 1378–1399. [20].

Noir & Cébron, 2013, Precession-driven flows in non-axisymmetric ellipsoids. *Journal of Fluid Mechanics* **737**, 412–439. [10].

Olson, Landeau, & Reynolds, 2018, Outer core stratification from the high latitude structure of the geomagnetic field. *Frontiers in Earth Science* **6**, 140. [13].

Pais & Jault, 2008, Quasi-geostrophic flows responsible for the secular variation of the Earth's magnetic field. *Geophysical Journal International* **173** (2), 421–443. [11].

Pais & Le Mouel, 2001, Precession-induced flows in liquid-filled containers and in the Earth/s core. *Geophys. J. Int.* **144** (3), 539–554. [71].

Palmer, Shutts, & Swinbank, 1986, Alleviation of a systematic westerly bias in general circulation and numerical weather prediction models through an orographic gravity wave drag parametrization. *Q. J. R. Meteorolog. Soc.* **112** (474), 1001–1039. [20].

Pedlosky, 2003, *Waves in the Ocean and Atmosphere*. Berlin, Heidelberg: Springer Berlin Heidelberg. [31].

Pedlosky, 2013, *Geophysical Fluid Dynamics*. Springer Science & Business Media. [29].

Pedlosky & Greenspan, 1967, A simple laboratory model for the oceanic circulation. *Journal of Fluid Mechanics* **27** (2), 291–304. [21].

Pfeffer, Cazenave, Rosat, Moreira, Mandea, Dehant, & Coupry, 2023, A 6-year cycle in the Earth system. *Global and Planetary Change* **229**, 104245. [18, 19].

Pfeffer, Kung, Ding, & Li, 1993, Barotropic flow over bottom topography—experiments and nonlinear theory. *Dynamics of atmospheres and oceans* **19** (1-4), 101–114. [21].

Pichon, Aubert, & Fournier, 2016, Coupled dynamics of Earth's geomagnetic westward drift and inner core super-rotation. *Earth and Planetary Science Letters* **437**, 114–126. [22].

Pratte & Hart, 1991, Experiments on periodically forced flow over topography in a rotating fluid. *Journal of Fluid Mechanics* **229**, 87–114. [21].

Puica, Dehant, Folgueira, Van Hoolst, & Rekier, 2023, Analytical computation of total topographic torque at the core–mantle boundary and its impact on tidally driven length-of-day variations. *Geophys. J. Int.* **234** (1), 585–596. [15, 18].

Radko, 2023*a*, A generalized theory of flow forcing by rough topography. *Journal of Fluid Mechanics* **961**, A24. [21].

Radko, 2023*b*, The sandpaper theory of flow–topography interaction for homogeneous shallow-water systems. *Journal of Fluid Mechanics* **977**, A9. [21].

Rekier, Triana, Trinh, & Buffett, 2023, Electric interface condition for sliding and viscous contacts. *Phys. Rev. Res.* **5** (3), 033029. [33].

Rexer & Hirt, 2015, Ultra-high-Degree Surface Spherical Harmonic Analysis Using the Gauss–Legendre and the Driscoll/Healy Quadrature Theorem and Application to Planetary Topography Models of Earth, Mars and Moon. *Surv Geophys* **36** (6), 803–830. [15].

Rismani Yazdi, Nosrati, Stevens, Vogel, Davies, & Escobedo, 2018, Magnetotaxis Enables Magnetotactic Bacteria to Navigate in Flow. *Small* **14** (5), 1702982. [8].

Roberts & Aurnou, 2012, On the theory of core-mantle coupling. *Geophysical & Astrophysical Fluid Dynamics* **106** (2), 157–230. [12, 22, 33, 59, 75, 76].

Roberts & King, 2013, On the genesis of the Earth's magnetism. *Reports on Progress in Physics* **76** (9), 096801. [8].

Roberts, 1972, Electromagnetic core-mantle coupling. *Journal of geomagnetism and geoelectricity* **24** (2), 231–259. [65].

Rochester, 1960, Geomagnetic westward drift and irregularities in the Earth's rotation. *Philosophical Transactions of the Royal Society of London. Series A, Mathematical and Physical Sciences* **252** (1018), 531–555. [65].

Rochester & Crossley, 2009, Earth's long-period wobbles: A Lagrangean description of the Liouville equations. *Geophysical Journal International* **176** (1), 40–62. [16, 17].

Rosat, 2016, Observations Gravimétriques et Modélisation de la Dynamique Globale de la Terre. PhD thesis, Université de Strasbourg. [12].

Rosat & Gillet, 2023, Intradecadal variations in length of day: Coherence with models of the Earth's core dynamics. *Physics of the Earth and Planetary Interiors* p. 107053. [18].

Rosat, Lambert, Gattano, & Calvo, 2017, Earth's core and inner-core resonances from analysis of VLBI nutation and superconducting gravimeter data. *Geophysical Journal International* **208** (1), 211–220. [10].

Rossby, 1939, Relation between variations in the intensity of the zonal circulation of the atmosphere and the displacements of the semi-permanent centers of action. *J. mar. Res.* **2**, 38–55. [29, 30].

Salhi, Baklouti, Godeferd, Lehner, & Cambon, 2017, Energy partition, scale by scale, in magnetic Archimedes Coriolis weak wave turbulence. *Phys. Rev. E* **95** (2), 023112. [49, 50, 58, 86].

Sasao, Okubo, & Saito, 1980, A simple theory on the dynamical effects of a stratified fluid core upon nutational motion of the Earth. In *Symposium-International Astronomical Union*, , vol. 78, pp. 165–183. Cambridge University Press. [16].

Schaeffer & Cardin, 2005, Quasigeostrophic model of the instabilities of the Stewartson layer in flat and depth-varying containers. *Physics of Fluids* **17** (10), 104111. [30].

Schaeffer & Jault, 2016, Electrical conductivity of the lowermost mantle explains absorption of core torsional waves at the equator. *Geophysical Research Letters* **43** (10), 4922–4928. [14].

Schwaiger, Gillet, Jault, Istas, & Mandea, 2024, Wave-like motions and torques in Earth's core as inferred from geomagnetic data: A synthetic study. *Physics of the Earth and Planetary Interiors* **346**, 107104. [12, 18, 19, 22].

Scorer, 1949, Theory of waves in the lee of mountains. *Q. J. R. Meteorolog. Soc.* **75** (323), 41–56. [20].

Seidelmann, 1982, 1980 IAU Theory of Nutation: The final report of the IAU Working Group on Nutation. *Celestial Mechanics* **27** (1), 79–106. [17].

Shih, Triana, Rekier, & Dehant, 2023, Turbulent dissipation in the boundary layer of precession-driven flow in a sphere. *AIP Advances* **13** (7), 075025. [17].

Sikdar & Dumberry, 2023, The differential precession of Earth's fluid and solid cores. *Physics of the Earth and Planetary Interiors* **339**, 107022. [17, 18].

Smith, 1977, Wobble and nutation of the Earth. *Geophysical Journal International* **50** (1), 103–140. [17].

Smith, 1979, The Influence of the Earth's Rotation on Mountain Wave Drag. *Journal of the Atmospheric Sciences* **36** (1), 177–180. [20].

Smith, 1989, Mountain-induced stagnation points in hydrostatic flow. *Tellus A: Dynamic Meteorology and Oceanography* **41** (3), 270–274. [20].

Sommerfeld, 1912, Die Greensche Funktion der Schwingungslgleichung. *Jahresbericht der Deutschen Mathematiker-Vereinigung* **21**, 309–352. [52].

Tarits & Mandéa, 2010, The heterogeneous electrical conductivity structure of the lower mantle. *Physics of the Earth and Planetary Interiors* **183** (1-2), 115–125. [82].

Teixeira, 2014, The physics of orographic gravity wave drag. *Aip. Conf. Proc.* **2**, 43. [83].

The mpmath development team, 2023, *Mpmath: A Python Library for Arbitrary-Precision Floating-Point Arithmetic (Version 1.3.0)*. [39].

Thompson, Moran, & Swenson, 2017, Very-Long-Baseline Interferometry. pp. 391–483. Cham: Springer International Publishing. [9].

Thorne & Blandford, 2017, *Modern Classical Physics. Optics, Fluids, Plasmas, Elasticity, Relativity, and Statistical Physics*. Princeton University Press. [32, 33].

Tian, Weeks, Ide, Urbach, Baroud, Ghil, & Swinney, 2001, Experimental and numerical studies of an eastward jet over topography. *Journal of Fluid Mechanics* **438**, 129–157. [21].

Vallis, 2017, *Atmospheric and Oceanic Fluid Dynamics*. Cambridge University Press. [20, 29].

Van Hoolst, Baland, & Trinh, 2013, On the librations and tides of large icy satellites. *Icarus* **226** (1), 299–315. [73].

Van Hoolst, Rambaux, Karatekin, & Baland, 2009, The effect of gravitational and pressure torques on Titan's length-of-day variations. *Icarus* **200** (1), 256–264. [20].

Velímský & Knopp, 2021, Lateral variations of electrical conductivity in the lower mantle constrained by Swarm and CryoSat-2 missions. *Earth Planets Space* **73** (1), 4. [82].

Vidal & Cébron, 2023, Precession-driven flows in stress-free ellipsoids. *Journal of Fluid Mechanics* **954**, A5. [34].

Wahr, 1981, Body tides on an elliptical, rotating, elastic and oceanless Earth. *Geophysical Journal International* **64** (3), 677–703. [17].

Weeks, Tian, Urbach, Ide, Swinney, & Ghil, 1997, Transitions Between Blocked and Zonal Flows in a Rotating Annulus with Topography. *Science* **278** (5343), 1598–1601. [21].

Westerburg & Busse, 2003, Centrifugally driven convection in the rotating cylindrical annulus with modulated boundaries. *Nonlinear Proc. Geoph.* **10** (3), 275–280. [21].

Whaler & Gubbins, 1981, Spherical harmonic analysis of the geomagnetic field: An example of a linear inverse problem. *Geophysical Journal International* **65** (3), 645–693. [11].

Wicht & Jault, 2000, Electromagnetic core-mantle coupling for laterally varying mantle conductivity. *J. Geophys. Res.* **105** (B10), 23569–23578. [82].

Wiltschko & Wiltschko, 2005, Magnetic orientation and magnetoreception in birds and other animals. *J Comp Physiol A* **191** (8), 675–693. [8].

Woolard, 1953, Redevelopment of the theory of nutation. *Astronomical Journal, Vol. 58, p. 1 (1953)* **58**, 1. [16, 17].

Wurtele, Sharman, & Datta, 1996, Atmospheric Lee Waves. *Annu. Rev. Fluid Mech.* **28** (1), 429–476. [20, 83].

Yang, 1987, Evolution of a Rossby Wave Packet in Barotropic Flows with Asymmetric Basic Current, Topography and δ-Effect. *Journal of the Atmospheric Sciences* **44** (16), 2267–2276. [31].

Yoshino, 2010, Laboratory Electrical Conductivity Measurement of Mantle Minerals. *Surv Geophys* **31** (2), 163–206. [14].

Zebker, Stiles, Hensley, Lorenz, Kirk, & Lunine, 2009, Size and Shape of Saturn's Moon Titan. *Science* **324** (5929), 921–923. [20].